NOTE TO USERS

DISSERTATION

STUDY OF TRANSFORMER COUPLED TOROIDAL DISCHARGES

Submitted by

Juan José González

Department of Electrical and Computer Engineering

In partial fulfillment of the requirements

For the Degree of Doctor of Philosophy

Colorado State University

Fort Collins, Colorado

Summer 2005

INFORMATION TO USERS

The quality of this reproduction is dependent upon the quality of the copy submitted. Broken or indistinct print, colored or poor quality illustrations and photographs, print bleed-through, substandard margins, and improper alignment can adversely affect reproduction.

In the unlikely event that the author did not send a complete manuscript and there are missing pages, these will be noted. Also, if unauthorized copyright material had to be removed, a note will indicate the deletion.

ProQuest Information and Learning Company
300 North Zeeb Road
P.O. Box 1346
Ann Arbor, MI 48106-1346

COLORADO STATE UNIVERSITY

May 26, 2005

WE HEREBY RECOMMEND THAT THE DISSERTATION PREPARED UNDER OUR SUPERVISION BY JUAN JOSÉ GONZÁLEZ ENTITLED STUDY OF TRANSFORMER COUPLED TOROIDAL DISCHARGES BE ACCEPTED AS FULFILLING IN PART REQUIREMENTS FOR THE DEGREE OF DOCTOR OF PHILOSOPHY.

Committee on Graduate Work

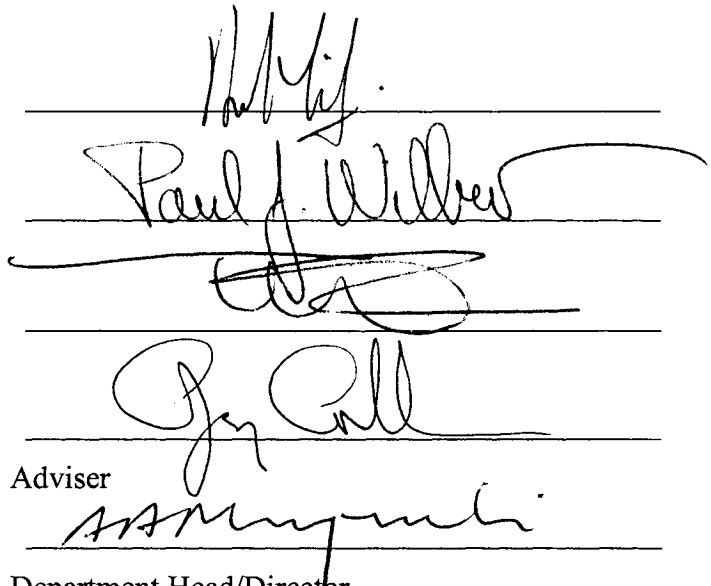

Adviser

Department Head/Director

ABSTRACT OF DISSERTATION

STUDY OF TRANSFORMER COUPLED TOROIDAL DISCHARGES

The technology of transformer-coupled toroidal discharges (TCTD) has grown to become a key element in the semiconductor industry, especially in applications such as remote chamber cleaning and remote generation of reactive gases. This Dissertation provides a description of TCTDs from two different perspectives. On the one hand, it studies the basic mechanisms of power deposition into the plasma and the processes occurring in the plasma bulk, completing the physical description of the plasma by describing its interaction with the wall and the properties of the plasma sheath. On the other hand, this work analyzes the properties of TCTDs from an electrical point of view, investigating the scaling laws that guide their design and exploring the technical obstacles that must be cleared to develop industrial remote plasma sources.

In the first part of this work, we will describe the electrical characteristics and basic plasma bulk physics of TCTDs. The description includes a model for the plasma bulk that incorporates the most relevant mechanisms for the range of pressure and power density of interest. The results of this model are contrasted against experimental measurements carried out in TCTDs. In the second of this Dissertation, we present a

simple model that describes the temporal variation of voltage and current across the sheath and along the chamber in conductive and dielectric vessels.

The good agreement observed between the models predictions and experimental data from argon discharges shows that both models succeeds in capturing the essential aspects of the plasma bulk and its interaction with the walls.

Juan José González
Electrical and Computer Engineering Department
Colorado State University
Fort Collins, CO 80523
Summer 2005

ACKNOWLEDGMENTS

I would like to express my gratitude to the following people for their support and assistance. I would like to thank my advisor Professor George Collins for his help and advice during this work as well as my fiends and co-authors Andrew Shabalin, Denis Shaw and Maximo Frati.

I would like to acknowledge Advanced Energy for allowing this work to happen, especially Steve Rhoades for his advice and encouragement.

Finally, I need to specially thank Fernando Tomasel for his mentoring, help and support but most importantly for his true friendship during all these years.

A mis viejos.

TABLE OF CONTENTS

Chapter 1 Introduction

1.1. Electrodeless discharges: the early years

The study of inductive, electrodeless discharges was initiated in the late eighteen century with the work of Hittorf (1884). Hittorf noticed that the residual gas in a vacuum vessel placed into an inductor begins to glow as soon as a high-frequency current is passed through the inductor. The phenomenon was subsequently examined by several investigators, most notably by Thompson (1927). In Thompson's experiments, plasmas were created in a cylindrical vessel placed inside a solenoid that was excited with trains of damped, high frequency oscillations. He constructed a theory for the discharge proposing that the plasma was sustained by the electric field induced by the changing magnetic field produced by the coil, which included a derivation of an expression for the ignition potential of such discharges. However other authors, with Townsend and Donaldson among them, objected to the hypothesis of the inductive character of the discharge, claiming that the field strength close to the last turns of the coil is many times higher than the strength of the induced electric field. This controversy generated further interest on these discharges, and later studies by MacKinnon showed that the contradiction between the two explanations could be traced back to the different

conditions under which the experiments were performed on each case (Francis 1960). In fact, the current understanding of the operation of inductive discharges ascribes the operation at ignition and low power to the capacitive coupling between the coil and other grounded surfaces. An increase in power after the discharge is initiated increases the conductivity of the plasma, and eventually the induced electric field becomes the main driver for the discharge. For a range of experimental conditions, both forms of excitation (inductive and capacitive) can coexist (Birkhoff and Angew 1958).

All the experiments performed on electrodeless discharges during this period (1920-1936) used relatively low power supplies, so the interest on these studies was mainly academic, and no practical applications for this technology were seen. It was Babat in 1941 that first used RF vacuum tube oscillators to create and sustain inductive plasmas, demonstrating operation in cylindrical vessels up to atmospheric pressure. Electrodeless discharges were subsequently used for other applications, such as spectroscopy (Nisewanger et al. 1946), and production of positive ions (Thonemann 1948). Continuing investigation of cylindrical, inductive discharges eventually paved the road for the development of devices in which low temperature plasmas could be generated and sustained reliably at atmospheric pressure using powers of up to several tens of kilowatts. Limitations on the maximum power load that dielectric chambers were able to withstand led to the development of inductive discharge chambers with water-cooled, slotted metallic walls (Mironer 1963).

1.2. The appearance of toroidal, inductive discharges

Toroidal inductive plasmas were first studied around 1947 by Ware and Cousins at the Imperial College, and by Thonemann at Oxford (Hendry and Lawson 1993), in fusion-related investigations. The idea was to use the ionized gas as the secondary winding of a transformer, the primary windings of which were placed outside and in the plane of the torus. Using a glass torus and a 7 kW, 100 kHz power oscillator, Thonemann was able to successfully generate plasmas with ring currents of several tens of amperes. However, it was clear that the currents needed for fusion experiments could not be sustained in dielectric chambers, due in part to the poor thermal properties of the materials and the difficulties in achieving efficient cooling of the chamber walls. The solution proposed was to use a copper torus, which was constructed and tested in 1949. With this chamber, Thonemann was able to generate secondary currents of up to 2 kA in argon at 1 mTorr, using the same 7 kW oscillator.

The simple toroidal chambers used for these experiments quickly evolved into much more sophisticated plasma confinement schemes, such as tokamaks and stellerators. For several decades, the interest in fusion-related devices directed the development of toroidal discharges towards the region of high-temperature, highly ionized, low-pressure plasmas. However, the interest in simple toroidal discharges without magnetic confinement arose again in the late sixties, motivated by potential applications for the lighting industry: the first electrodeless fluorescent lamp design using ferrite cores dates back to 1967 (Anderson 1969). More recently, the availability of both

low-cost ferrite materials with significantly lower losses at RF frequencies and reliable, low-cost switching mode power supplies able to deliver tens of kilowatts into a plasma load have fueled the development of toroidal sources for industrial applications.

1.3. Industrial applications of low temperature, electrodeless discharges: the case of semiconductor processing

From the early 1970s to the mid 1980s, only one type of plasma source, namely, capacitive RF discharge excited at a frequencies between 50 kHz to 13.56 MHz, was commonly used in wafer etch and deposition tools. The relatively low plasma density typical for these types of sources (10^9 to 10^{10} cm^{-3}) was one of the major factors that limited plasma process capability; in particular etch rates and film growth. Low plasma density is an inherent feature of these plasma tools, and is the result of the very low ionization efficiency of a capacitively coupled, non-magnetized discharge operating at RF frequencies of a few MHz. Indeed, at pressures of 1-300 mTorr, and RF surface power densities of about 0.1 W/cm^2, only 3-10% of the total RF power dissipated in the 13.56 MHz discharge is absorbed by plasma electrons and "spent" partially in ionization. The bulk of the total RF power is "consumed" by plasma ions as a consequence of their motion in the sheath between the plasma and the RF electrodes. This energy is either lost in ion collisions with neutral atoms or molecules, or deposited on the RF electrodes.

In the last few years, substantial progress has been made in the design; research and development of various types of electrodeless plasma sources that have been replacing some of the traditional, parallel-plate capacitively coupled sources. The driving force behind the development of electrodeless discharges for wafer processing has been the need for a plasma-processing tool able to operate with high efficiency at low pressure. To achieve the dissociation and ionization levels needed for high-throughput wafer processing, low efficiency capacitive discharges require rather high input powers, which result in increased wafer damage and degraded selectivity. In addition, independent ion energy control for tailoring film properties is not possible in capacitively coupled discharges, as the plasma production and ion extraction mechanisms are intrinsically linked.

It has been widely demonstrated that much higher plasma densities ($>10^{12}$ cm^{-3}) and higher ionization efficiencies can be achieved by wave excited discharges at higher RF frequencies (including microwaves), or by discharges employing power coupling schemes which are more efficient than capacitive coupling, or by utilizing confinement and resonant effects of static magnetic fields generated by external means (such as coils and permanent magnets). All these schemes are often grouped under the general denomination of high-density plasma sources (Lieberman and Gottscho, 1994). Table 1.1 lists the typical ranges for representative parameters of high-efficiency and conventional, capacitively coupled plasmas commonly used for semiconductor processing.

Table 1.1. Typical ranges for characteristic parameters of high-density and capacitively coupled discharges (Liebermann and Lichtenberg 1994).

Parameter	Units	Parallel-plate discharge	High-density discharge
Pressure p	Torr	0.01 – 1	0.0005 – 0.05
Power P	W	50 – 2,000	100 – 5,000
Frequency f	MHz	0.05 – 13.56	0.05 – 2,450
Volume V	cm^3	1,000 – 10,000	2,000 – 50,000
Cross sectional area A	cm^2	300 – 2,000	300 – 500
Magnetic field B	kG	0	0 – 1
Plasma density n	cm^{-3}	10^9 - 10^{11}	10^{10} - 10^{13}
Electron temperature T_e	eV	1 –5	2 – 7
Ion acceleration energy ϵ_i	V	200 – 1,000	20 – 500
Fractional ionization		10^{-6} – 10^{-3}	10^{-4} – 10^{-1}

Effective inductive in-situ discharges have proven to be decisive for the development of the semiconductor industry during the past decade, although they may not be the best candidates for many of the processing steps for chip manufacturing in the future (ITRS 2004). As the feature size of microelectronics components shrinks to below 100 nm, minimization of ion and charge damage to the device structures becomes an increasingly important device performance driver. To address some of these issues, plasmas can be generated remotely from the process chamber. Remote plasma processing provides a means of controlling the flux of plasma-activated reactants to the substrate without the need for plasmas in direct contact the working piece. Surfaces may be cleaned and/or passivated, and dielectric layers grown while avoiding potential device damage. Remote plasma generation of active species is likely to have an impact on many different areas, such as deposition of silicon oxide and silicon nitride films at very low

temperatures, pre-activation of feeding gases in atomic layer deposition (ALD), deposition of low-stress thin films, etc.

Remote generation of active species is also a solution for chamber cleaning, a step of utmost importance in processes such as chemical vapor deposition (CVD), plasma-enhanced chemical vapor deposition (PE-CVD), high-density plasma chemical vapor deposition (HDP-CVD) and others (Cox et al. 2000). In these processes, films are deposited not only on the semiconductor surfaces where they are desired, but also on all the interior surfaces of the reactor. Deposits on the reactor surfaces must be periodically removed: if the deposits become too thick, they will generate particles that can contaminate the substrates. Cleaning is also essential to reset the chamber conditions before starting every new batch of wafers or, in some cases, before starting every single wafer.

The construction of remote reactors able to produce plasmas for both processing and cleaning poses a number of new challenges. Remote reactors need to generate plasmas efficiently over a wide range of pressures and chemistries with a simple design, this is inexpensive to manufacture and yields high power transfer efficiencies to the plasma. Preventing damage or modification of the structural elements of the source with the plasma is of critical importance for semiconductor applications. The chamber wall material and coatings need to be able to handle high power densities and minimize the recombination losses of the desired active species at the wall surfaces.

Among other approaches (μ-wave, ECR, ICP, etc), toroidal discharges appear as a likely candidate for high power application in very reactive environments (e.g. generation of high flows of atomic fluorine from fluorine bearing gases for remote chamber cleaning). As mentioned before, the basic underlying physical principles of toroidal discharges are well understood for some regions of the operational parameters, such is the case of high-temperature, low-pressure plasmas. However, in remote plasma source applications the electron temperature is only few eV, while the electron densities can be of the order of 10^{12} cm^{-3} (significantly higher than that commonly used for semiconductor plasma processing). The power per unit volume is also considerably large, reaching values up to 10 W/cm^3. The pressure operating range targeted for remote plasma source operation spans four orders of magnitude, typically from 10 mTorr to 100 Torr. Looking at Table 1.1, we can notice that to date these ranges are not simultaneously covered by any of the plasma reactors commonly used in the semiconductor industry. Also for these ranges, no comprehensive study can be found in the literature. Such a study would be therefore especially valuable to fully develop and exploit the potential of this technology in different applications where subjects such as the interaction of the plasma with the chamber walls and the high power density deposited on the plasma have generated new technological challenges (González et al. 2000; González and Shabalin 2003; González et al. 2004a-e; González et al. 2005).

This Thesis provides a description of transformer coupled toroidal discharges (TCTDs) from two different perspectives. On the one hand, it addresses the basic mechanisms of power deposition into the plasma and the processes occurring in that

plasma, completing the physical description of the plasma by describing its interaction with the wall and the properties of the plasma sheath. On the other hand, this work analyzes the properties of TCTDs from an electrical point of view, investigating the scaling laws that guide their design and exploring the technical obstacles that must be cleared to develop industrial remote plasma sources. Finally, dissociation efficiencies for halocarbons in a remote TCTD plasma and the etch rates obtained for SiO_2 are presented in relation to chamber cleaning applications.

1.4. References

Anderson J. M. (1969), *Illuminating Engineering* **4**, 236.

Babat G. I. (1947), *J. Inst. Elec. Eng.* (*London*) **94**, 27-37.

Birhoff G. and Angew Z. (1958), *Phys.* **10**, 204.

Cox M., Lai K., Dubey N., Tran D., Krishnaraj P., Wong M., Loewenhardt P., Lane C., Collins A., Mahoney L. and González J. J. (2000). *A New Remote Plasma Source for HDP-CVD Process Chamber Dry-Cleaning*, 53rd Annual Gaseous Electronics Conference, Houston, Texas, Oct. 24-27.

Francis G. (1960), *Ionization phenomena in gases*, Butterworths Scientific Publications, London.

González J. J., Shaw, D. M., Watanabe, M., Uchiyama, H. and Collins, G. J. (2000), *Electrical model of an inductive ring discharge in argon*, 53rd Annual Gaseous Electronics Conference, Houston, Texas, Oct 24-27.

González J. J. and Shabalin A. (2003), *Plasma Sources Sci. Technol.* **12**, 317-323.

González J. J., Shabalin A. and Tomasel F. G. (2004a), *Mechanism for minimizing ion bombardment energy in a plasma chamber*, United States Patent 6724148.

González J. J., Shabalin A., Geissler S. J. and Tomasel, F. G. (2004b), *Transformer ignition circuit for a transformer coupled plasma source*, United States Patent Application 6822396.

González J. J., Geissler S. J. and Tomasel, F. G. (2004c), *Power Measurement Mechanism For A Transformer Coupled Plasma Source*, United States Patent 6819096.

González J. J., Shabalin A. and Tomasel F. G. (2004d), *Reaction enhancing gas feed for injecting gas into a plasma chamber*, United States Patent Application 20040149701.

González J. J., Dillon S., Shabalin A. and Tomasel, F. G. (2004e), *Vacuum seal protection in a dielectric break*, United States Patent Application 20040149697.

González J. J., Tomasel F. G. and Shabalin A. (2005), *Pulsed excitation of inductively coupled plasma sources*, WO2005029527.

Hendry J. and Lawson, J. D. (1993), *Fusion Research in the UK 1945-1960*, United Kingdom Atomic Energy Authority.

Hittorf W. (1884), *Ann. Phys.* **21**, 90-139.

ITRS: International Technology Roadmap for Semiconductors, 2004 update (http://public.itrs.net).

Lieberman M. A. and Gottscho R. A. (1994), Design of high-density plasma a sources for materials processing, *Physics of Thin Films*, **18**, Francombe M. H. and Vossen J. L. eds., Academic, New York.

Lieberman M. A. and Lichtenberg A. J. (1994), *Principles of plasma discharges and materials processing*, Wiley, New York.

Mironer A. (1963), *AIAA Journal* **1**, 2638-2639.

Nisewanger C. R., Holmes, J. R. and Weissler, G. L. (1946), *J. Opt. Soc. Am.* **36**, 581.

Thomson J. J. (1927), *Phil. Mat. Ser. 7* **4**, 1128-1160.

Thonemann P. C., Moffat, J., Roaf, D. and Sanders, J. H. (1948), *Proc. Phys. Soc. Lond.* **61**, 482.

Chapter 2 Electrical properties of the plasma bulk in transformer-coupled toroidal discharges

2.1. Introduction

In its simplest form, a transformer-coupled toroidal discharge (TCTD) consists of a torus-shaped dielectric chamber (V) that runs through the center of a high magnetic permeability toroidal transformer core (T). Figure 2.1 shows a schematic representation of a toroidal discharge. In this configuration, the time-varying magnetic field in the ferrite core (T) induces an electric field that sustains a closed plasma loop (P). This loop acts as a single-turn secondary winding for the transformer. The electric field driving the current around the torus is controlled by the amount of electron-ion pairs lost by recombination both at the walls and in the plasma bulk (González et al. 2000), therefore the properties of the plasma ring are very similar to those of positive column discharges. This electric field E_{eff} is mainly parallel to the walls of the toroidal chamber, and its strength ranges from about 0.1 V/cm in Ar to 10 V/cm in electronegative gases such as SF_6. On the direction of the small radius of the torus, the loss of mobile electrons to the walls generates an ambipolar electric field that confines the electrons to the bulk region and accelerates the positive ions toward the walls.

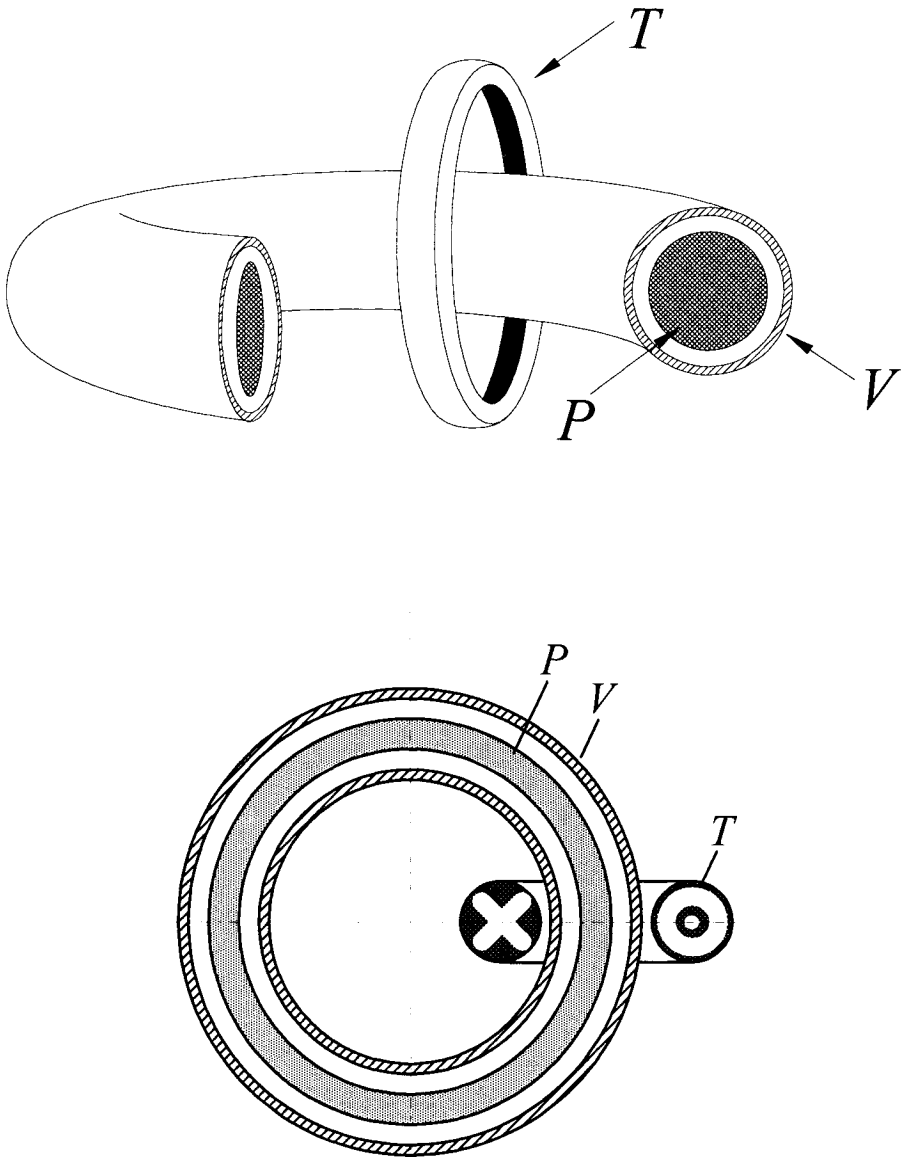

Figure 2.1. Isometric and cross sectional views of the toroidal chamber. Letters *V*, *P* and *T* indicate the vessel, plasma column and toroidal ferrite core, respectively. For simplicity no other elements, such as the primary coil, are drawn.

In TCTDs, the electrical power is coupled most efficiently into the plasma by electrons. Within the plasma bulk, energy from the electrons is transferred with

relatively low efficiency to ions and neutrals by weak collisional processes. As the atom-to-electron mass ratio is large ($\sim 10^5$) and the collision frequency is relatively small, the electron temperature in the bulk T_e greatly exceeds both the ion temperature T_i and the neutral temperature T_g (typically $T_e \sim 1$ eV, whereas T_i and T_g are a few times room temperature, 0.026 eV). Other processes occurring in the bulk, such as dissociation and excitation, can nevertheless create a subgroup of heavy particles with relatively high energies. For ions, ambipolar electric fields are an additional source of acceleration towards the sheath edge.

In this Chapter, we will describe the electrical characteristics and basic plasma bulk physics of TCTDs. The description includes a model for the plasma bulk that incorporates the most relevant mechanisms for the range of pressure and power density of interest. The validity of this model is evaluated contrasting its predictions against experimental measurements.

The Chapter is organized as follows: Section 2.1 describes how the external power source transfers energy to the electrons and (indirectly) to the ions. Section 2.2 discusses the theoretical aspects of the positive column (with special emphasis on electropositive plasmas) and presents a model where the nonlinear diffusion equation with volume recombination is numerically solved to provide the discharge density profiles. Section 2.3 presents the results of measurements carried out in TCTDs with dielectric chambers. Finally, Section 2.4 compares the results of the model with the measured data and discusses the range of validity and predictive power of the model.

2.2. Circuit model for TCTD plasmas

As previously mentioned, in TCTDs the plasma can be considered as the single-turn secondary winding of a transformer. A first-principles approach to describe the spatial and temporal characteristics of such a system requires, at a minimum, numerically solving Maxwell's equations along with a set of equations describing the motion of particles. In the present treatment, toroidal discharges will be approached from a circuital point of view, and only integral plasma parameters such as discharge current, voltage and power will be considered, regardless of their particular spatial distributions. An integral representation of plasma parameters, rather than differential representations such as those described in (Lister and Cox 1992; Denneman 1990), considerably simplifies the analysis and enables one to generate analytical formulae that help to understand the relationships between the external electrical parameters and the plasma characteristics.

When TCTDs are modeled in the form of an equivalent lumped circuit composed of resistor and inductors, the discharge impedance Z_0, which acts as a load to the RF power delivery circuit, can be calculated once the equivalent circuit is specified. The choice of an appropriate equivalent circuit is guided by both the knowledge of the detailed physics of the discharge as revealed by experimental data and the solutions of simplified plasma models. In the following subsections, appropriate circuit models for the bulk plasma and the RF delivery system are derived and approximate values of the circuit elements related to the discharge parameters for the case of Ar and O_2 are estimated.

2.2.1. Impedance of the plasma bulk

The classical expression for the conductivity σ_{bk} in weakly ionized RF plasmas, considering only the contribution of highly mobile electrons, is

$$\sigma_{bk} = \frac{\omega_e^{\,2}\,\varepsilon_0}{\nu_e + j\omega}, \tag{2.1}$$

where ω is the RF angular frequency, ω_e is the electron plasma frequency $\omega_e \equiv (n_e e^2/\varepsilon_0 m)^{1/2}$, and ν_e is the electron-atom collisional frequency for momentum transfer. Note that for plasmas dominated by collisions ($\nu_e >> \omega$) the impedance of the bulk is mainly resistive, while for weakly collisional plasmas ($\nu_e << \omega$) the bulk becomes mainly inductive. If the conduction current due to motion of positive and negative ions is included, we have by analogy

$$\sigma_{bk} = \frac{\omega_e^{\,2}\,\varepsilon_0}{(\nu_e + j\omega)} + \frac{\omega_+^{\,2}\,\varepsilon_0}{(\nu_+ + j\omega)} + \frac{\omega_-^{\,2}\,\varepsilon_0}{(\nu_- + j\omega)}, \tag{2.2}$$

where ω_+, ω_- are the plasma frequency of the ions and ν_+, ν_- are their collisional frequencies for momentum transfer with neutrals. Usually, in electropositive discharges $n_e \approx n_+$ and, since $(\omega_+^{\,2}/\omega_e^{\,2}) = (m/M) << 1$, the contribution of the positive ions can be neglected. However, in strongly electronegative plasmas, where $n_e << n_+ \approx n_-$, the

contribution of the ions to the plasma conductivity may be comparable to that of the electrons.

In general, invoking the plasma neutrality condition $n_e + n_- = n_+$, and writing $\alpha \equiv n_-/n_e$, equation (2.2) may be rewritten as:

$$\sigma_{bk} = \frac{\omega_e^{\,2}\,\varepsilon_0}{(\nu_e + j\omega)} + \frac{(\alpha+1)\,(m_e/M)\;\omega_e^{\,2}\,\varepsilon_0}{(\nu_+ + j\omega)} + \frac{\alpha\,(m_e/M)\,\omega_e^{\,2}\,\varepsilon_0}{(\nu_- + j\omega)}. \tag{2.3}$$

It is convenient to normalize all frequencies to the RF excitation frequency ω, indicating the dimensionless frequencies with an overbar. Separating real and imaginary parts, equation (2.3) becomes

$$\frac{\sigma_{bk}}{\omega\,\varepsilon_0} = \left[\frac{\bar{\nu}_e\,\bar{\omega}_e^{\,2}}{1+\bar{\nu}_e^{\,2}} + \frac{\bar{\nu}_+\,\bar{\omega}_e^{\,2}\,(\alpha+1)(m_e/M)}{1+\bar{\nu}_+^{\,2}} + \frac{\bar{\nu}_-\,\bar{\omega}_e^{\,2}\,\alpha\,(m_e/M)}{1+\bar{\nu}_-^{\,2}}\right] + j\left[-\frac{\bar{\omega}_e^{\,2}}{1+\bar{\nu}_e^{\,2}} - \frac{\bar{\omega}_e^{\,2}\,(\alpha+1)(m_e/M)}{1+\bar{\nu}_+^{\,2}} - \frac{\bar{\omega}_e^{\,2}\,\alpha\,(m_e/M)}{1+\bar{\nu}_-^{\,2}}\right]. \tag{2.4}$$

To understand the behavior of the conductivity for different discharge conditions, it is useful to substitute with the appropriate values for the different typical conditions encountered in TCTDs. For example, let us analyze the cases of Ar and O_2, representing electropositive and electronegative gases, respectively.

For typical TCTD plasmas, the electron density n_e lies in the range of 5×10^{10} cm^{-3} - 5×10^{13} cm^{-3}, increasing with dissipated RF power. Generally, for the same power and pressure, n_e is lower in O_2 (Lichtenberg et al. 1994; Gudmundsson et al. 2001). Thus we have $\overline{\omega}_e \sim 6\times10^3 - 2\times10^5$ for $f=\omega/2\pi=350$ kHz. The electron collision rates in Ar and O_2 are approximately $k_{e/Ar}=10^{-7}$ cm^3/s (Liebermann and Lichtenberg 1994) and $k_{e/O_2}=6.6\times10^{-8}$ cm^3/s (for T_e = 2 eV) (Eliason and Kogelschatz 1986), with corresponding values (at 350 kHz) of $\overline{\nu}_{e/Ar}=1.2\times10^3\,p$ and $\overline{\nu}_{e/O_2}=8\times10^2\,p$, where p is the gas pressure in Torr. Thus, for pressures in the range of 100 mTorr to 10 Torr, $\overline{\nu}_e^{\,2}$ is much larger than unity for both gases. The values for the normalized ion-atom momentum transfer rates are $k_{+/Ar}=1.5\times10^{-9}$ cm^3/s for Ar (Liebermann and Lichtenberg 1994) and $k_{\pm/O_2}=4\times10^{-10}$ cm^3/s for O_2, resulting in collision frequencies of $\overline{\nu}_{+/Ar}=17\,p$ and $\overline{\nu}_{\pm/O_2}=5\,p$, respectively. Using these expressions for the collision frequencies we can compare the electron and ion contributions to the real (resistive) part of the plasma conductivity, which yields

$$\frac{1}{\overline{\nu}_e} >> \frac{\overline{\nu}_\pm\left(m_e/M\right)}{1+\overline{\nu}_\pm^{\,2}}. \tag{2.5}$$

Consequently, the contribution of ions to the real part of the plasma conductivity is insignificant. Although equation (2.5) applies to oxygen plasmas as long as $\alpha<100$ (see equation 2.4), this condition does not represent a serious limitation since for the vast majority of the oxygen plasmas reported in the literature $\alpha<30$ (see for example

Lichtenberg et al. 1994; Gudmundsson et al. 2001). Furthermore, plasma electronegativity is a strongly decreasing function of power (Stoffels et al. 1995). Bogdanov et al. (2002) recently reported electronegativity values of $\alpha < 2$ for 1 Torr of oxygen in an ICP discharge operated at 2×10^{-3} W/cm^3. Thus, for high power density plasmas such as TCTDs, where power densities are in excess of 2 W/cm^3, even lower values of electronegativity can be expected (i.e. high power O_2 discharges will behave as electropositive gas discharges).

Examining the magnitude of the several imaginary terms in (2.4), we observe that

$$\frac{1}{\bar{\nu}_e^{\,2}} >> \frac{(m_e/M)}{1+\bar{\nu}_{\pm}^{\,2}}, \tag{2.6}$$

meaning that the contribution of the ions to the plasma reactance in argon and oxygen plasmas ($\alpha < 100$) is also completely negligible. Note that neglecting the contribution of the ions makes the ratio between the real and imaginary parts of the plasma conductivity equal to the normalized electron collision frequency,

$$\frac{\bar{\nu}_e\bar{\omega}_e^{\,2}/(1+\bar{\nu}_e^{\,2})}{\bar{\omega}_e^{\,2}/(1+\bar{\nu}_e^{\,2})} = \bar{\nu}_e, \tag{2.7}$$

which for our range of conditions is much larger than unity ($\bar{\nu}_e >> 1$). Therefore, for all conditions of interest in argon and oxygen discharges, the conductivity of the bulk of the plasma is essentially real, and (2.4) takes the simple form

$$\sigma_{bk}(n_e) = \frac{\varepsilon_0 \omega_e^{\ 2}}{\nu_e} = \frac{e^2 n_e}{m_e \nu_e} = e\,\mu_e n_e, \tag{2.8}$$

where μ_e is the electron mobility. Notice that for strongly electronegative gases such as chlorine (Lichtenberg at al. 1997) or SF_6 (Stamate and Ohe 1998), where α>150 and α>10^3 respectively, the inductive contribution due to the inertia of the ions becomes significant, and equation (2.4) must be used in full.

Equation (2.1), and therefore equation (2.8), is strictly valid only if the electron collisional frequency is independent of the electron velocity (Lister et al. 1996). In actual plasma discharges, the velocity dependence of the differential collisional frequency $\nu_m(v)$ (see b.17) must be taken into account. However, if ω is sufficiently small (such that $\omega^2 << \nu_e^2$), equation (2.8) is still a good approximation to the electrical conductivity, provided that the chosen value for ν_e is the appropriate average of the differential collisional frequency $\nu_m(\varepsilon)$ over the electron energy distribution $f(\varepsilon)$ (Godyak et al. 1999).

2.2.2. Circuit model

For the purpose of circuit modeling, it is usually sufficient to represent the plasma bulk as a resistor with a value inversely proportional to the electron density n_e, in series with two inductors, one of them representing the electron and ion inertia, and the other

representing the self-inductance of the plasma configuration. For electropositive or weakly electronegative plasmas, the inductance of the plasma is mainly given by the self-inductance of the loop.

Figure 2.2 shows a simplified equivalent circuit for a TCTD. In these discharges, the plasma can be considered as a multitude of filamentary discharges that essentially run in parallel forming, in practice, a one-turn secondary winding ($N_2 \equiv 1$) of the excitation transformer.

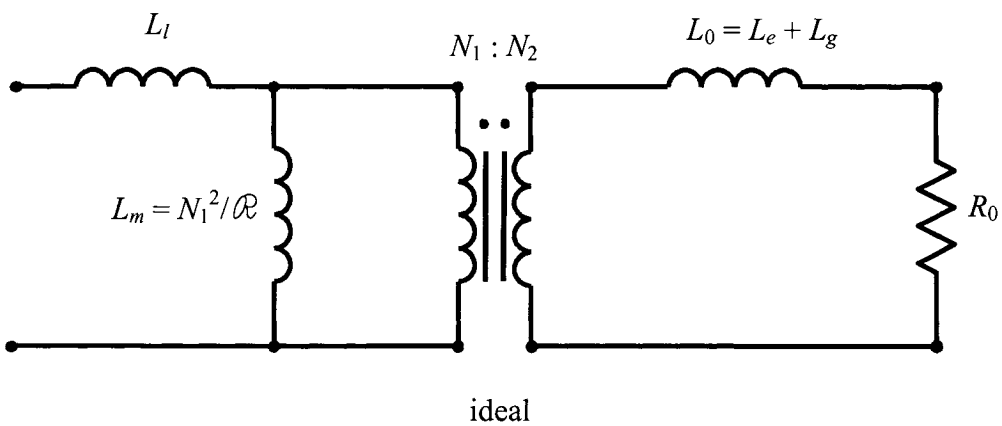

Figure 2.2. Equivalent electrical model for a TCTD.

The plasma impedance Z_0 is defined as the sum of the plasma resistance R_0 and the inductive reactance ωL_0. The plasma resistance R_0 can be estimated by

$$R_0 = \frac{l_p}{A_p}\left\langle \mathrm{Re}(\sigma_{bk}^{-1}) \right\rangle, \tag{2.9}$$

where σ_{bk} is the plasma conductivity defined in (2.4), l_p is the effective plasma length and A_p is the effective plasma cross sectional area. The total plasma inductance L_0 consists of two components: the electron inertia inductance L_e, which is defined from the plasma conductivity formula (2.4) as

$$L_e = \frac{l_p}{\omega A_p}\left\langle \mathrm{Im}(\sigma_{bk}^{-1})\right\rangle, \tag{2.10}$$

and the geometric inductance L_g, which is due to the discharge current path. For the conditions of interest in an electropositive plasma, the electron inductive reactance reduces to $\omega L_e = R_0\,\omega/\nu_e << \omega L_g << R_0$. Consequently, on all practical designs of TCTDs for the pressures and powers of interest, the plasma impedance is almost resistive and can be approximated by

$$Z_0(n_e) \approx R_0(n_e) = \frac{m_e \nu_e l_p}{e^2 \langle n_e \rangle A_p}. \tag{2.11}$$

In contrast to the more common air-coupled inductive plasmas (Piejak et al. 1992), the magnetic coupling between the primary and secondary windings in TCTDs is close to unity, meaning that almost all the magnetic field lines produced by the primary winding pass through the center of the plasma ring. The primary magnetic flux that is not concatenated by the plasma loop and leaks into the air is represented in Fig. 2.2 by the primary leakage inductance L_l. The magnetizing inductance L_m in the equivalent circuit

accounts for the finite value of the magnetic circuit reluctance $\mathcal{R}$ and is given by $L_m = N_1^2/\mathcal{R}$; core material permittivity, gaps sizes and the geometrical dimensions of the transformer assembly determine the value of the reluctance. As the inductances L_l and L_g cause the terminal voltage ratio to differ from the ideal turn ratio N_2/N_1, it is useful to define the *effective* turn ratio as (Erickson and Maksimovic 2001)

$$N_e = \sqrt{\frac{L_g + (N_2/N_1)^2 L_m}{L_l + L_m}} \tag{2.12}$$

and the coupling coefficient between primary and secondary windings as

$$k = \frac{(N_2/N_1)L_m}{(L_l + L_m)^{1/2}(L_g + (N_2/N_1)^2 L_m)^{1/2}}. \tag{2.13}$$

The value for this coefficient falls in the range $0 \leq k \leq 1$, and is a measure of the degree of magnetic coupling between the primary winding and the plasma. In a transformer with perfect coupling, L_l and L_g are zero, and the coupling coefficient k is then equal to unity.

Generally, the plasma self-inductance can be neglected when compared to the magnetizing inductance $L_g << L_m (N_2/N_1)^2$. Under this assumption we can rewrite (2.13) as

$$k = (1 + L_l/L_m)^{-1/2} \approx 1 - \frac{L_l}{2L_m}, \tag{2.14}$$

where we used $L_m > L_l$. In a similar way, we can write the effective turn ratio as

$$N_e = \frac{N_2}{N_1}(1 + L_l / L_m)^{-1/2} = \frac{N_2}{N_1} k . \tag{2.15}$$

Construction of TCTDs transformers with coupling coefficients in excess of 0.9 is quite feasible, obtaining effective turn ratios N_e close to the physical turn ratio N_2/N_1 of the transformer.

The circuit shown in figure 2.2 can be transformed through a straighforward circuit analysis into that shown in figure 2.3 (Erickson and Maksimovic 2001). In this representation, the secondary circuit elements are written in terms of the primary circuit's current and voltage. From the point of view of the primary circuit, the effect of the coupled secondary appears as the transformed impedance $Z_0' = (N_1/N_2)^2 Z_0$, where $Z_0 = R_0 + j\omega L_0$ is the complex impedance of the secondary circuit.

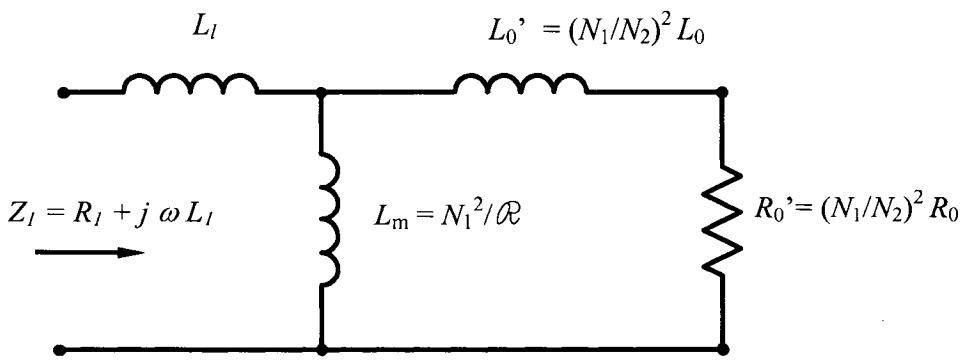

Figure 2.3. Equivalent circuit of a TCTD where the secondary circuit has been referenced to the primary circuit.

From figure 2.3, we can write the primary complex impedance as

$$Z_1 = R_1 + j\omega L_1 . \tag{2.16}$$

The primary equivalent resistance R_1 is written as

$$R_1 = \frac{R_0'\omega^2 L_m^{\,2}}{R_0'^2 + \omega^2 (L_m + L_0')^2}, \tag{2.17}$$

where $R_0' = (N_1/N_2)^2 R_0$ and $L_0' = (N_1/N_2)^2 L_0$ are the plasma resistance and inductance, respectively, referenced to the primary. The equivalent inductance L_1 is of the same general form as R_1, and may be written as

$$L_1 = L_m + L_l - \frac{\omega^2 L_m^{\,2} (L_m + L_0')}{R_0'^2 + \omega^2 (L_m + L_0')^2}. \tag{2.18}$$

The last term on the RHS represents the reactance of the secondary. The negative sign associated with this term can be simply understood by noting that the magnetic field produced by the current in the secondary loop cancels part of the magnetic flux in the primary, thus resulting in a lower total magnetic flux in the primary circuit.

Figure 2.4 shows the change in both primary resistance R_1 (Eq. 2.17) and reactance $X_{L1} = \omega L_1$ as a function of plasma resistance (R_0) for a fixed frequency of

460 kHz and typical values of leakage and magnetizing inductances. The primary reactance is a positively defined, monotonically increasing function of the plasma resistance with an asymptote at the open circuit value of $\omega(L_m + L_l)$, (i.e. no plasma condition or $R_0 = \infty$), and an absolute minimum at $R_0 = 0$ (short circuit value), approximately equal to the total leakage reactance $\omega(L_0' + L_l)$. The leakage inductance of the secondary is approximately equal to the plasma geometric inductance ($L_g \approx L_0$) in absence of the ferrite core. Notice that changes in the plasma resistance $R_0(n_e)$ due to changing conditions in the discharge (e.g. pressure, flow, power, etc), affect the primary resistance and reactance in a non-trivial way. For example, an increase in plasma resistance may imply either an increase or a decrease in primary resistance, depending on the circuit parameters and the value of the plasma resistance.

The primary side equivalent resistance R_1 is a non-monotonic function of the plasma resistance R_0, reaching a maximum value of $R_{1\,max} = \omega L_m^2 / 2(L_m + L_0')$ at $R_0 = \omega(L_0' + L_m)$ (See Eq. 2.13 and Fig. 2.3). For the limit $R_0 \to 0$ (plasma resistance shorted) no power can be dissipated by the network, so the primary impedance needs to be purely reactive or equivalently the primary equivalent resistance needs to be zero ($R_1 = 0$). Similarly, the equivalent resistance tends to zero in the limit $R_0 \to +\infty$ (no plasma condition).

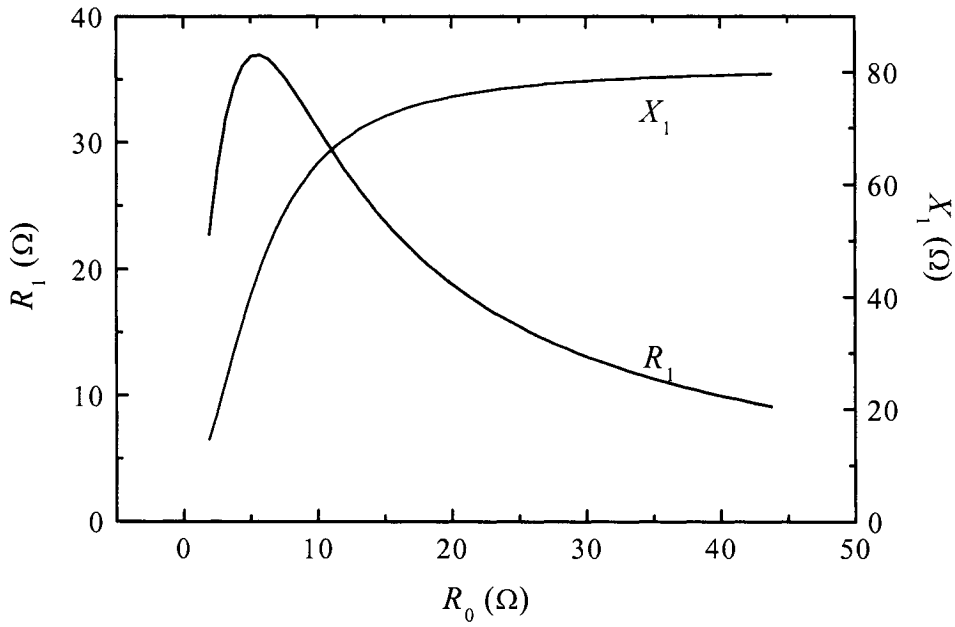

Figure 2.4. Typical variation of the primary reactance and resistance as a function of the plasma resistance.

Note that for an ideal transformer $Z_1 = Z_0' = (N_1/N_2)^2 Z_0$, since $L_m = \infty$ and $L_l = 0$ (perfect coupling). Therefore, since a perfect transformer only offsets the plasma impedance by the turns ratio, for completely resistive plasmas (as is usually the case) the primary impedance is also purely resistive. In general, due to matching requirements and design limitations, the coupling is purposely kept away from unity.

The transformer parameters L_m, L_1, N_1, and N_2, and the plasma leakage inductance L_2, are fairly constant quantities that only depend on the chamber and the power transformer design. Hence, once the experimental setup has been characterized, the only free parameter on the previous equations is the plasma resistance, which can be linked to

the plasma parameters through equation (2.9). To verify the accuracy of the circuit model and the validity of the underlying assumptions, the plasma resistance and the voltage and current in the primary winding were measured for a diverse set of experimental conditions (See Section 2.3 for further details). The plasma impedance was calculated from the measured plasma voltage (V_p) and current (I_p) as

$$R_0 = \frac{V_p}{I_p}\cos(\varphi_p), \tag{2.19}$$

where φ_p is the phase shift between V_p and I_p. Figure (2.5) presents the measured values for R_0, X_1, and R_1, along with values of the primary reactance and resistance calculated using the measured plasma resistance as an input to the equivalent circuit model. The model parameters were obtained from the open and short circuit impedances of the transformer [i.e. $Z_{short} = \omega (L_0' + L_l)$ and $Z_{open} = \omega (L_m + L_l)$]. The figure shows that the calculations agree well with the experimental results for a wide range of plasma resistances and discharge conditions without correcting for changes in the coupling efficiency (i.e. L_0, L_l, and L_m). This inherent characteristic of TCTDs permits to separate the analysis of the electrical excitation of the plasma from the plasma behavior itself.

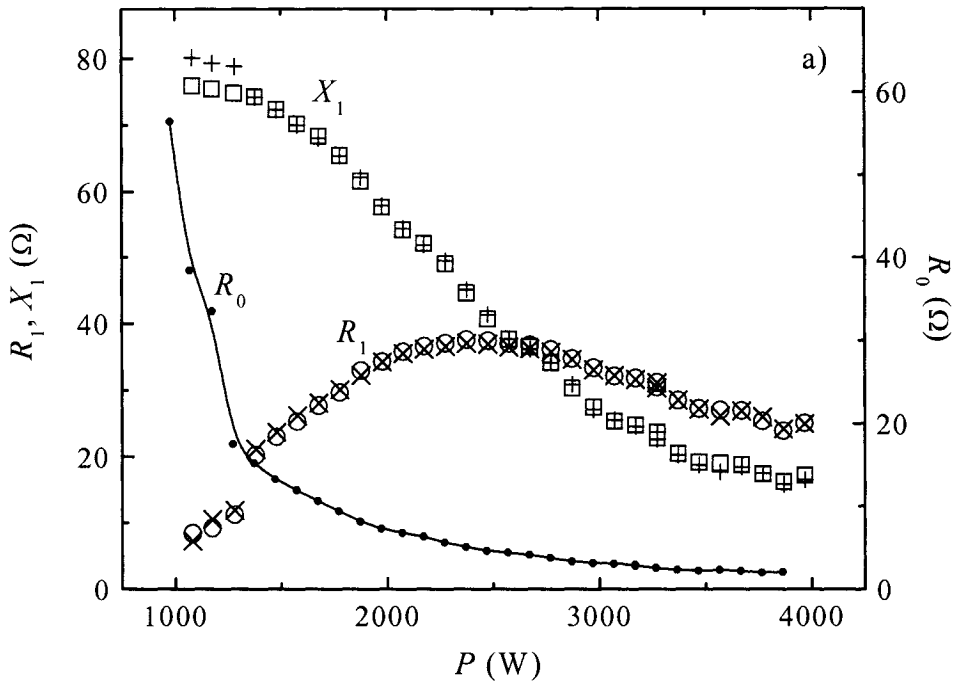

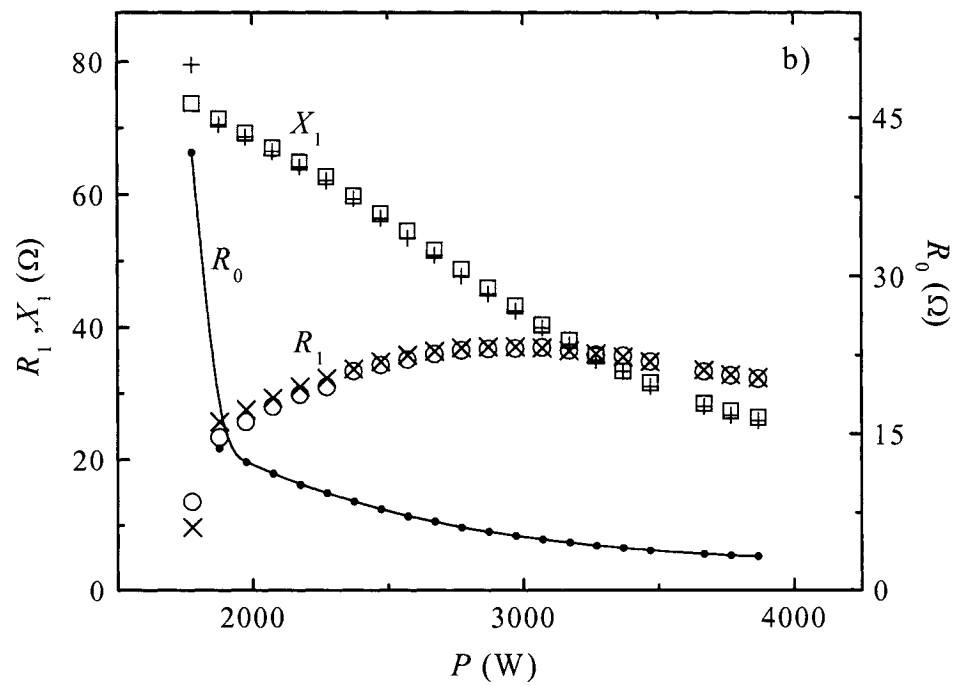

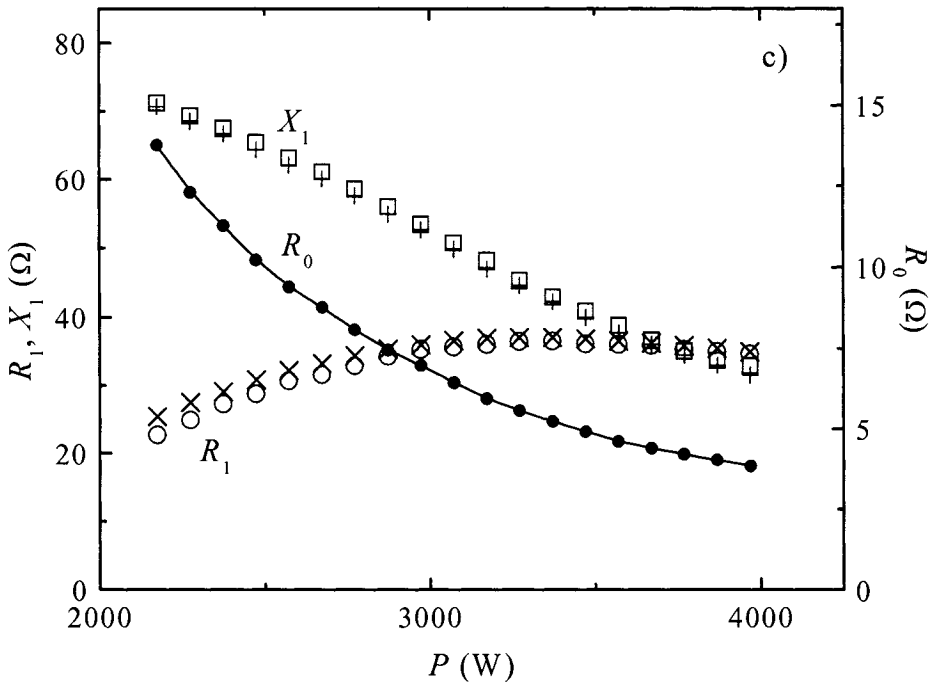

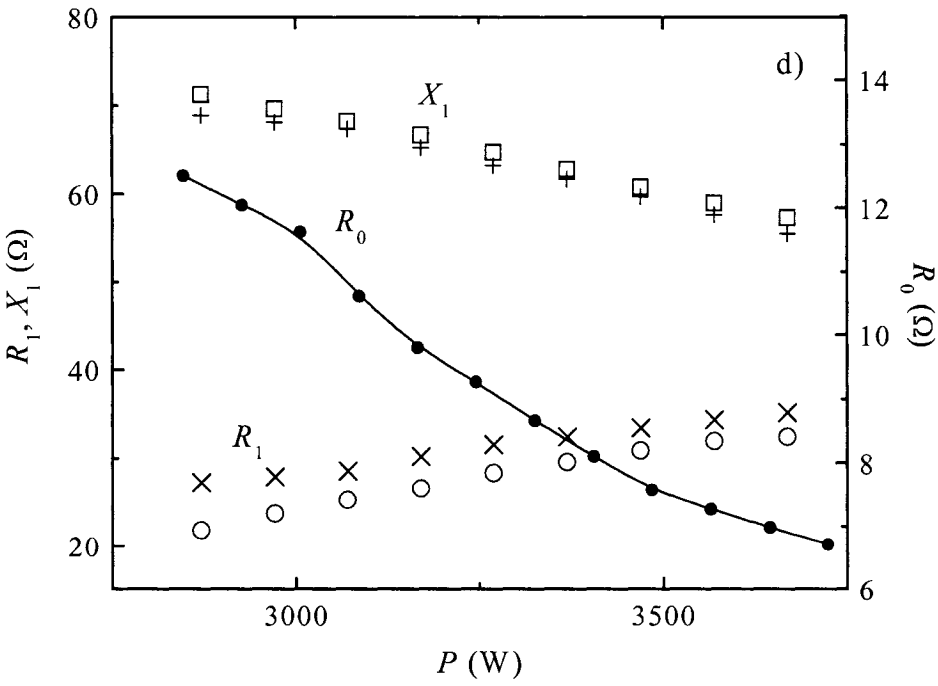

Figure 2.5. Primary resistance (R_1) and reactance (X_1) versus power (P) for different flow conditions in an Ar/O_2 mix; a) 0.3 slm O_2 + 0.15 slm Ar at 0.4 Torr, b) 0.5 slm O_2 + 0.25 slm Ar at 0.6 Torr, c) 0.7 slm O_2 + 0.35 slm Ar at 0.8 Torr and d) 1.3 slm O_2 + 0.65 slm Ar at 1.3 Torr. The meaning of the symbols is as follows: the open circles (○) indicate the measured resistance, the crosses (×) indicate the modeled resistance, the open squares (□) indicate the measured reactance and the pluses (+) indicate the modeled reactance. The solid circles indicate the measured plasma resistance R_0. The values for the transformer electrical parameters are L_m = 27.8 μH, L_1 = 168 nH, L_o = 149 nH and N_1 = 4.

2.3. Positive Column

Having analyzed the TCTDs from a macroscopic and purely circuital point of view, we will now turn our attention to the microscopic processes occurring in the plasma bulk. Let us start by briefly describing the physics of positive columns. Positive columns are defined as quasi-neutral regions where the axial electric field is constant, and the charge concentrations of opposite signs are almost equal and independent of the axial position. Early theories of positive column are reviewed by Francis (1956). In this type of discharges, the drifting electrons primarily carry the current, and the ionization is sustained by the axial electric field. Depending on the pressure, power and gas medium under consideration, the dominant electron loss mechanism can be diffusion, recombination or attachment (in electronegative gases). The earliest treatment of these plasmas is known as the Schottky ambipolar diffusion theory (von Engel 1965; Franklin 1976), which balances the loss of electrons and ions by ambipolar diffusion against the volume generation by collisional impact ionization. This case will be discussed in Section 2.3.1, while the more general case where recombination cannot be neglected will be considered in Sections 2.3.2 and 2.3.3.

2.3.1. Ambipolar Diffusion Model

To analyze this case let start by writing the particle and momentum conservation equations. The continuity equation can be written as

$$\vec{\nabla} \cdot n_e \vec{u}_e = \nu_{iz} n_e = \vec{\nabla} \cdot n_+ \vec{u}_+, \tag{2.20}$$

where ν_{iz} is the electron collision frequency for ionization. We assume here that the source term is one-step ionization of a neutral by an electron. For momentum conservation (see Appendix B, equation b.2), we can write

$$\vec{u}_e = -\mu_e \vec{E} - D_e \frac{\vec{\nabla} n_e}{n_e}, \tag{2.21}$$

$$\vec{u}_+ = \mu_+ \vec{E} - D_+ \frac{\vec{\nabla} n_+}{n_+}. \tag{2.22}$$

We will assume for the time being that the temperatures are constant, and we will not use the equation for energy conservation. This restriction will be removed later. Assuming that ambipolar diffusion applies, $\Gamma_e = \Gamma_+$ and $n_e = n_+ = n$, as usual, we can write

$$\vec{\nabla} \cdot (n_e \vec{u}_e - n_+ \vec{u}_+) = -\mu_e \vec{\nabla} \cdot n\vec{E} - D_e \nabla^2 n - \mu_+ \vec{\nabla} \cdot n\vec{E} + D_+ \nabla^2 n = 0. \tag{2.23}$$

We also have

$$\vec{\nabla} \cdot n\vec{u}_+ = \mu_+ \vec{\nabla} \cdot n\vec{E} + D_+ \nabla^2 n = \nu_{iz} n, \tag{2.24}$$

from which we can write

$$\vec{\nabla} \cdot n\vec{E} = \frac{1}{\mu_+}(D_+ \nabla^2 n + \nu_{iz} n). \tag{2.25}$$

Substituting back in (2.23), we obtain

$$\nabla^2 n \left(\frac{\mu_+ D_+ + \mu_e D_e}{\mu_+ + \mu_e} \right) + \nu_{iz} n = 0 \tag{2.26}$$

or

$$D_a \nabla^2 n + \nu_{iz} n = 0, \tag{2.27}$$

where we used equation (b.9) to define the ambipolar diffusion constant D_a. Equation (2.25) can be rewritten as

$$\nabla^2 n + \frac{\nu_{iz}}{D_a} n = 0. \tag{2.28}$$

This equation allows us to solve for the electron density distribution in the positive column. Expressing (2.28) in cylindrical coordinates, and assuming no variations on the φ or z coordinates, we obtain

$$\frac{1}{r}\frac{\partial}{\partial r}r\frac{\partial}{\partial r}n + \frac{\nu_{iz}}{D_a}n = \frac{\partial^2}{\partial r^2}n + \frac{1}{r}\frac{\partial}{\partial r}n + \frac{\nu_{iz}}{D_a}n = 0. \qquad (2.29)$$

The solution to this equation is the well-known zero-order Bessel function

$$n = n_0 J_0(\beta_0 r). \qquad (2.30)$$

Therefore, under the assumption that one-step ionization is the predominant source for charged particles, and that diffusion is the only electron loss mechanism, the zero-order Bessel function describes the radial electron density distribution in a cylindrical discharge tube. We know that at the walls of the discharge tube, $n(r = R_p) \approx 0$ requiring that

$$\beta_0 = \frac{\chi_{01}}{R_p} = \left(\frac{\nu_{iz}(T_e)}{D_a(T_e)}\right)^{1/2} = \left(\frac{k_{iz}(T_e)\, n_g}{D_a(T_e)}\right)^{1/2}, \qquad (2.31)$$

where χ_{01} is the first zero of the zero order Bessel function, $k_{iz}(T_e)$ is the ionization rate constant (see b.16), and n_g is the gas density. Both the radial variation of n and the electron temperature T_e are therefore univocally determined if n_g and R_p are specified. This is a statement of a balance condition: as many electrons must be produced per second as are lost to the walls by diffusion. Although (2.31) does not give a completely self-consistent solution (since the finite ion flux at the wall implies infinite velocity at zero density), it can provide a reasonably accurate value of T_e. The reason is that $k_{iz}(T_e)$ is a very sensitive function of T_e of the form (see equation b.16)

$$k_{iz}(T_e) = \sigma_0 \bar{v}_e \left(1 + \frac{\varepsilon_{iz}}{2T_e}\right) \exp\left(-\frac{\varepsilon_{iz}}{T_e}\right). \tag{2.32}$$

Thus, T_e depends only weakly on all parameters except for ionization energy, ε_{iz}.

Since all charged particles are lost by diffusion to the walls, we can calculate the total power lost per unit discharge length as

$$P_{D_a} = 2\pi R_p \Gamma_{R_p} e \varepsilon_T , \tag{2.33}$$

where Γ_{R_p} is the radial particle flux and $e\,\varepsilon_T$ is the total energy carried out per electron-ion pair created (see b.18). Replacing the particle flux to the wall by $\Gamma_{R_p} = -D_a \left|\frac{dn(r)}{dr}\right|_{r=R_p} = \frac{D_a}{R_p} \chi_{01}\, J_1(\beta_0 R_p) n_0$ yields

$$P_{D_a} = 2\pi \chi_{01} J_1(\chi_{01}) e\, n_0 D_a(T_e)\, \varepsilon_T(T_e) , \tag{2.34}$$

which can be solved along with equation (2.31) to determine n_0 as function of the input power.

The electric field E along the z-axis of the discharge is calculated by equating the absorbed input power to the power lost. Since uniform temperatures have been assumed,

no heat flux terms need to be included. Equating the energy gained by the electrons per unit discharge length per second

$$P_{in} = 2\pi \int_0^{R_p} \vec{J} \cdot \vec{E}\, r\, dr \tag{2.35}$$

to the power lost to the walls (2.34), and substituting our radial density solution from (2.30), we have

$$e n_0 \mu_e E^2 2\pi \int_0^{R_p} J_0(\beta_0 r) r\, dr = 2\pi \chi_{01} J_1(\chi_{01}) e\, n_0 D_a(T_e)\, \varepsilon_T(T_e)\,, \tag{2.36}$$

where we have replaced the current density J along z using the plasma conductivity defined in (2.8)

$$J = \sigma_{bk} E = e n \mu_e E, \tag{2.37}$$

and we have taken E out of the integral by assuming that it is constant in the long, thin plasma approximation. We see that n_0 cancels from (2.36), resulting in an equation for the electric field only. Performing the integration, we find that J_1 also cancels out, so we can solve directly for E to obtain

$$E = \left(\frac{\nu_{iz} \varepsilon_T}{\mu_e} \right)^{1/2} = \frac{\chi_{01}}{R_p} \left(\frac{D_a \varepsilon_T}{\mu_e} \right)^{1/2}. \tag{2.38}$$

Note that both D_a and μ_e are dependent on the gas density n_g, so for a given density the electric field only depends on T_e. We can make this dependence explicit by using equations (b.5) and (b.4) for D_a and μ_e, respectively,

$$E(T_e) = \frac{\chi_{01}}{R_p}\left(\frac{m k_m(T_e)}{M\, k_M}\, T_e\, \varepsilon_T(T_e)\right)^{1/2}, \tag{2.39}$$

where k_m and k_M are the electron–atom (figure b.1) and the ion-atom elastic collisions rates, respectively. Equation (2.39) shows that $E(T_e)$ is a function of the gas and the electron energy only. Therefore, under the assumption that the electron energy (temperature) is determined by the product $n_g R_p$ (Eq. 2.31), the longitudinal electric field (and hence the plasma voltage V_p) along the discharge is fixed, and is independent of the current through the discharge. We will later return to this statement to discuss its range of validity, and to compare the resulting predictions with the experimental results.

2.3.2. Recombination Losses

As the discharge pressure increases, losses mechanisms in the plasma bulk, such as volume recombination, start to play an important role in the discharge dynamics. In the volume recombination process, an electron and a positive ion unite to form a neutral molecule or an atom in ground state. This mechanism includes the totality of

microscopic processes involved in the capture of an electron to form an excited atom or molecule and the subsequent decay to the neutral ground state.

Volume recombination is essentially a chemical process, and the continuity equation when recombination dominates is written as

$$\nu_{iz} n_e = k_{rec} n_+ n_e , \tag{2.40}$$

where k_{rec} is an effective recombination coefficient. Since the recombination rate depends on the local density, this mechanism tends to flatten out any non-uniformity in the plasma density. Therefore, recombination results in spatially uniform plasmas, in contrast to the Bessel-like density profiles produced by diffusion.

The recombination process, being of a collisional microscopic nature, is considerably more complicated in its details than diffusion. In a rather simple manner however, we realize that the probability for a recombination event to occur will depend upon the relative kinetic energies of the electron and the ion and, more importantly, on how the energy and momentum can be conserved in the recombination process. There are several different processes by which energy and momentum can be conserved, resulting in different types of recombination. Nevertheless, in spite of the nature of the recombining positive ion, the mechanisms for ion-electron recombination can be divided into two- and three-body processes. The generalized two-body process may be written as

$$X^+ + e \rightarrow X + h\nu, \tag{2.41}$$

while three-body processes may be written as

$$X^+ + Y + e \rightarrow X + Y + h\nu. \tag{2.42}$$

Bhave and Cooper (1995) have shown that it is possible to lump together the contributions of various recombination processes into a single or *effective* recombination rate, which introduces a dependence on the square of the electron density into the continuity equation. The effective recombination coefficient k_{rec} can be written as

$$k_{rec} = \alpha_{eff} T_e^{-0.7} n_g^{\ 2}, \tag{2.43}$$

where n_g the gas density and α_{eff} is the effective recombination constant, which includes two- and three-body recombination effects (Akhtar et al. 2003; Bates and Khare 1965; Pitaevskii 1962).

2.3.3. Semi-Global Density Model

Considering the case where both diffusion and recombination are playing an important role, the continuity equation (2.28) becomes

$$\vec{\nabla} \cdot D_a \vec{\nabla} n + \nu_{iz} n - k_{rec} n^2 = 0. \tag{2.44}$$

Being this expression is a nonlinear equation in the electron density, no general solutions can be easily found. Let us consider instead a zero-dimensional model, where all spatial variations are averaged over the entire volume. Integrating equation (2.44) over the discharge volume V_p, and using Green's theorem to convert the volume integral of the diffusion term into an integral over the discharge's surface A_p, we have

$$\oint_{A_p} D_a \vec{\nabla} n \, d\vec{A}_p + \int_{V_p} \left(\nu_{iz} n - k_{rec} n^2 \right) dV_p = 0 \tag{2.45}$$

Expressing (2.45) in cylindrical coordinates and assuming variations only in r yields

$$-2\pi R_p l_p \Gamma_{R_p} + \nu_{iz} 2\pi l_p \int_0^{R_p} n(r) r \, dr - k_{rec} 2\pi l_p \int_0^{R_p} n(r)^2 r \, dr = 0, \tag{2.46}$$

where l_p is the plasma column length and

$$\Gamma_{R_p} = -D_a \left| \frac{dn(r)}{dr} \right|_{r=R_p} \tag{2.47}$$

is the average positive ion flux normal to the wall surfaces. Unlike the model with only diffusion losses in which the electron density cancels out to give an equation only depending on T_e, equation (2.46) depends also on n. To eliminate this dependence, we

will use the equation for absorbed power. Repeating the same averaging process over the discharge volume for the energy balance equation and rearranging terms, we obtain a set of equations for the particles and energy conservation per unit plasma length in steady state

$$-R_p\,\Gamma_{R_p} + R_p^{\,2} A_{eff}\, n_0\, \nu_{iz} - R_p^{\,2} B_{eff}\, n_0^{\,2} k_{rec} = 0 \tag{2.48}$$

$$P_{abs} = 2\pi R_p^{\,2} A_{eff}\, \nu_{iz}\, n_0\, e\,\varepsilon_c + 2\pi R_p \left|\Gamma_{R_p}\right| e\left(\varepsilon_e + \varepsilon_i\right), \tag{2.49}$$

where we have defined the average integral parameters as

$$A_{eff} = \int_0^1 \frac{n(R_p \bar{r})}{n_0}\,\bar{r}\,d\bar{r} \qquad \text{and} \qquad B_{eff} = \int_0^1 \left(\frac{n(R_p \bar{r})}{n_0}\right)^2 \bar{r}\,d\bar{r}\ , \tag{2.50}$$

In these expressions ε_c is the collisional energy lost per electron-ion created (b.18), ε_e is the mean kinetic energy lost per electron lost (b.19), and ε_i ion kinetic energy lost at the surface (b.21). Using a simple diffusion model, we can estimate Γ_{R_p} as

$$\Gamma_{R_p} = \frac{D_a\, n_0}{d_{eff}\, R_p} \tag{2.51}$$

where we define

$$d_{eff} = -\frac{n_0}{R_p \left| \frac{dn(r)}{dr} \right|_{r=R_p}} \tag{2.52}$$

as the effective normalized diffusion length in the plasma bulk. Inserting (2.52) in (2.48) and (2.49) yields the following set of equations

$$n_0 = \frac{A_{eff}\, \nu_{iz}(T_e) - \frac{D_a(T_e)}{R_p^{\,2} d_{eff}}}{B_{eff}\, k_{rec}(T_e)} \tag{2.53}$$

$$P_{abs} = e\, 2\pi R_p^{\,2} n_0 \left(A_{eff}\, \nu_{iz}(T_e)\, \varepsilon_c(T_e) + \frac{D_a(T_e)}{R_p^{\,2} d_{eff}} \left(\varepsilon_e(T_e) + \varepsilon_i(T_e) \right) \right), \tag{2.54}$$

where the dependence on T_e is explicitly shown. The general solution for these equations is very complex: in this case, T_e is not only a function of $n_g R_p^2$, but also depends on n_g and the discharge power P_{abs}, in addition to other dependences on the geometry and the radial density profile through A_{eff}, B_{eff} and d_{eff}. However, some general features of the equilibrium can be readily noticed. From (2.48) we see that $A_{eff}\, \nu_{iz} \geq D_a / R_p\, d_{eff}$ for an equilibrium condition to exist; this condition guarantees enough ionization to compensate for both volume and surface particle losses.

To gain deeper insight on the behavior of the plasma, let us examine two simple limiting cases for the ratio of volume-to-surface losses.

a) Volume Losses Dominate. For this case Γ_{Rp} can be eliminated, and the density profile becomes independent of the radial position r (see figure 2.6), meaning that the geometric coefficients become $A_{eff} = B_{eff} = 0.5$. Replacing the new coefficients values and removing the diffusion term from equation (2.53), we obtain the density as a function of the electron temperature T_e

$$n_0 = \frac{\nu_{iz}(T_e)}{k_{rec}(T_e)}. \tag{2.55}$$

The power balance equation (2.54) along with (2.55) yields

$$P_{abs} = e\,\pi R_p^{\,2}\,\frac{\nu_{iz}(T_e)^2\,\varepsilon_c(T_e)}{k_{rec}(T_e)}, \tag{2.56}$$

which can be used to calculate T_e. For this recombination-dominated discharge, the electric field E along the z-axis of the discharge is calculated by equating the absorbed input power to the power lost by recombination such that

$$E = \left(\frac{\nu_{iz}\,\varepsilon_c}{\mu_e}\right)^{1/2} = \left(\frac{k_{rec}\,n_0\,\varepsilon_c}{\mu_e}\right)^{1/2}, \tag{2.57}$$

with both k_{rec} and μ_e dependent on the gas density n_g. Note that the electric field depends not only on T_e but also on the electron density.

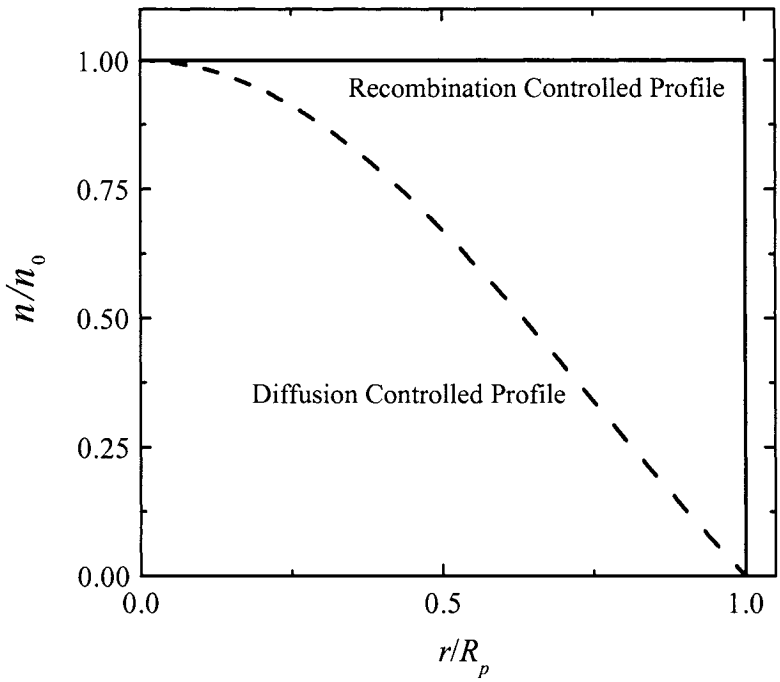

Figure 2.6. Normalized electron density spatial profiles for a recombination dominated discharge (solid-red line) and a diffusion controlled discharge (dashed-blue line). The dashed line curve corresponds to the zero-order Bessel function (diffusion solution), while the solid line corresponds to the recombination limit (flat profile).

b) Surface losses dominate. Let us assume that the effect of recombination can be neglected in determining the spatial distribution of the plasma density. Therefore, the density profile is only controlled by ambipolar diffusion, which for cylindrical symmetry results in a zero-order Bessel function (figure 2.6). In this case, the coefficients A_{eff}, B_{eff} and d_{eff} take the following values:

$$A_{eff} = \frac{J_1(\chi_{01})}{\chi_{01}}, \quad B_{eff} = 0.135 \quad \text{and} \quad d_{eff} = \frac{1}{\chi_{01} J_1(\chi_{01})}. \tag{2.58}$$

Substituting these values in (2.53) and (2.54), we obtain the expressions for the plasma density and the absorbed power,

$$n_0 = \frac{J_1(\chi_{01})}{\chi_{01}\, 0.135} \frac{\nu_{iz}(T_e) - \frac{\chi_{01}^{\ 2}}{R_p^{\ 2}} D_a(T_e)}{k_{rec}(T_e)} \tag{2.59}$$

and

$$P_{abs} = \frac{J_1(\chi_{01})}{\chi_{01}} e\, 2\pi R_p^{\ 2} n_0 \left(\nu_{iz}(T_e)\varepsilon_c(T_e) + \frac{\chi_{01}^{\ 2}}{R_p^{\ 2}} D_a(T_e) \left(\varepsilon_e(T_e) + \varepsilon_i(T_e)\right) \right). \tag{2.60}$$

Equations (2.59) and (2.60) can now be combined to determine T_e and n_0 for a given input power, gas density and discharge tube radius. In the asymptotic case where $n_0 k_{rec} << \nu_{iz}$, we recover the ambipolar diffusion solution of equations (2.31) and (2.34). This approach provides good estimates for the electron temperature and density, even for conditions where the volume losses are similar to the ionization rate. However, equations (2.59) and (2.60) do not provide a completely self-consistent solution, since the density profile can differ substantially from the assumed zero order Bessel function as gas pressure is increased (see figure 2.7).

2.3.4. Numerical Model

As discussed on Section 2.3.3, equations (2.53) and (2.54) are very complex, in the sense that T_e depends on multiple quantities including the density profile. However, the density profile parameters can be independently obtained by solving a dimensionless continuity equation for different initial conditions that only depend on the ratio between the recombination and the ionization rate. The electron density profile is controlled by the continuity equation (2.44), which in cylindrical coordinates becomes

$$D_a\left[\frac{\partial^2 n(r)}{\partial r^2}-\frac{1}{r}\frac{\partial n(r)}{\partial r}\right]+\nu_{iz}\,n(r)-k_{rec}\,n(r)^2=0\,, \tag{2.61}$$

with

$$\left|\frac{dn(r)}{dr}\right|_{r=0}=0 \quad \text{and} \quad n(r=0)=n_0 \tag{2.62}$$

for boundary conditions. We define the dimensionless radius $\bar{r}$ and dimensionless plasma density $\bar{n}$ as

$$\bar{r}=\beta r \tag{2.63}$$

and

$$\bar{n}(\bar{r}) = \gamma\, n(\beta r), \tag{2.64}$$

with

$$\beta = \left(\frac{\nu_{iz}}{D_a}\right)^{1/2} \tag{2.65}$$

and

$$\gamma = \frac{k_{rec}}{\nu_{iz}} = \frac{\alpha\, T_e^{-0.7}}{k_{iz}}. \tag{2.66}$$

Inserting (2.63) and (2.64) into (2.61) and (2.62), we obtain

$$\frac{\partial^2 \bar{n}(\bar{r})}{\partial \bar{r}^2} - \frac{1}{\bar{r}}\frac{\partial \bar{n}(\bar{r})}{\partial \bar{r}} + \bar{n}(\bar{r}) - \bar{n}(\bar{r})^2 = 0 \tag{2.67}$$

with the new boundary conditions

$$\left|\frac{d\,\bar{n}(\bar{r})}{d\,\bar{r}}\right|_{\bar{r}=0} = 0 \qquad \text{and} \qquad \bar{n}(\bar{r}=0) = \bar{n}_0 = \gamma\, n_0. \tag{2.68}$$

Equation (2.67) can be integrated numerically to obtain the dimensionless density profile $\left|\bar{n}(\bar{r})\right|_{\bar{n}_0}$, which is completely defined by the continuity equation and the

dimensionless peak density $\overline{n}_0$ (see figure 2.7). Applying the boundary condition at the chamber walls $n(R_p) = 0$ to the solution for the normalized density we obtain the condition

$$\beta = \frac{\chi(\overline{n}_0)}{R_p} = \left(\frac{\nu_{iz}(T_e)}{D_a(T_e)} \right)^{1/2} \tag{2.69}$$

where $\chi(\overline{n}_0)$ is the first zero of $\overline{n}$. Condition (2.69) is the generalization of equation (2.31), and it can be utilized to obtain an approximate solution for the electron temperature. However, in a similar way equations (2.69) and (2.31) do not give a completely self-consistent solution, since the finite ion flux at the wall implies infinite velocity at zero density.

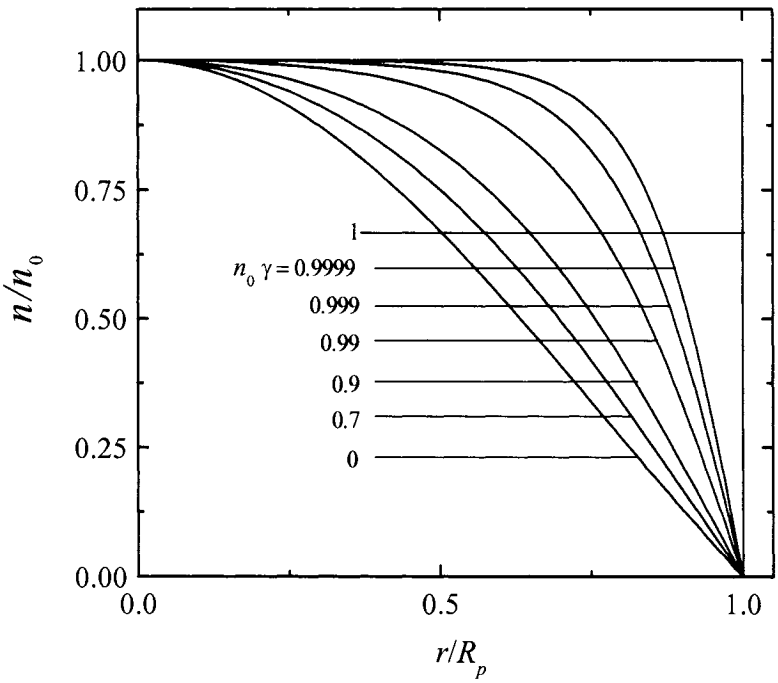

Figure 2.7. Normalized electron density profile for different values of the dimensionless peak density $\bar{n}_0 = n_0 \gamma$. The curve for $n_0 \gamma = 0$ corresponds to the zero-order Bessel function (diffusion solution), while $n_0 \gamma = 1$ corresponds to the recombination limit (flat profile).

Expressing the distribution parameters (2.50) and the effective diffusion length (2.52) as a function of $\bar{n}(\bar{r})$ we obtain

$$A_{eff}(\bar{n}_0) = \frac{1}{\beta^2 R_p^{\,2} \bar{n}_0} \int_0^{\beta R_p} \bar{n}(\bar{r}) \bar{r}\, d\bar{r} = \frac{1}{\bar{n}_0} \int_0^1 \bar{n}(\chi(\bar{n}_0)\bar{r}) \bar{r}\, d\bar{r}, \tag{2.70}$$

$$B_{eff}(\bar{n}_0) = \frac{1}{\beta^2 R_p^{\,2} n_0^{\,2} \gamma^2} \int_0^{\beta R_p} \bar{n}(\bar{r})^2 \bar{r}\, d\bar{r} = \frac{1}{\bar{n}_0^{\,2}} \int_0^1 \bar{n}(\chi(\bar{n}_0)\bar{r})^2 \bar{r}\, d\bar{r} \tag{2.71}$$

and

$$d_{eff}(\bar{n}_0) = -\frac{\bar{n}_0}{\beta R_p \left|\frac{d\bar{n}(\bar{r})}{d\bar{r}}\right|_{\bar{r}=\beta R_p}} = -\frac{\bar{n}_0}{\left|\frac{d\bar{n}(\chi(\bar{n}_0)\bar{r})}{d\bar{r}}\right|_{\bar{r}=1}} \tag{2.72}$$

with $\bar{n}_0$ as a parameter. Table 2.1 and figure 2.8 show the results of solving equations (2.67) and (2.70-2.72) for different values of $\bar{n}_0$ in the interval [0,1]. Note $\bar{n}_0=1$ represents the case with only volume recombination.

Table 2.1. Shape parameters as a function of normalized peak density.

$\bar{n}_0 = \gamma n_0$	$\chi(\bar{n}_0)$	$d_{eff}(\bar{n}_0)$	$A_{eff}(\bar{n}_0)$	$B_{eff}(\bar{n}_0)$
0	2.405	0.8013	0.216	0.135
0.1	2.497	0.7848	0.218	0.137
0.2	2.602	0.7663	0.220	0.139
0.3	2.724	0.7455	0.223	0.142
0.4	2.866	0.7210	0.227	0.145
0.5	3.038	0.6925	0.231	0.150
0.6	3.253	0.6575	0.237	0.156
0.7	3.536	0.6143	0.245	0.164
0.8	3.942	0.5569	0.256	0.176
0.9	4.652	0.4715	0.276	0.198
0.95	5.374	0.4028	0.295	0.220
0.99	7.064	0.2937	0.334	0.268
0.995	7.792	0.2618	0.347	0.286
0.999	9.479	0.1997	0.372	0.319
0.9995	10.204	0.1918	0.381	0.331
0.9999	11.880	0.1617	0.397	0.353
1	∞	0	0.5	0.5

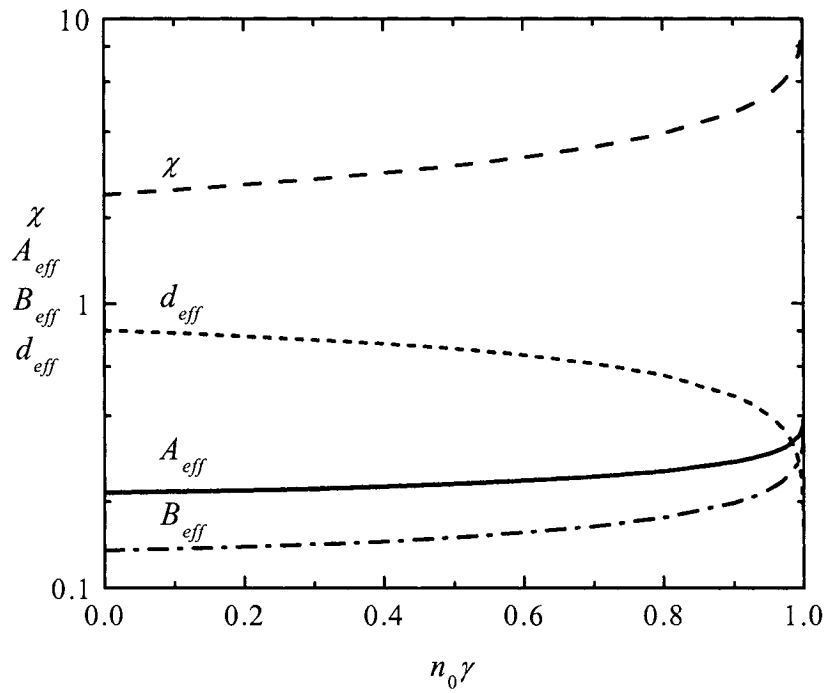

Figure 2.8. Density distribution parameters χ (red dash), A_{eff} (solid blue), B_{eff} (dash dot olive) and d_{eff} (dot green) dependence with $\bar{n}_0 = n_0\,\gamma$.

Inserting equations (2.66), (2.70), (2.71) and (2.72) into (2.53) and (2.54) and utilizing expressions (2.50) and (2.52) we obtain the following set of equations

$$n_0 = \frac{A_{eff}(n_0 \frac{k_{rec}(T_e)}{\nu_{iz}(T_e)})\ \nu_{iz}(T_e) - \frac{D_a(T_e)}{R_p^{\,2}\, d_{eff}(n_0 \frac{k_{rec}(T_e)}{\nu_{iz}(T_e)})}}{B_{eff}(n_0 \frac{k_{rec}(T_e)}{\nu_{iz}(T_e)})k_{rec}(T_e)} \qquad (2.73)$$

$$P_{abs} = e\,2\pi R_p^{\,2} n_0 \left(A_{eff}(n_0 \frac{k_{rec}(T_e)}{\nu_{iz}(T_e)})\ \nu_{iz}(T_e)\varepsilon_c(T_e) + \frac{D_a(T_e)}{R_p^{\,2} d_{eff}(n_0 \frac{k_{rec}(T_e)}{\nu_{iz}(T_e)})} \left(\varepsilon_e(T_e) + \varepsilon_i(T_e)\right) \right), \tag{2.74}$$

which can be numerically solved to obtain the electron temperature T_e and the radial density profile $n(r)$. In the same spirit of equation (2.36), we can equate the input electrical power to the power being lost by the discharge

$$e\,2\pi\ R_p^{\,2}\ n_0\ A_{eff}\ \mu_e\ E^2 = P_{abs}. \tag{2.75}$$

Replacing P_{abs} by (2.74), we obtain

$$e\,2\pi\ R_p^{\,2}\ n_0\ A_{eff}\ \mu_e E^2 = e\,2\pi R_p^{\,2} n_0 \left(A_{eff}\ \nu_{iz}\ \varepsilon_c + \frac{D_a}{R_p^{\,2} d_{eff}} \left(\varepsilon_e + \varepsilon_i\right) \right), \tag{2.76}$$

where we see that n_0 cancels out, resulting in an equation only for the electric field E. However, E still depends on n_0 through A_{eff} and d_{eff}. Solving directly for E we obtain

$$E = \left(\frac{\nu_{iz}(T_e)}{\mu_e(T_e)} \varepsilon_c(T_e) + \frac{D_a(T_e)}{R_p^{\,2} d_{eff}\, A_{eff}} \left(\varepsilon_e(T_e) + \varepsilon_i(T_e)\right) \right)^{1/2} \tag{2.77}$$

which, along with (2.73) and (2.74), can be solved to obtain the discharge axial field.

2.4. Experimental

In order to understand the plasma behavior and check the predictions of the different models for various operating conditions, the electron density as well as electrical parameters such as the plasma discharge voltage V_p, the current through the plasma I_p, and phase angle between them ϕ_p were measured for a range of pressures and plasma powers in argon and oxygen discharges. In addition, the temperature of the neutrals was measured for different power levels for stagnated flow conditions. This Section describes the experimental setup used for these measurements.

2.4.1. Description of the plasma chamber

For the argon discharges, measurements were carried out on three different rectangular dielectric tube rings with center-to-center dimensions of 5.7 cm wide by 5.5 cm, 10.5 cm and 15 cm long, named *A*, *B,* and *C*, respectively. The corresponding plasma lengths were 22.4 cm, 32.4 cm and 41.4 cm, while the chamber volumes were 44.8 cm^3, 64.8 cm^3, and 82.8 cm^3, for chambers *A*, *B*, and *C*, respectively. All rings were made with cylindrical Pyrex glass tubing (1.6 cm ID, 1.9 cm OD, cross section 2 cm^2). A separate stem of Pyrex tubing was attached to the rings to interface with the vacuum system. Figure 2.9 shows a photograph of an argon discharge on tube A, with all diagnostics removed for the sake of clarity.

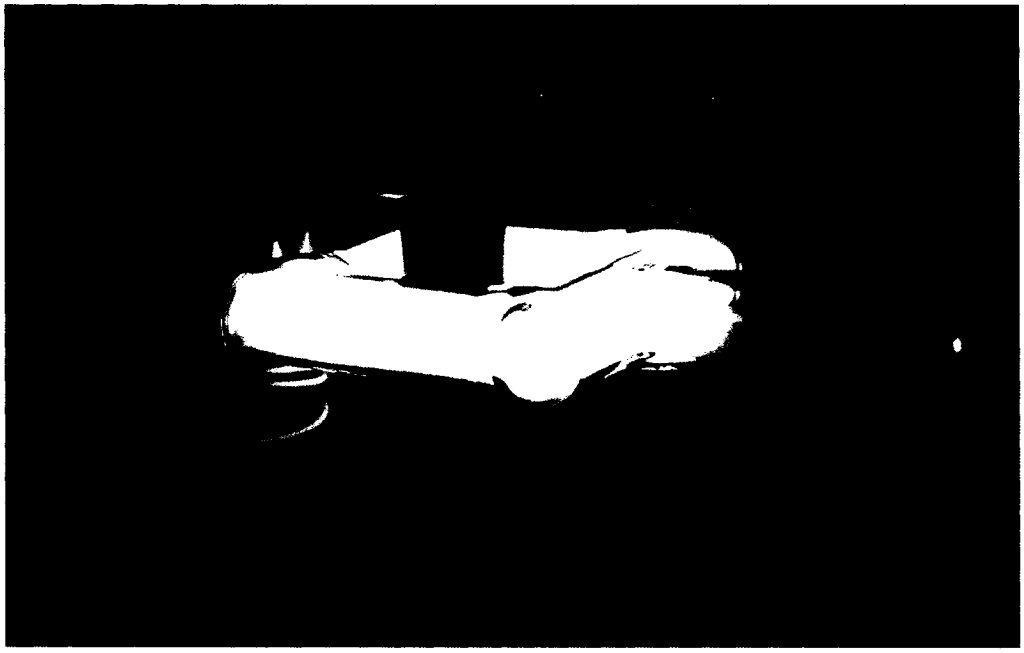

Figure 2.9. Photograph of an argon discharge running in chamber *A*. Only driving transformer core is shown, the diagnostics are omitted for clarity.

Figure 2.10 shows a schematic representation of the complete experimental setup. The ring-shaped vacuum chamber allows closed plasma loops to form around the magnetic core. The arrow in the cross section presented in figure 2.10 shows the direction of the RF electric field and current in the plasma. To couple the RF power into the plasma, two Philips UR64/40/20-3F3 ferrite cores were clamped together. The single transformer module had a four-turn primary winding directly connected to the RF power supply (Advanced Energy PDX 1250) operating at a frequency of 350 kHz. The power supply internal load match provides an output impedance range of 10 Ω to 350 Ω in seven selectable configurations of its output transformer. This adjustment was sufficient to directly match the plasma load to the output impedance of the power supply without the need of any extra matching circuitry. The electrical equivalent model parameters

were L_m = 103 μH, L_l = 5.4 μH, L_o = 60 nH, which translates into a coupling coefficient k = 0.97 and an effective turn ratio N_e = 0.245.

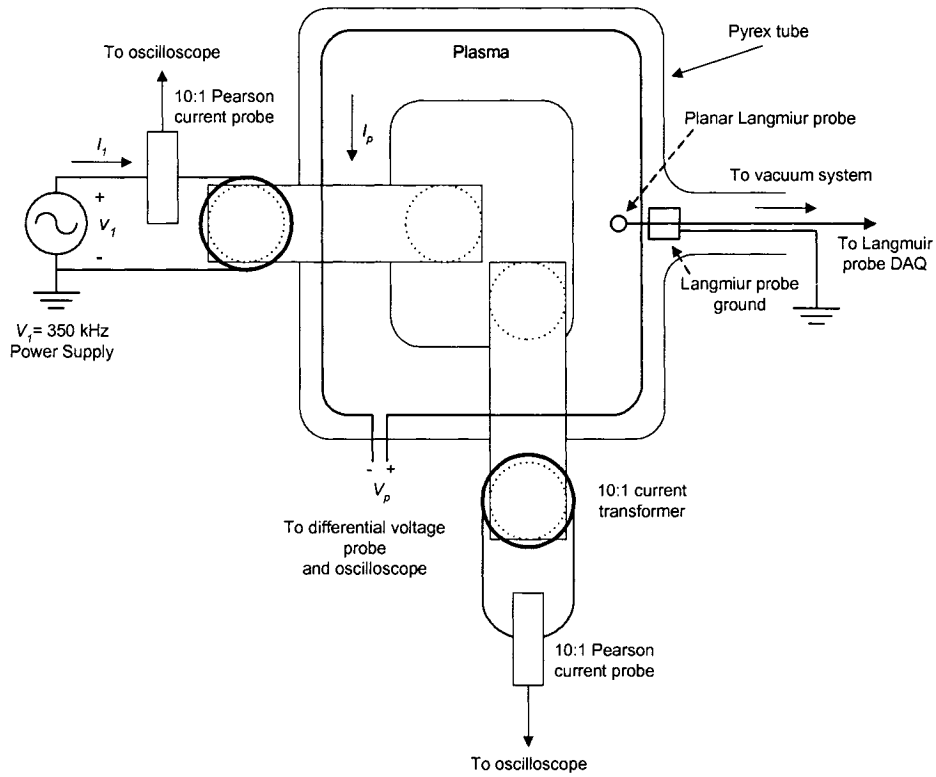

Figure 2.10. Schematic representation of the TCTD discharge system used in the experiments, showing the RF excitation and the way in which some of the relevant electrical parameters were measured.

For electrical measurements in oxygen discharges, a different setup designed to handle higher gas flows and powers was utilized. The chamber was made of quartz instead of Pyrex glass, due to the better thermal properties of quartz. The chamber was built with four 15.5 cm long sections of standard 4.4 cm ID quartz tube welded in a

square arrangement (see figure 2.11). The chamber was symmetrically teed with input and output ports. This arrangement provided a total plasma length of 62 cm, a cross section of 15.2 cm^2 and a volume of 943 cm^3.

Figure 2.11. Photograph of the experimental setup, utilized for the electrical measurements in oxygen discharges, showing five transformers sustaining a 1.8 Torr oxygen plasma.

The oxygen plasmas required a higher output power supply (Advanced Energy PDX 5000) to maintain the same volumetric discharge power density on the larger chamber. This power supply has a fixed, 50 Ω output impedance, so a matching network was required to match the plasma-transformer circuit impedance to 50 Ω. A standard, two-capacitor "L" matching network with a series inductor was sufficient to match the

impedances over the whole range of discharge conditions surveyed. The transformer configuration was optimized to operate within the higher plasma impedance range and higher discharge voltages typical of oxygen plasmas. The transformer configuration consisted of five three-turn transformers connected in parallel (figure 2.12), providing an equivalent turn ratio (N_1/N_2) of 0.6 to 1. Figure 2.13 shows the magnetic circuit assembly. Each of the five individual transformers was assembled with four I25/25/100 bars made of Phillips 3C90 ferrite material. The coupling coefficient for each of the individual transformer was k = 0.86. Since this arrangement uses four gaps instead of two, and the gaps between I-bars are wider due to their lower dimensional tolerance, the coupling coefficient here is lower than that of the argon discharge setup.

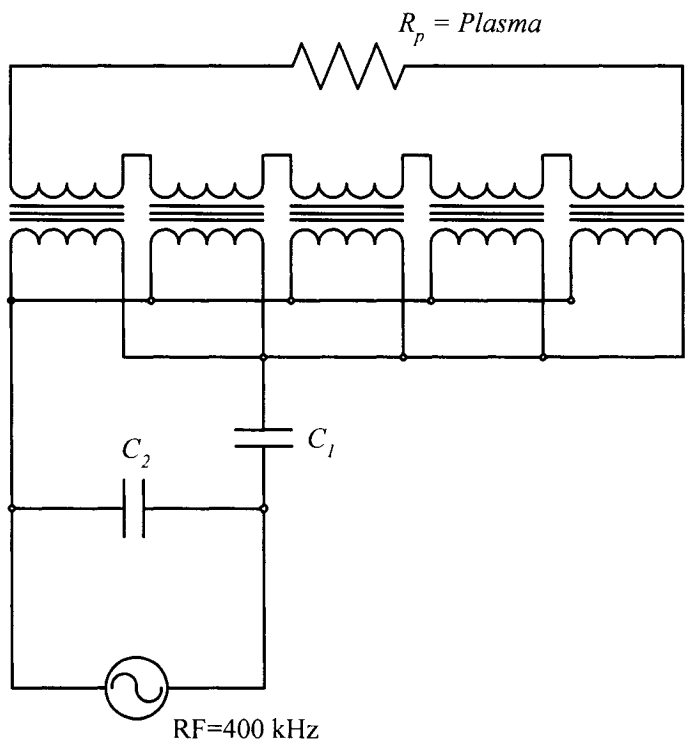

Figure 2.12. Illustration of the matching network and the transformer configuration utilized to obtain high plasma discharge voltages (> 500 V). The resistor R_p represents the plasma in this circuit.

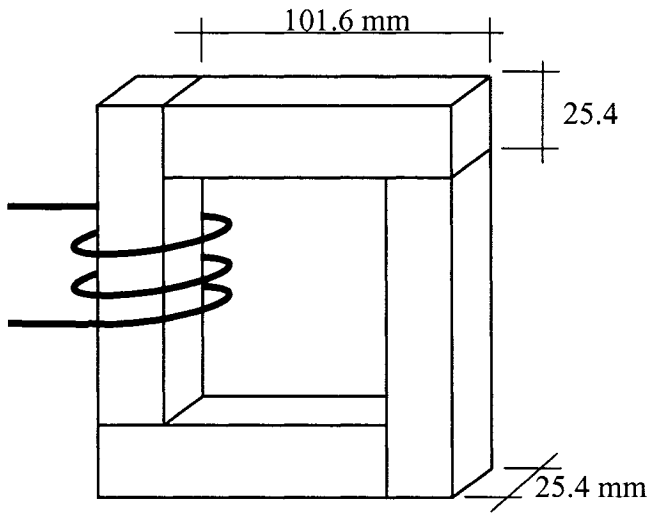

Figure 2.13. The transformer assembly consists of four I-bar pieces (1 in^2 cross-section) and a three-turn primary. The open circuit inductance at 400 kHz is 17.41 μH and the short circuit inductance is 4.41 μH, giving a magnetizing inductance of 13 μH and a leakage inductance of 4.41 μH.

The optimum values for the match capacitors C_1 and C_2 were obtained by equating the combined impedance Z_L of the match and the transformer to the power supply output impedance (figure 2.14):

$$Z_L^{-1} = \left(\frac{1}{j\omega C_1} + j\omega L_C + Z_1(R_p) \right)^{-1} + j\omega C_2 , \tag{2.78}$$

where $Z_1(R_p)$ is a function of the plasma resistance R_p (defined be equations (2.16), (2.17) and (2.18)), and L_C is the match series inductor. Separating the real and imaginary parts of equation (2.78), we obtain

$$R_1 + \frac{\left(\omega L_C + \omega L_1 - \frac{1}{\omega C_1}\right)^2}{R_1} = 50\Omega \tag{2.79}$$

and

$$\frac{R_1^2 + \left(\omega L_C + \omega L_1 - \frac{1}{\omega C_1}\right)^2}{\omega L_C + \omega L_1 - \frac{1}{\omega C_1}} = \frac{1}{\omega C_2} \tag{2.80}$$

which define the capacitance values C_1 and C_2 for the best match condition.

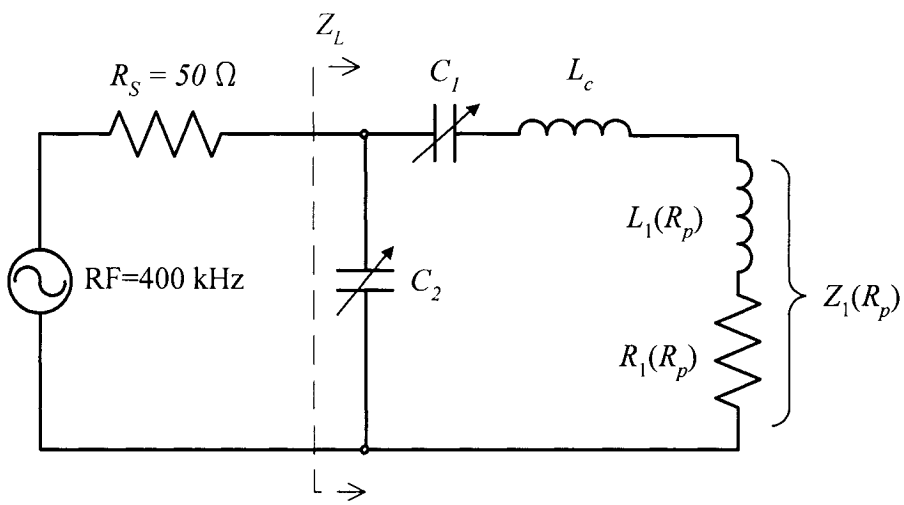

Figure 2.14. Equivalent circuit for matching the TCTD to the RF power generator.

Figure 2.15 shows the capacitance values C_1 and C_2 as a function of the plasma resistance (R_p) for a frequency of 400 kHz. The equivalent electrical model parameter values for this setup were L_m = 2.6 μH, L_l = 0.88 μH, L_o = 100 nH, which translates into a coupling coefficient k = 0.858 and an effective turn ratio N_e = 0.689.

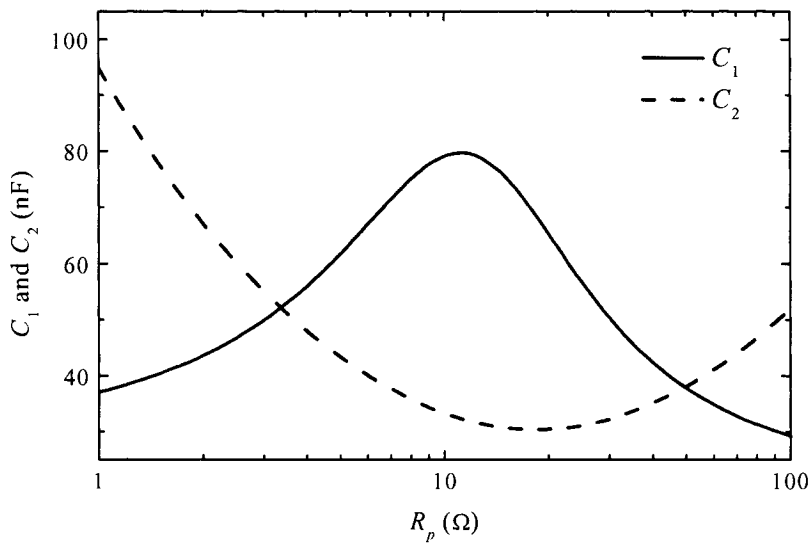

Figure 2.15. Optimum match capacitor values for a RF frequency of 400 kHz and a series inductor value L_C = 5 μH.

2.4.2. Diagnostics

The electrical parameters on the primary side of the transformer (V_1, I_1, φ_1) were measured directly, using a high voltage probe (Tektronix P5100) and a 0.1 V/A Pearson 411 current probe. Both the voltage and current probes were calibrated by measuring known RF currents and voltages. The plasma voltage (V_p) was measured using a wire loop that followed the plasma path from outside the chamber (see figure 2.10 and 2.11)

connected to a differential voltage probe (Tektronix P5205). A 0.1 V/A Pearson 411 current probe connected to a 10:1 (argon setup) or a 20:1 (oxygen setup) current transformer placed around the discharge tubes was utilized to measure the current through the plasma (I_p). The phase angle between the plasma voltage and current waveform was also measured using the same probes.

A simple, two-sided planar Langmuir probe was used to measured the ion saturation current I_{probe} in argon plasmas. The probe was constructed from a 3 mm diameter, 100-μm thick tantalum disk, spot-welded to a tungsten wire. The voltage applied to the probe was swept from 0 V to -20 V with respect to a grounded 10 mm x 10 mm copper plate placed along the glass wall adjacent to the Langmuir probe. Since the chamber is dielectric, the copper grounding plate is required to provide a ground reference to the plasma. Figure 2.16 shows a typical I-V trace. These traces showed well-defined saturation current for all cases. No changes were observed in the measured plasma electrical characteristics upon insertion or operation of the probe in the plasma.

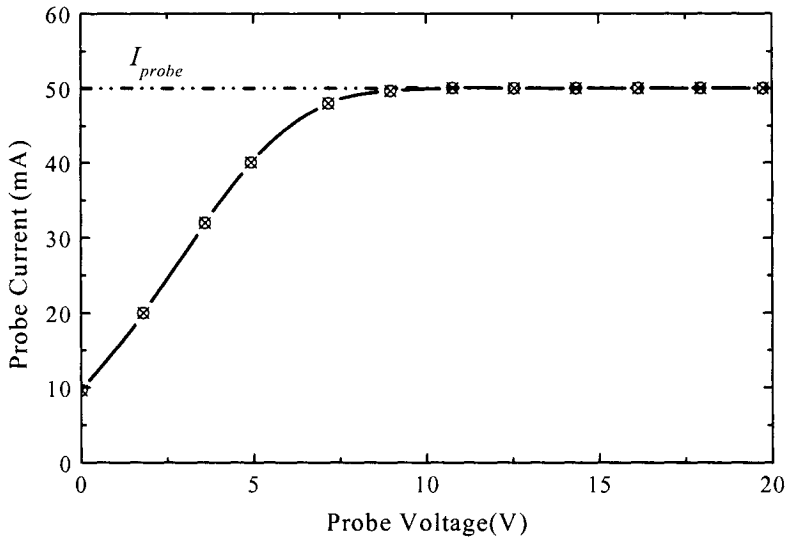

Figure 2.16. Example of a measured I-V trace showing the saturation ion current I_{probe}. Plasma conditions were 6 Torr Ar, 450 W RF, and middle size plasma tube. This figure is representative of all Langmuir probe measurements.

The electron density was calculated directly from the ion saturation current as (Lieberman and Lichtenberg 1994)

$$n = \frac{I_{probe}}{0.607 e A_{probe} u_B}, \tag{2.81}$$

where I_{probe} is the probe current, A_p is the probe total collection area, and u_B is the Bohm velocity. For the collisional case, as the velocity at the sheath edge u_s is no longer equal to u_B (refer to Chapter 3 for a detailed discussion), Eq. (2.81) was corrected using the following approximation

$$u_s \approx u_B \left(1 + \frac{\pi \lambda_{De}}{2 \lambda_i} \right)^{-1/2} \tag{2.82}$$

where $\lambda_{De} = \left(\frac{\varepsilon_o T_e}{e n} \right)^{1/2}$ is the electron Debye length and λ_i is the ion-atom collisional mean free path. This expression is a fit to the numerical solution obtained by Godyak and Sternberg (1990) for collisional sheaths. The behavior of plasma sheaths at high pressures is discussed in more detail in Chapter 3.

2.5. Results and discussion

2.5.1. Gas Temperature Measurements

For low power density plasmas, operating gas temperatures are often assumed to be close to ambient temperature. However, recent works on planar inductively coupled plasma reactors (Hebner 1996; Singh et al. 2001; Donnelley and Malyshev 2000; Tonnis and Graves 2002; Chevolleau and Fukarek 2000) report neutral heating to a level significantly higher than room temperature, with temperatures of up to 1,300 K. In addition, temperatures were found to increase consistently with both discharge pressure and power. Based on these observations, and considering the high power densities deposited into the plasma by TCTP devices, the discharge gas temperature was measured

for different steady state operating conditions in an attempt to understand the influence of gas temperature on the discharge performance.

In TCTPs, the neutral gas in the discharge is heated by elastic and inelastic electron-atom collisions and by electron–ion recombination processes. The power deposited into the plasma is transferred to the walls by the neutral atoms, radiation and recombination of charged particles at the wall surface. All power deposited into the plasma is ultimately dissipated by the chamber walls through convection to the surrounding air or by conduction to the cooling water, depending on the chamber design.

For the experiments described herein, the average neutral gas temperatures in the plasma column for different pressures and power levels were estimated from measurements of the pressure increase produced by the gas heating under stagnation. Under this condition, the amount of power dissipated and the chamber wall temperature can be assumed to be independent of the gas pressure. The discharge was stagnated using a shutoff valve installed between the vacuum system and the discharge chamber. The setup was optimized to minimize the volume upstream the isolation valve ($\mathcal{V}_T$). This volume comprises the active discharge volume ($\mathcal{V}_p$) and the volume added by the capacitance manometer and the connection fittings ($\mathcal{V}_l$):

$$\mathcal{V}_T = \mathcal{V}_p + \mathcal{V}_l. \tag{2.83}$$

When the plasma is off, the entire volume of gas is in equilibrium at room temperature, so we can write

$$p_1 = \frac{N_T}{\mathcal{V}_T} k_B T_1, \tag{2.84}$$

where k_B is Boltzmann constant, N_T is the total number of molecules, and p_1 and T_1 are the plasma off pressure and temperature, respectively. When the plasma is turned on, the pressure in the entire volume $\mathcal{V}_T$ increases to a steady state value p_2. Under these conditions we can write

$$p_2 = \frac{N_p}{\mathcal{V}_p} k_B T_p = \frac{N_1}{\mathcal{V}_1} k_B T_1, \tag{2.85}$$

where T_p is the gas temperature in the discharge region, N_p and N_1 are the number of molecules in the discharge volume and the parasitic volume, respectively. Using $N_T = N_1 + N_p$ along with (2.83) and (2.85) we can write the following expression for the discharge gas temperature

$$T_p = \frac{p_2 \mathcal{V}_p}{p_1 \mathcal{V}_T - p_2 \mathcal{V}_1} T_1 \tag{2.86}$$

The plasma off pressures were compared before and after the measurements for every experimental point, verifying that no significant degas occurred during the measurements.

The experimental data dependence with the gas pressure (p_g) was fitted with an exponential function

$$T_g(P_p, p_g) = A(P_p) + B(P_p)\exp\left(\frac{p_g}{C(P_p)}\right) K$$
$$A(P_p) = 625 + 77P_p \qquad (2.87)$$
$$B(P_p) = -253 - 65P_p$$
$$C(P_p) = 8.87 - 0.323P_p$$

where A, B, and C are fitting coefficients that depend linearly on the plasma power density P_p.

Figure 2.17 shows the experimental data along with the fitted curves. At low pressures, all charged particles are lost at the walls by ambipolar diffusion. These particles recombine at the chamber wall surfaces liberating the energy gained from the electric field, both during the ionization process and at the sheath. Therefore, only a fraction of the total power absorbed by the plasma is used to heat the gas. As pressure increases, a larger fraction of the charged particles recombine in the plasma bulk, increasing the amount of power being transferred to the neutral gas. The sharp increase in gas temperature between 1 and 10 Torr in figure 2.17 is due to the transition from a diffusion-controlled to a recombination-controlled plasma.

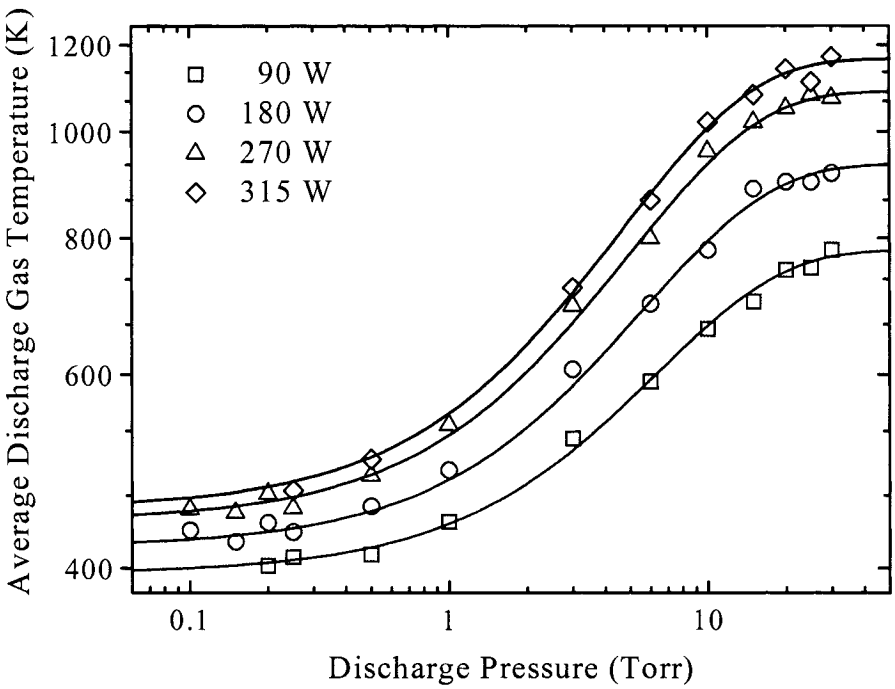

Figure 2.17. Discharge gas temperature versus gas pressure for different powers. The solid lines correspond to the fitted function (2.87). The experimental points correspond to the following discharge power densities: (◊) 7 W/cm^3, (Δ) 6 W/cm^3, (○) 4 W/cm^3 and (□) 2 W/cm^3.

2.5.2. Electrical measurements

In Section 2.2.1, we showed that the phase angle between the plasma voltage and current is expected to be directly proportional to the inverse of the normalized electron collision frequency, Eq. (2.7). We also showed that for electropositive plasmas operating under our experimental conditions this phase angle is expected to be zero (real plasma impedance). Figure 2.18 shows a plot of the phase angle versus discharge current for pressures between 250 mTorr and 10 Torr. For all cases, the phase angle is greater than

zero due to the finite geometrical inductance of the plasma ($L_g \approx 65$ nH) and the low plasma resistivity. The phase angle can be expressed as

$$\phi_p = ArcTan\left(\frac{\omega L_g}{R_0}\right) \approx \frac{\omega L_g}{R_0}, \tag{2.88}$$

where R_0 is the plasma resistance and (ωL_g) is the discharge geometric reactance, which is a constant that depends only on the discharge geometrical configuration. Using the definition for R_0 (Eq. 2.9) and equation (2.8) for the plasma conductivity, we can rewrite (2.88) as

$$\phi_p \approx \frac{\omega L_g A_p}{L_p} \mu_e n_e \propto n_e, \tag{2.89}$$

which shows the direct proportionality of the phase angle with the electron density and hence with the plasma current. This proportionality is readily observed in Fig. 2.18. For oxygen plasmas, the measured values for the phase angle were below the instrumental resolution for all conditions. This result implies a low electronegativity (i.e. the plasma resistivity dominates over the inductive ion inertia component, $R_0 >> \omega (L_g+L_\pm) > \omega L_\pm$), in agreement with observations by other authors (Stoffels et al. 1995; Vender et al. 1995).

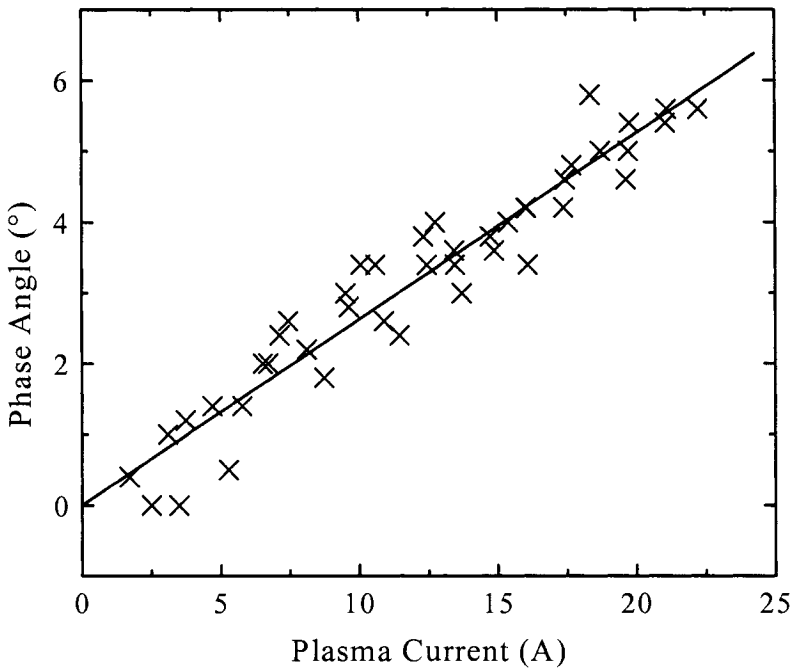

Figure 2.18. Phase angle versus discharge current for pressures between 250 mTorr and 10 Torr of argon in the 41.4 cm long chamber *"C"*.

Figures 2.19 and 2.20 show the dependence of plasma resistance on the average current density. The dashed hyperbola on each graph shows the dependence predicted by Schottky's diffusion model, where the electric field is assumed to be constant, independent of the plasma current. Using this result, it can be easily shown that the resistivity is inversely proportional to the current density:

$$\rho_{bk} = \frac{1}{\sigma_{bk}} = \frac{E}{J} \tag{2.90}$$

where ρ_{bk} is the plasma bulk resistivity, $J = I_p/A_p$ is the plasma current density, and E is the electric field. Even when the agreement between the model prediction and the experimental data is good, figures 2.19 and 2.20 show some dispersion of the experimental data points around the constant electric field curve. This is due to the fact that Schottky's diffusion model (with the consequent constant electric field) does not fully apply to these types of discharges (see figure 2.21).

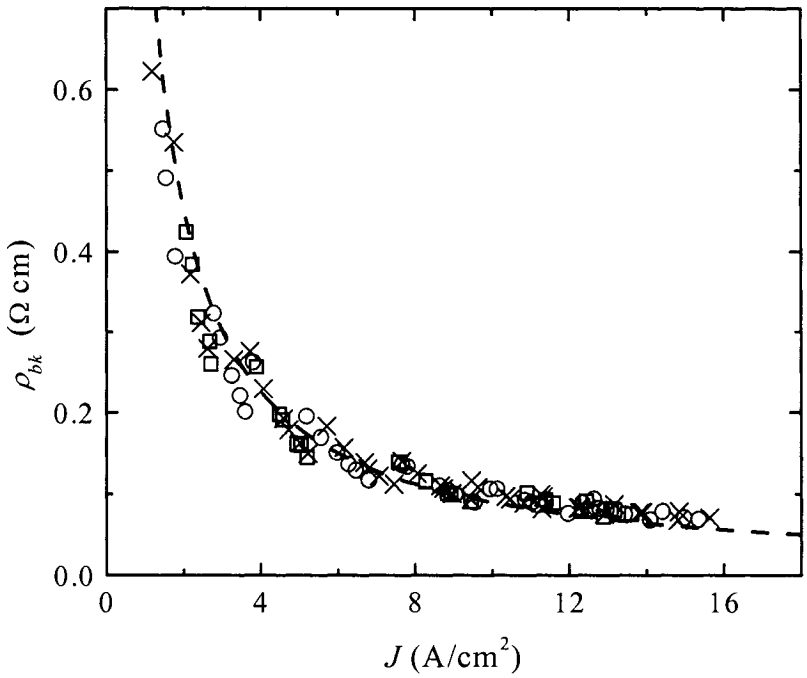

Figure 2.19. Plasma resistivity versus discharge current density for pressures between 250 mTorr and 10 Torr of argon. The blue squares (□), green circles (○) and the red crosses (×) correspond to chambers *"C"* (41.4 cm long), *"B"* (32.4 cm long) and *"A"* (22.4 cm long), respectively. The magenta dashed line results form equation (2.88) with $E = 0.9$ V/cm.

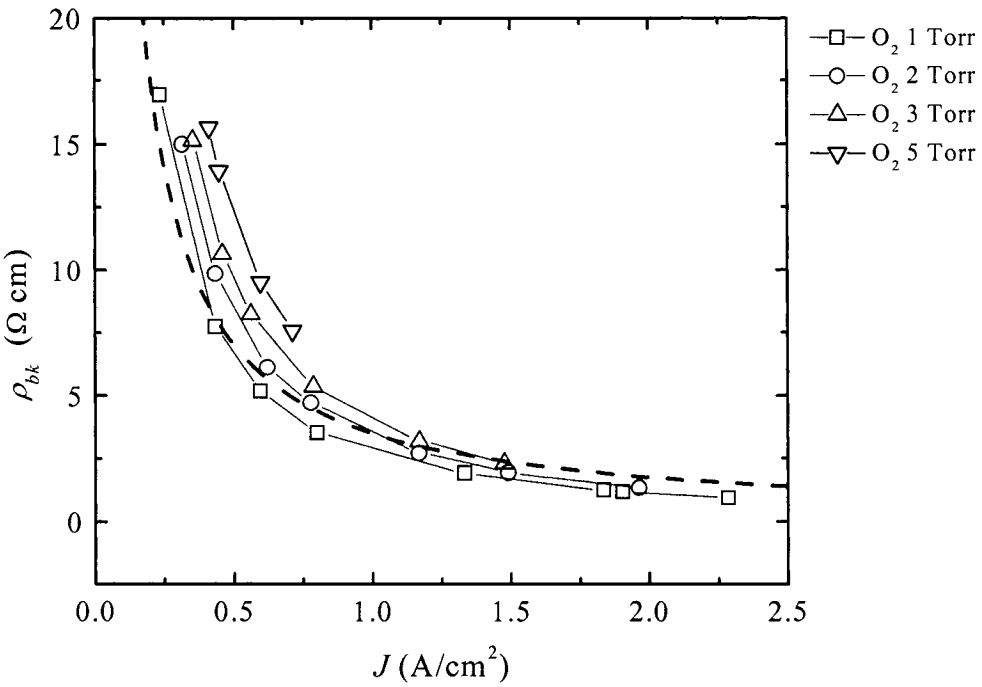

Figure 2.20. Plasma resistivity versus discharge current density for 4 slm and different pressures of oxygen. The magenta dashed line corresponds to equation (2.92) with $E = 3.5$ V/cm.

The assumption of a constant electric field holds well at low pressures and low plasma densities, where the plasma is mainly controlled by ambipolar diffusion losses. Under these conditions, the continuity equation (2.28) takes the form

$$n\nu_{iz}(T_e) = n\left(\frac{\chi_{01}}{R_p}\right)^2 D_a(T_e). \tag{2.91}$$

In this expression, the electron density cancels out, causing the discharge electric field value to depend only on the electron temperature. At the same time, the value of T_e

needs to be such that the diffusion and ionization rates are balanced in equation (2.91). The explicit dependence of the electric field with T_e is given by equation (2.39). This relation predicts an electric field that is constant with discharge current, i.e. a flat *E-J* characteristic.

However, as the electron density or current (power) increases, the electric field is no longer independent of the current (power), but increases as J (and P) increases, as shown in figures 2.21a and 2.21b. This is a regime in which recombination becomes important (Lowke et al. 1973; Denes and Lowke 1973; Eckert 1971). When recombination becomes the dominant loss process, the continuity equation (2.40) can be written as

$$n\nu_{iz}(T_e) = n^2 k_{rec}(T_e) \ . \tag{2.92}$$

In this case, the electron density does not cancel out, and the ionization rate must increase proportionally to it. Equation (2.57) shows the dependence of the electric field on n_0 (hence on current and power), which results in a positive *E-J* characteristic. The *E-J* characteristic for the argon plasmas conditions studied in this work shows that the electric field ($E = V_p/L_p$) increases with increasing current densities (figure 2.21a), indicating that recombination losses play an important role in the argon discharge's particle and power balance. This observation indicates that the particle conservation needs to be augmented to include a volume loss term with a dependence higher than linear on the electron density.

The overlapping of the data points in figures 2.21a and 2.21b for different discharge lengths indicates that the scaling of the plasma electrical parameters is largely independent of the length of the discharge and depends only on the power and current density, validating the long thin plasma approximation.

In contrast with the behavior observed in argon, the experimental data for oxygen presented in figures 2.22a and 2.22b shows that the electric field driving the discharge decreases as the current or power increases, giving the plasma a negative static resistance characteristic. The drop in E with increasing J is not explained by any of the previously presented models. Several authors, including Ecker and Zoller (1964), and Cohen and Whitman (1973) explained the negative E-J characteristic as the consequence of the heating and constriction of the plasma column. These effects become important at high currents, at the same time the uniform gas temperature profile assumption breaks down.

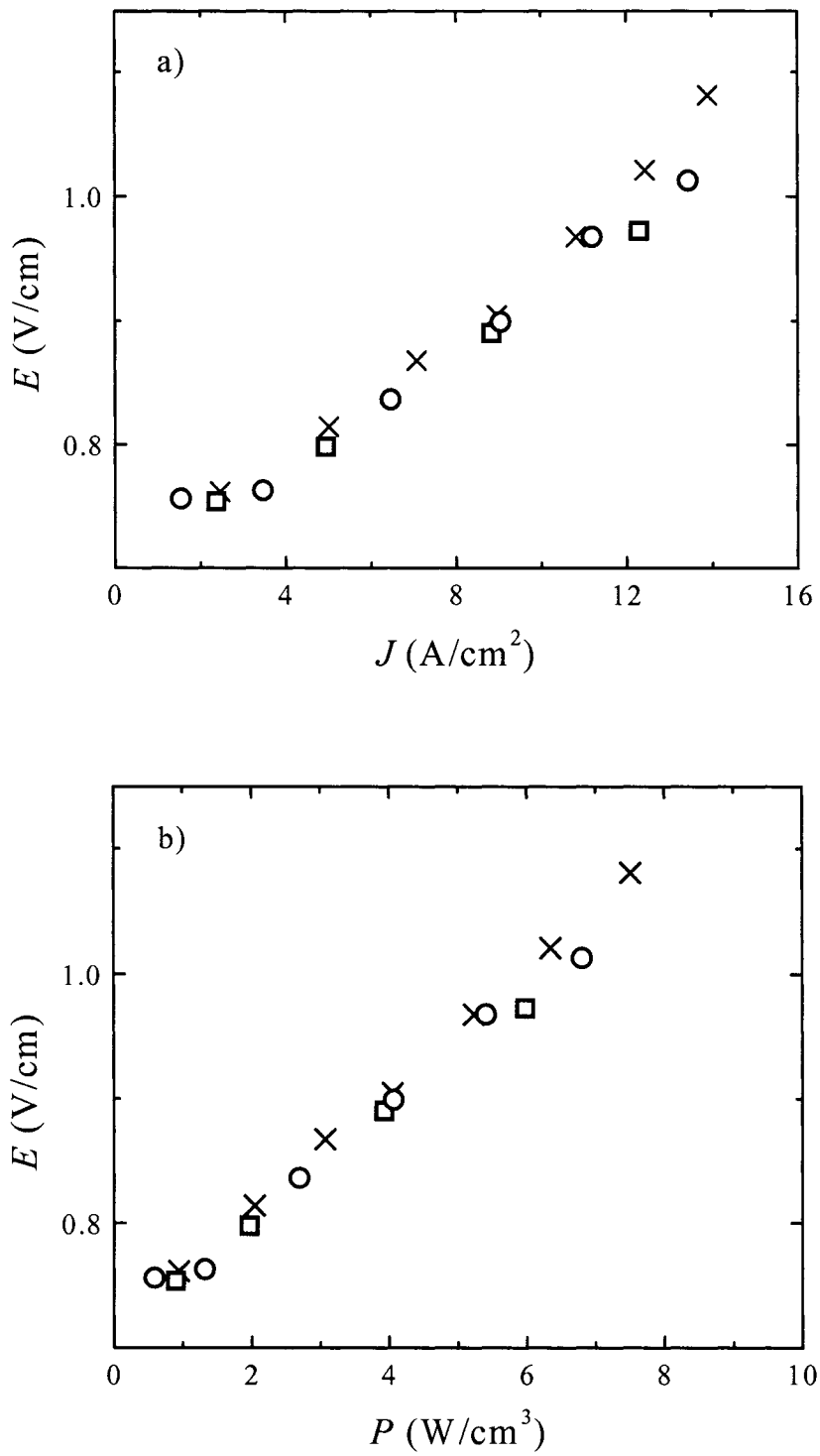

Figure 2.21. Axial electric field versus plasma current density (a) and power density (b) for a 1 Torr argon discharge. The red crosses (×), green circles (○) and the blue squares (□) correspond to data from discharge tubes *"C"* (41.4 cm), *"B"* (32.4 cm) and *"A"* (22.4 cm), respectively.

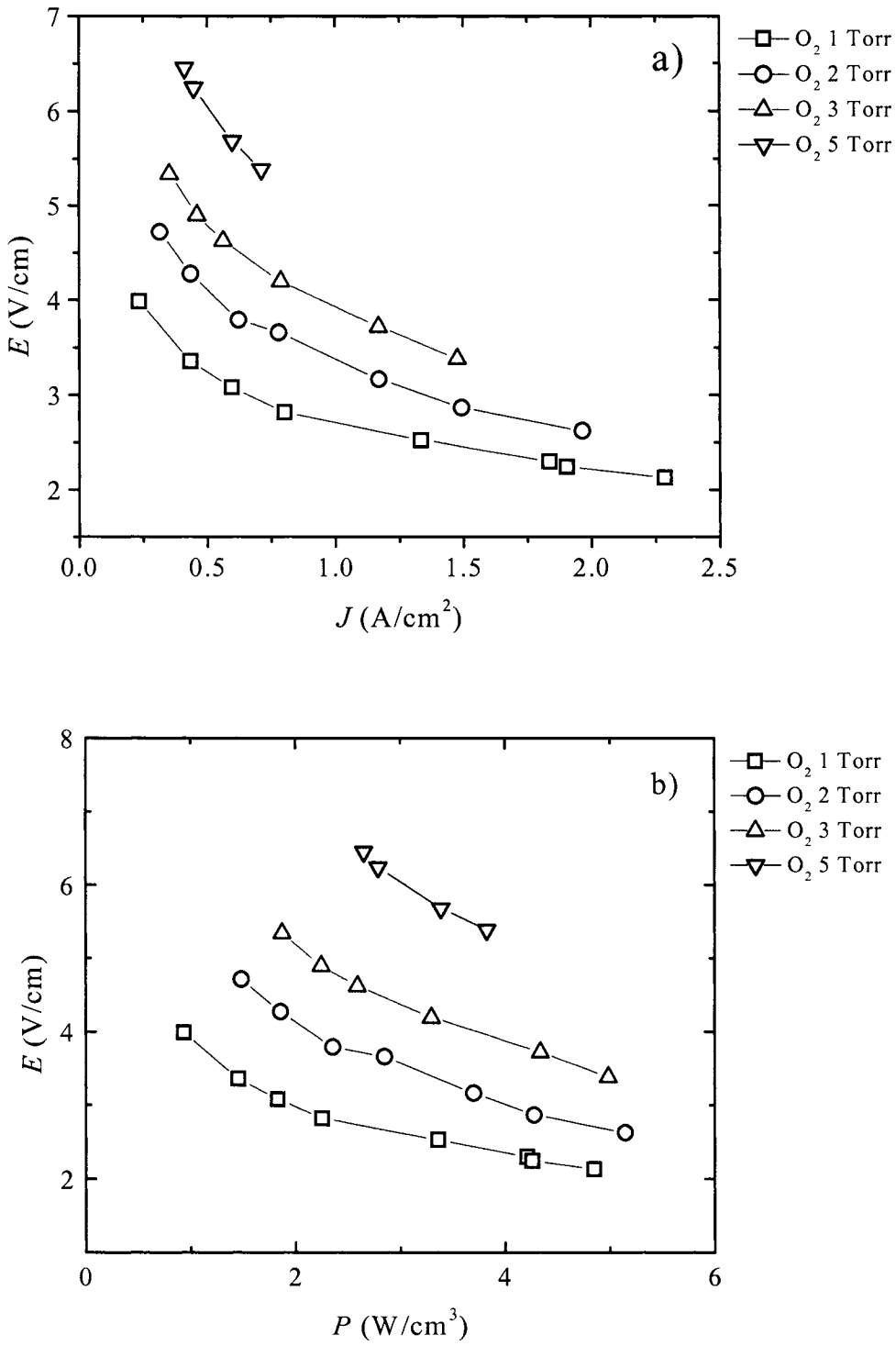

Figure 2.22. Axial electric field versus plasma current density a) and power density b) for 4 slm of oxygen flow at different pressures.

Figure 2.23 shows the measured plasma axial electric field $E = V_p/L_p$ as a function of argon pressure for different powers. At fixed power, the electric field initially decreases to reach a minimum value at about 3 Torr, and then start to increase with pressure. For $R_p = 8$ mm radius chambers, diffusion losses in argon start to dominate the discharge at pressures below approximately 2 Torr. Notice that this transition is not observed in the oxygen data (Fig. 2.22). For the oxygen discharge, this transition is expected to occur at a much lower pressures due to the larger chamber diameter and a smaller ambipolar diffusion. As the gas pressure decreases the diffusion losses rise, forcing the electron temperature (see figure 2.33) and hence the electric field to increase to keep the ionization rate balanced with the increasing losses. For pressures over 3 Torr, recombination becomes the dominant loss mechanism. Given that recombination and ionization rates are both proportional to the gas density, there is no need to balance the recombination rate by raising the electron temperate as pressure increases, therefore the electron temperature stays approximately constant (see figure 2.33). However, the electric field still increases, driven by the increase in pressure (see Eq. 2.57).

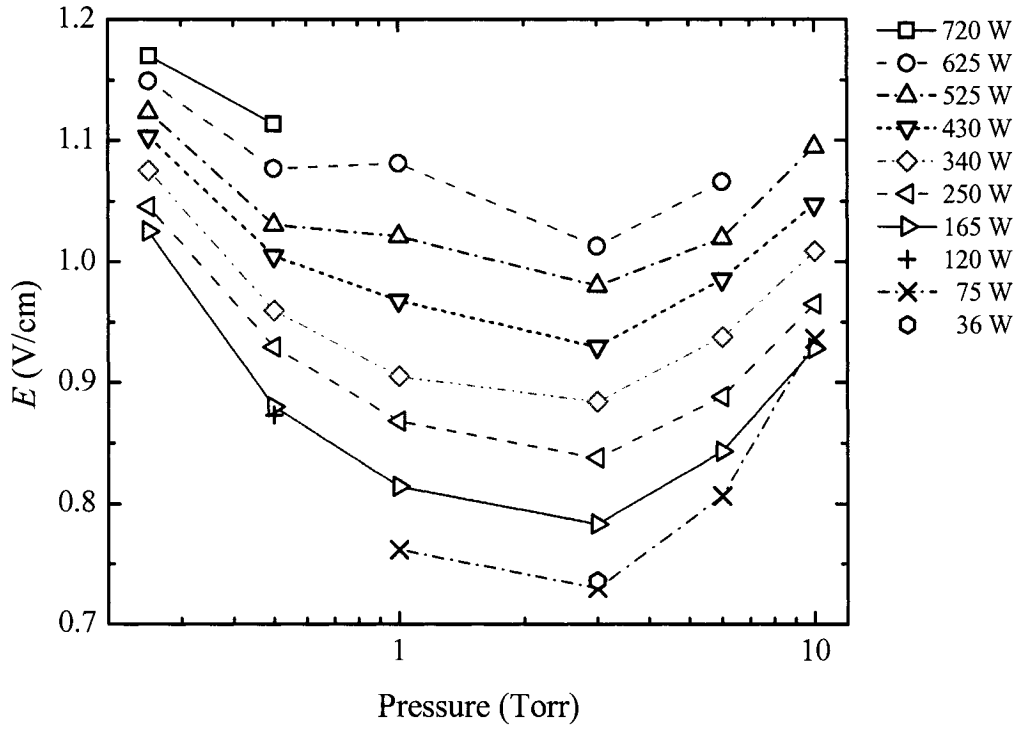

Figure 2.23. Argon discharge electric field for discharge tube *"C"* as a function of pressure for different power levels.

The plasma current density as a function of pressure shows a maximum at approximately 3 Torr, the same point where the electric field reaches its minimum value (Fig. 2.24). At the same pressure, the plasma conductivity shows a corresponding maximum (Fig. 2.25). The Langmuir probe measurements described in the next Section show that at this point the plasma density reaches its maximum value for a given plasma power (see for example Fig. 2.26), meaning that the total losses (diffusion plus recombination) reach a minimum.

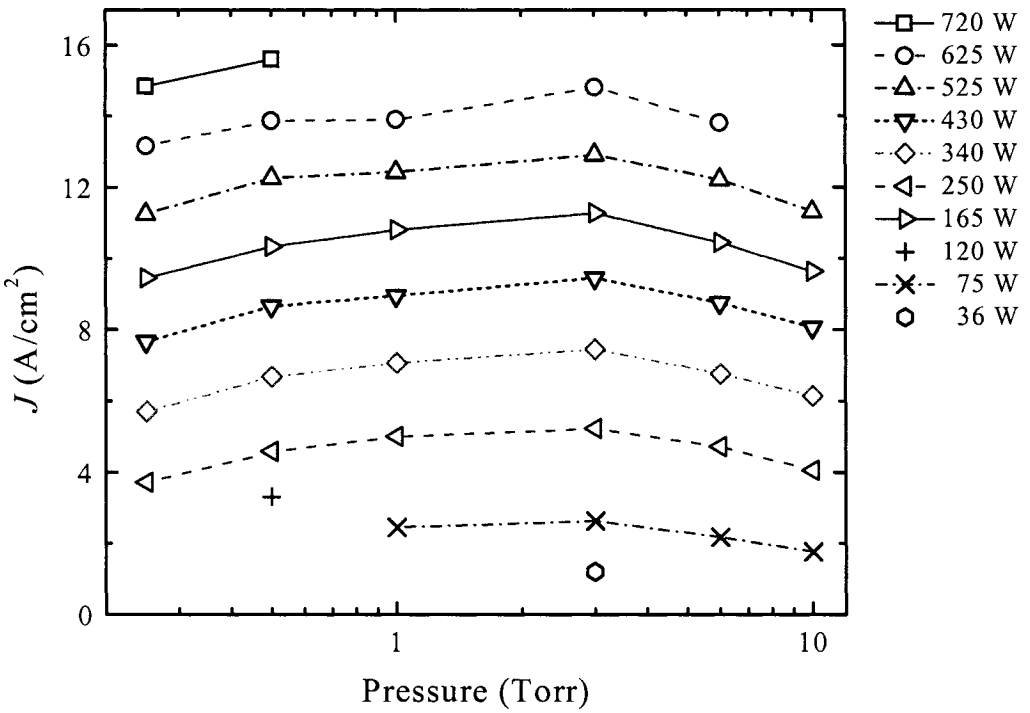

Figure 2.24. Argon discharge current density for discharge tube *"C"* as a function of pressure for different power levels.

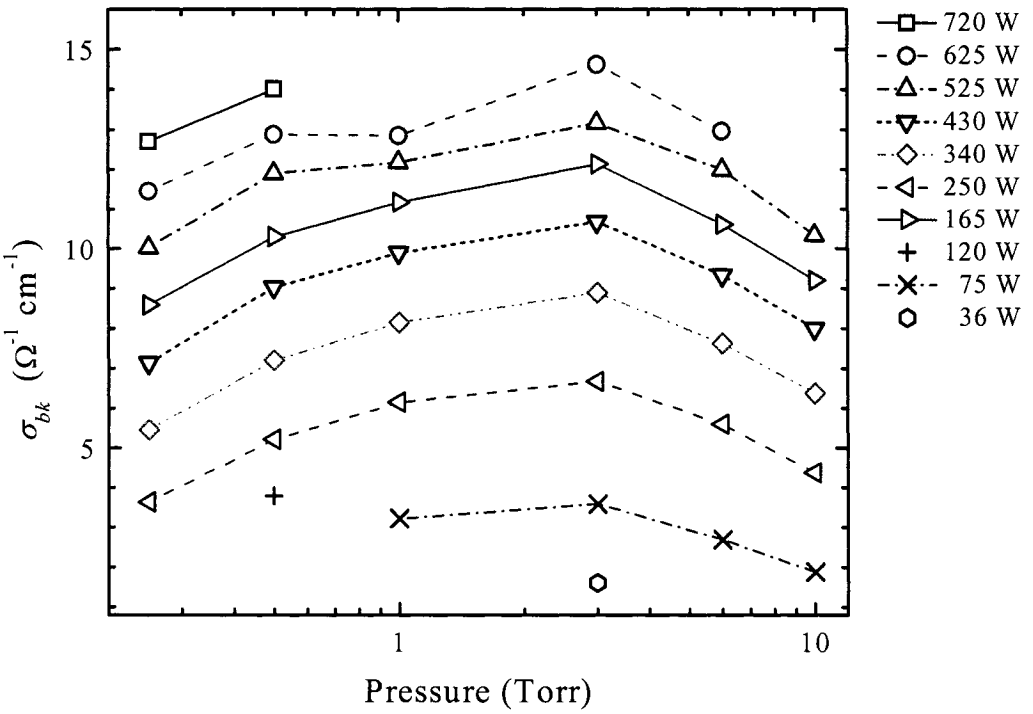

Figure 2.25. Plasma conductivity for discharge tube *"C"* as a function of pressure for different power levels in an argon discharge.

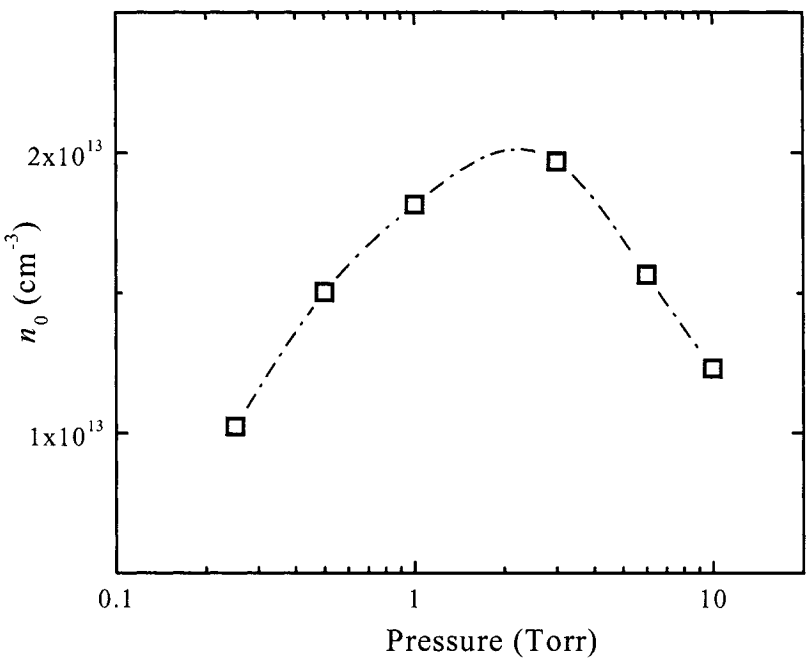

Figure 2.26. Measured electron density in discharge tube *"C"* versus pressure for a 250 W argon plasma.

Both the slope of the *E-J* curves and the non-monotonic characteristics of the current density and electron density as a function of pressure indicate that simple diffusion models are not adequate to describe the experimental behavior of TCTDs in the range of interest. In the next Section, we will compare the plasma density experimental measurements to the predictions obtained from the different models presented in Section 2.3. Utilizing the electrical measurements, presented in the previous Sections as an input to the different plasma models, estimations for the electron temperature and the dominant loss mechanisms as a function of the plasma conditions will be obtained.

2.5.3. Electron density measurements

Using the experimental electrical data as the input parameters for the models described in Section 2.3, the electron temperature and plasma density in an argon discharge were calculated for a range of plasma powers and pressures. The results for electron density from the different models were then compared to the electron density values obtained from the ion saturation current measurements to check the accuracy of the theoretical predictions.

a. Comparison with the ambipolar diffusion (Schottky) model.

This model was described in Section 2.3.1 and is used here as a starting point because of its simplicity. In this approximation, the electron temperature and density can be obtained separately by using the boundary condition of equation (2.31) and the power balance equation (2.34). Figure 2.27 shows that the model fails in predicting the correct electron density values. However, it will be later shown that it still provides reasonable estimates for the electron temperature. The normalized difference between measured and predicted electron density values for different power conditions is shown in figure 2.28. The vertical spread in the data points is due to gas heating (i.e. higher power, higher gas temperature, less gas density). Notice that the error in the prediction of the electron density increases with the gas pressure (or more precisely with the gas density), indicating the lack of a loss mechanism proportional to the gas density (see equation 2.48).

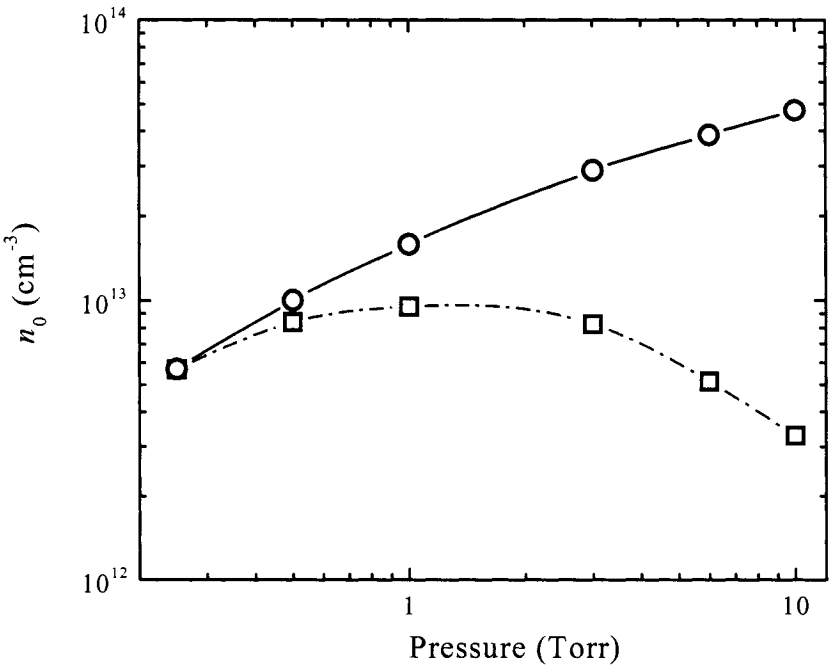

Figure 2.27. The peak electron density predicted by a pure diffusive model (blue circles) does not match the experimental data (red squares), breaking down at high pressures. (Argon, 165 W, tube *"C"*).

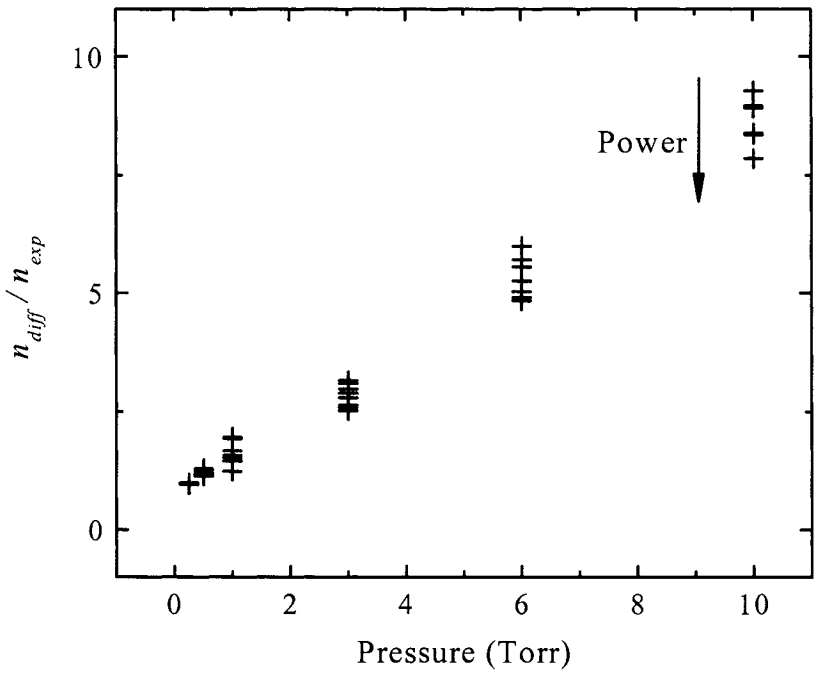

Figure 2.28. Overestimation of the plasma density by the diffusion model versus pressure for all pressures and powers in tube *"C"*.

b. Semi-Global model with power as the input.

As was explained in Section 2.3.2 and confirmed by the experimental data in Section 2.5.1, recombination plays a fundamental role in the physics of TCTP discharges. The equations for the plasma density and electron temperature for a spatially semi-averaged model, which includes diffusion and recombination losses, were derived in Section 2.3.3. Unfortunately, and due to the intrinsic nonlinearity of the recombination term that couples the equations for the electron temperature and density, no analytical solution can be found for this case. In Section 2.3.4, we introduced a method that decouples the calculations for the electron temperature and the average plasma density from the density profile. In this iterative approach, equations (2.73) and (2.74) are first

numerically solved assuming a Bessel spatial distribution. These results are then utilized to obtain the electron density profile integrals (A_{eff}, B_{eff}) and the effective diffusion length (d_{eff}) from equations (2.70), (2.71) and (2.72) respectively. The solutions to these equations were previously tabulated as a function of the normalized peak density $\overline{n}_0$ (see Table 2.1). The density profile information is then fed back into equations (2.73) and (2.74), where the electron temperature and density are recalculated. This procedure is repeated until convergence is reached. The only non-specified parameter in this calculation is the effective recombination constant α_{eff}, the value for which was selected to minimize the error in the electron density calculations against the experimental data.

The inclusion of the recombination term produces a drastic improvement against the diffusion model in predicting the plasma density. This is illustrated in figures 2.29, 2.30 and 2.31, where the values for the calculated plasma density are within a factor of two for all the experimental data points. The model was fitted to the experimental data using $\alpha_{eff} = 5\times10^{-44}$ cm^9/s for the effective recombination coefficient [a value that is within the range found in the literature(Appendix B.5)].

The proportionality of the electron density with power is exemplified in figure 2.30, where we observe a linear increase of electron density with the power deposited into the plasma.

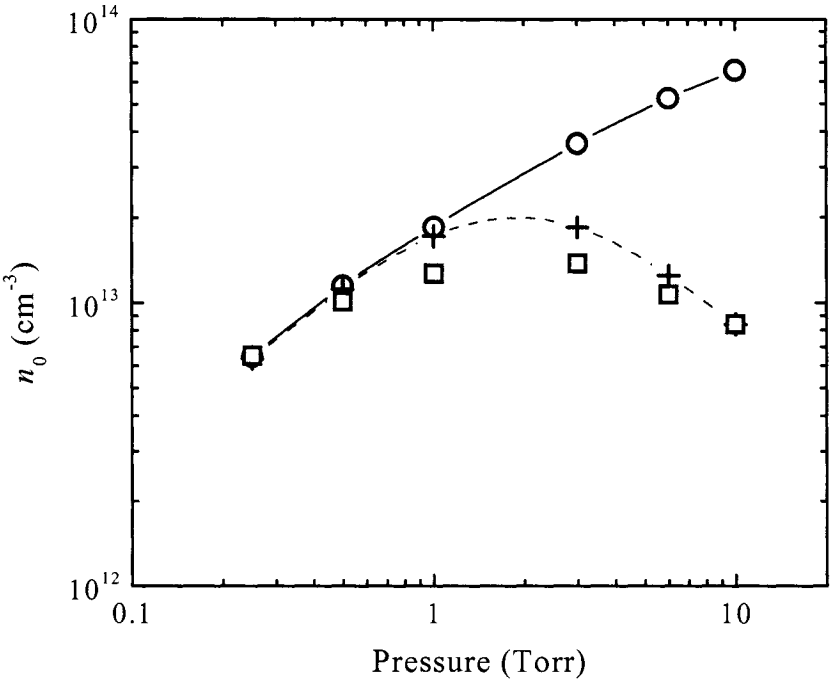

Figure 2.29. Comparison between experimental data and the predictions from both a purely diffusive and a diffusion + recombination model. (Argon, 165 W, tube *"C"*). The red squares represent the experimental points, the blue circles with a solid line correspond to the diffusion model and the green crosses with the dashed line correspond to the full (diffusion + recombination) model with an effective recombination coefficient of $\alpha_{eff} = 5\times10^{-44}$ cm^9/s.

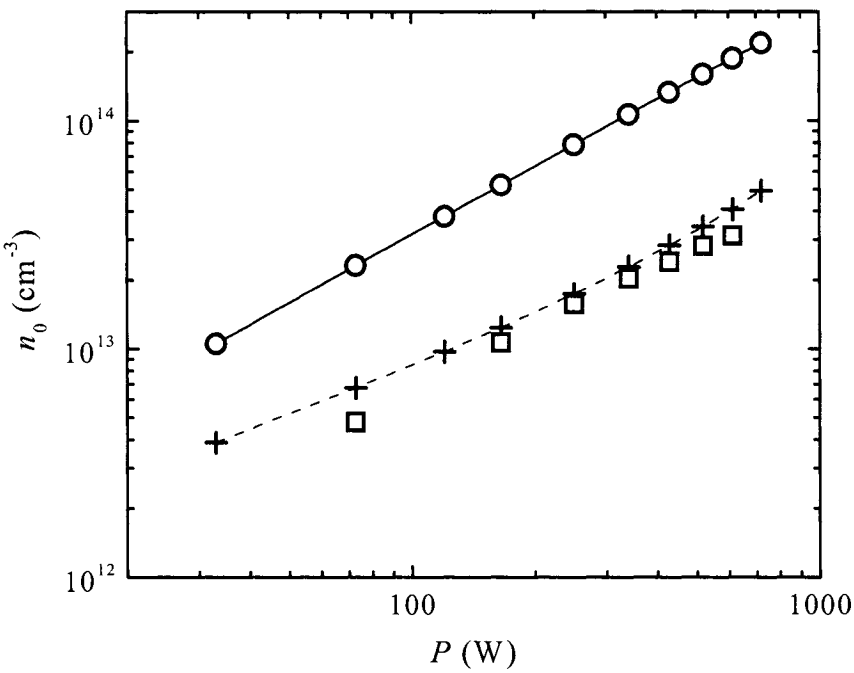

Figure 2.30. Electron density versus power for a 6 Torr argon discharge. The red squares represent the experimental points, the blue circles with a solid line correspond to the diffusion model and the green crosses with the dashed line correspond to the full (diffusion + recombination) model with an effective recombination coefficient of $\alpha_{eff} = 5\times10^{-44}$ cm^9/s.

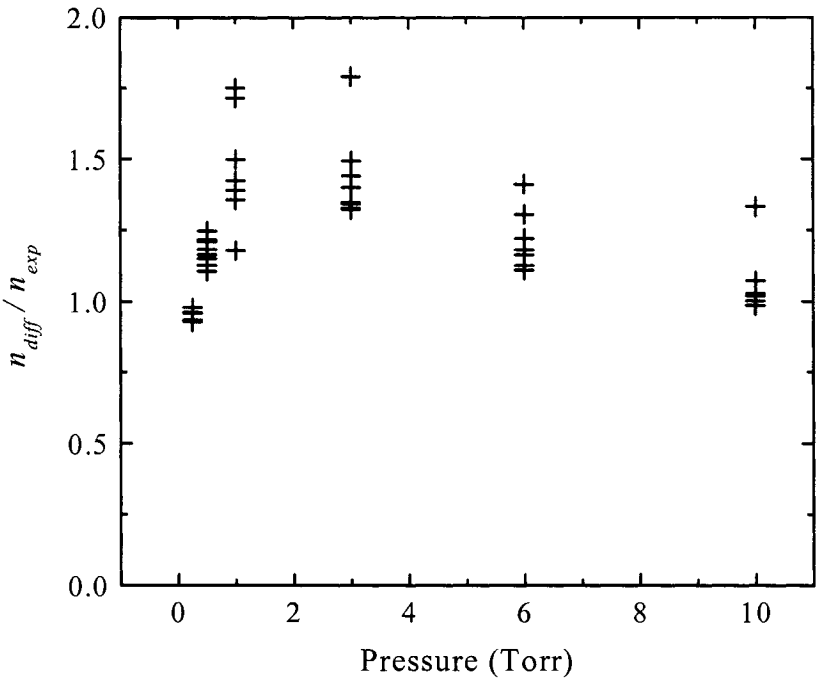

Figure 2.31. Relative difference between the predicted (full model) and measured electron densities as a function of pressure for all the experimental measurements in tube *"C"*.

Solving equations (2.73) and (2.74) under the assumption of a zero-order Bessel function for the electron density spatial distribution results in a good approximation for the electron temperature and average plasma density (equations 2.59 and 2.60). Although this method yields similar results for the average plasma density and the electron temperature (figure 2.33), it tends to overestimate the effective recombination coefficient.

As pressure and power increase, recombination losses rise, making the electron density profile flatter. To analyze the interplay between diffusion and recombination we use the normalized dimensionless peak electron density $\overline{n}_0$ as an indicator of the degree of recombination occurring in the discharge (notice that $\overline{n}_0 = 0$ corresponds to no

recombination with a Bessel-shaped density profile, while $\overline{n}_0 = 1$ corresponds to the case where all losses are due to recombination). The previous analysis of the experimental data defined the region between 2 and 3 Torr as the point where recombination losses start to dominate over the diffusion losses. In figure 2.32, we can see that $(1-\overline{n}_0)$ value stays constant in the diffusion-dominated regime, abruptly dropping for pressures higher than 1 Torr. It is also evident from this figure that the dependence with power is much weaker than the dependence with pressure, leveling off for powers higher than 300 W. The slight increase with power for values higher than 300 W is due to the decrease in gas density caused by gas heating.

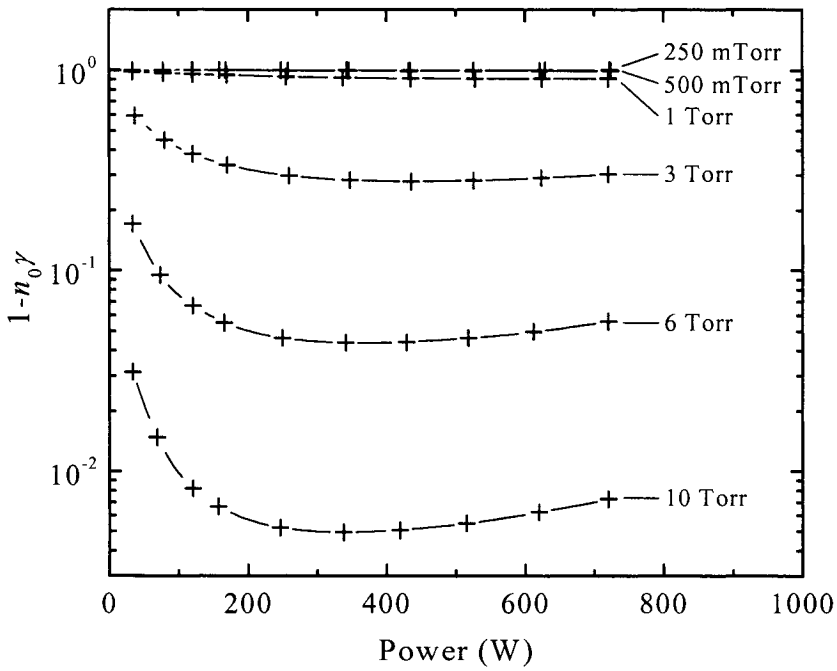

Figure 2.32. Complementary dimensionless peak electron density $1-n_0\gamma$ versus power. A value of $1-n_0\gamma = 1$ $(n_0\gamma = 0)$ means only diffusion losses, while $1-n_0\gamma = 0$ $(n_0\gamma = 1)$ represents only volume losses.

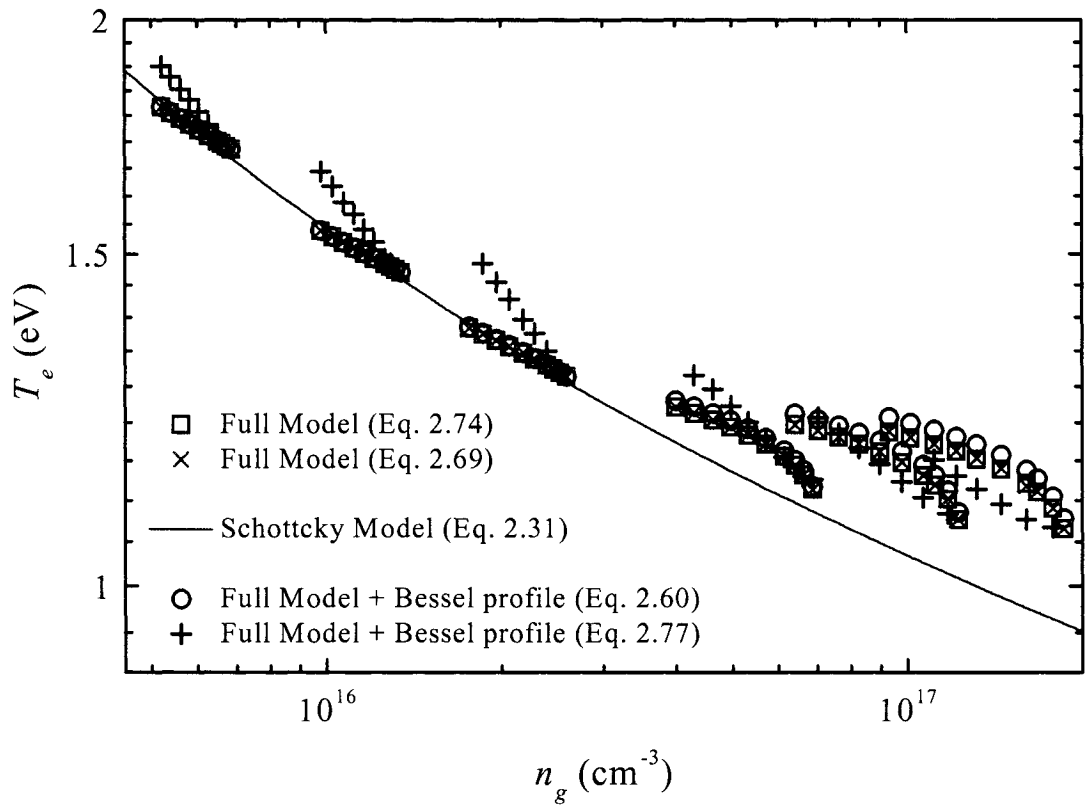

Figure 2.33. Calculated electron temperatures versus gas density as obtained by different calculation methods, for all experimental points. The green solid line (▬) is the electron temperature calculated from equation (2.31), which only considers diffusion losses (Schottky Model). The olive crosses (+) represent the electron temperate obtained from equating expression (2.77) to the experimental electric field and assuming a zero order Bessel distribution for the electron density spatial distribution. Red circles (○) are the electron temperature obtained from (2.60). This solution assumes a zero order Bessel electron density profile and three-body recombination volume losses. The blue squares (□) are the numerical solutions to equation (2.74), which accounts for recombination losses. The cyan crosses (×) represent the solutions to (2.69), a generalization of (2.31) that includes recombination.

2.5.4. Analysis of predicted electron temperatures

The values predicted for electron temperature from different calculation methods are presented in figure 2.33. The solid green line corresponds to the electron temperature

calculated using the boundary condition (2.31) for a diffusion-dominated plasma (Schottky model). Equation (2.31) only requires knowledge of the discharge tube radius and pressure to predict the electron temperature value.

The electron temperatures represented by the red circles in the same figure were obtained by equating the measured plasma input power to the power obtained from the energy balance equation (equation 2.60), which assumes a Bessel radial electron distribution function. When the corrected radial electron distribution function is utilized in the energy balance equation (2.74) (instead of a zero-order Bessel function), similar results are obtained for pressures below 3 Torr. This is not surprising since for these pressures the discharge is still governed by diffusion loses and, consequently, the electron density profiles resembles a Bessel function. As pressure increases and recombination losses begin to dominate the discharge, the values predicted by equation (2.60) slightly overestimate the electron temperature. To verify the self-consistency of the numerical model, the electron temperature obtained from equation (2.74) was compared with the electron temperature obtained from equation (2.69), which is the generalization of boundary condition (2.31) for plasmas with both diffusion and recombination losses. The observed agreement over the entire pressure range corroborates the self-consistency of the numerical model.

The remaining set of points in figure 2.33, indicated by the olive crosses, represent the electron temperature obtained by equating the axial electric field predicted by equation (2.77), which accounts for diffusion and recombination losses, to the

experimental measurements of the electric field. In this calculation, the spatial electron density profile was approximated by a zero-order Bessel function. There is a very good agreement between the electron temperature values obtained from the electric field and those obtained from the total power absorbed by the plasma. This result coincides with the good agreement obtained between the calculated electrical discharge parameters and the experimentally measured electrical parameters (see Section 2.5.5).

Overall, all five methods provide reasonable estimates of the discharge electron temperature. The agreement between the Schottky model predictions and the other calculations is rather unexpected, since equation (2.31) neither accounts for volume losses, nor utilizes any external data except the gas density and the radius of the discharge tube. For high gas densities (over 6 Torr), equation (2.31) begins to deviate from the temperatures obtained from the energy balance equation and the measured plasma power by underestimating the electron temperature.

2.5.5. Self-consistency check: comparison of measured and predicted plasma resistance

Both electrical and plasma density measurements have shown that the simple diffusion model is not adequate to describe the experimental behavior of TCTDs. The plasma measurements have further indicated that the full model results in satisfactory predictions for the electron density. However, it is not yet clear that the predictions of the full model will result in accurate values for the electrical parameters of the discharge,

such as plasma resistance. The relationship between plasma resistance and average electron density expressed by equation (2.11) allows us to connect the data presented in Sections 2.5.2 and 2.5.3 and demonstrate the self-consistency of the full model. Inserting the solution for the electron density obtained from solving equations (2.73) and (2.74) for given plasma power into (2.11) lets us predict the plasma resistance as a function of gas pressure and plasma power, provided that the dependence of the electron transport collision frequency (ν_e) on pressure is known. Figures 2.34 to 2.36 show how the experimental and predicted values for the plasma resistance, current and voltage as a function of pressure compare for a given power. For the calculations, we used the expression of ν_e as a function of pressure obtained by Godyak et al. (1999) in an air-coupled ICP (see Appendix B.4).

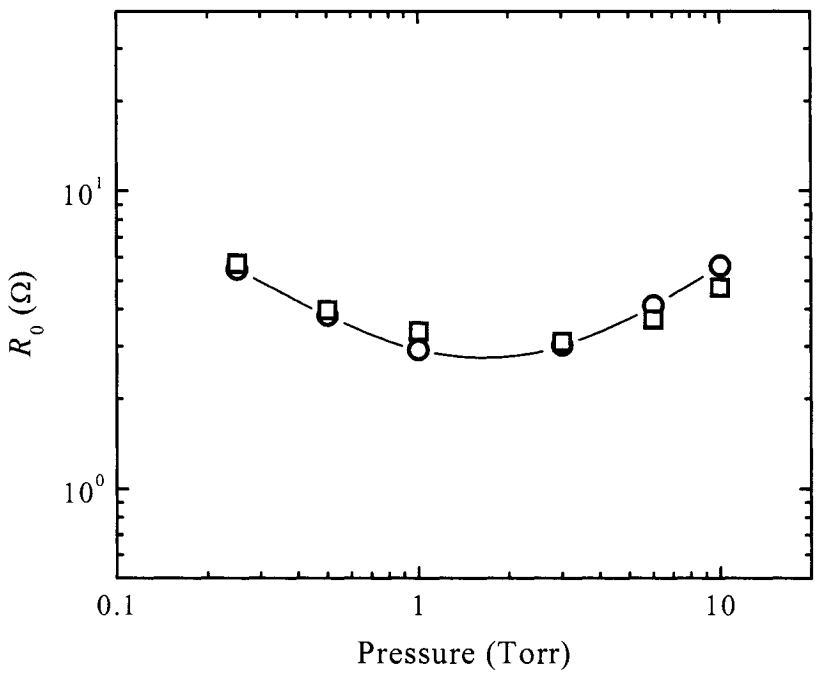

Figure 2.34. Experimental and calculated plasma resistance as a function of pressure for an argon plasma on discharge tube *"C"* (power: 165W). The red squares represent the experimental points; the blue circles with a solid line correspond to the model predicted values.

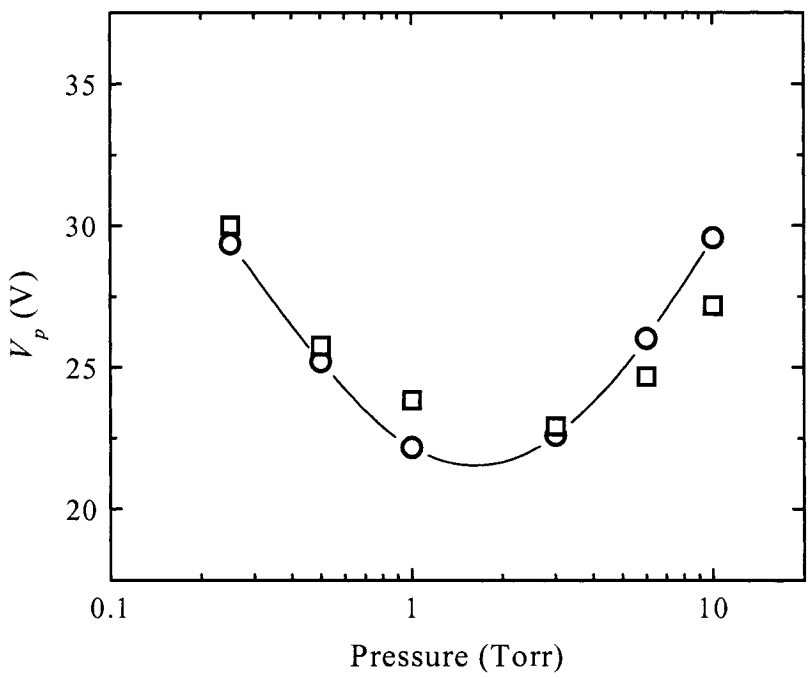

Figure 2.35. Experimental and calculated plasma voltage as a function of pressure for an argon plasma on discharge tube *"C"* (power: 165 W). The red squares represent the experimental points; the blue circles with a solid line correspond to the model predicted values.

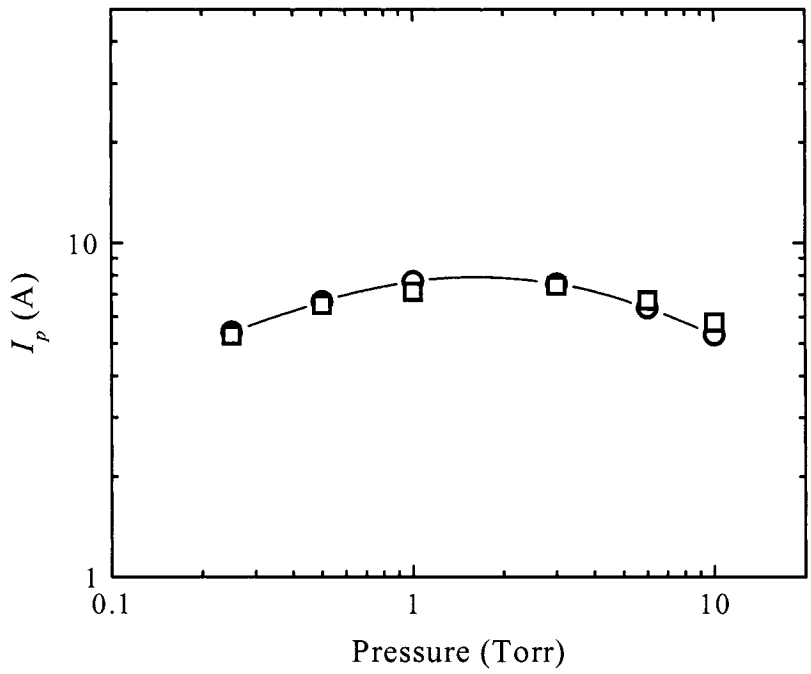

Figure 2.36. Experimental and calculated plasma current as a function of pressure for an argon plasma on discharge tube *"C"* (power: 165W). The red squares represent the experimental points; the blue circles with a solid line correspond to the model predicted values.

The preceding figures are a typical representation of the good agreement between model and experiment. As was shown, the predictions of the full model resulted in accurate values for the electrical parameters of the discharge, demonstrating the self-consistency of the full model. Similar plots for the remaining experimental data are presented in Appendix B.

2.5.6. Further discussion of recombination terms

As described in Section 2.3.2 and experimentally confirmed in Section 2.5, for high discharge pressures an accurate description of the losses requires the inclusion of mechanisms other than diffusion, such as volume recombination. Volume recombination comprises a wide set of microscopic mechanisms that provide a path for electrons and ions to decay to the neutral ground state. Examples of these processes are dissociative recombination, radiative recombination, 3-body electron recombination and 3-body atom recombination, among others. In our model, all these processes were lumped together into an effective recombination term, making the model independent of the details of the recombination process. The effective recombination constant in equation (2.43) is the only free parameter of the full model.

Among the most probable recombination process for the conditions under study in this thesis (see Appendix B.5 for a detailed description of the different possible recombination process been considered), dissociative recombination stands as the dominant recombination loss channel. Dissociative recombination occurs when a molecular ion and an electron make a radiation less transition to an unstable molecule, which causes the atoms forming the molecule to gain kinetic energy and come apart due to their mutual repulsion:

$$XY^{+} + e \leftrightarrow (XY)^{*} \rightarrow X + Y^{*}. \tag{2.93}$$

Figure 2.37 shows a comparison of the expected spatially averaged electron recombination loss frequency for the different recombination processes along with the calculated spatially averaged effective electron recombination loss frequency

$$\langle \nu_{rec} \rangle = B_{eff}\, k_{rec}\, n_{+}, \tag{2.94}$$

and the ambipolar diffusion loss frequency

$$\langle \nu_{D_a} \rangle = \frac{D_a}{d_{eff}\, R_p^{\,2}}, \tag{2.95}$$

as a function of power. From these curves, it is clear that the most important recombination process is dissociative recombination, with no significant contribution from other recombination channels.

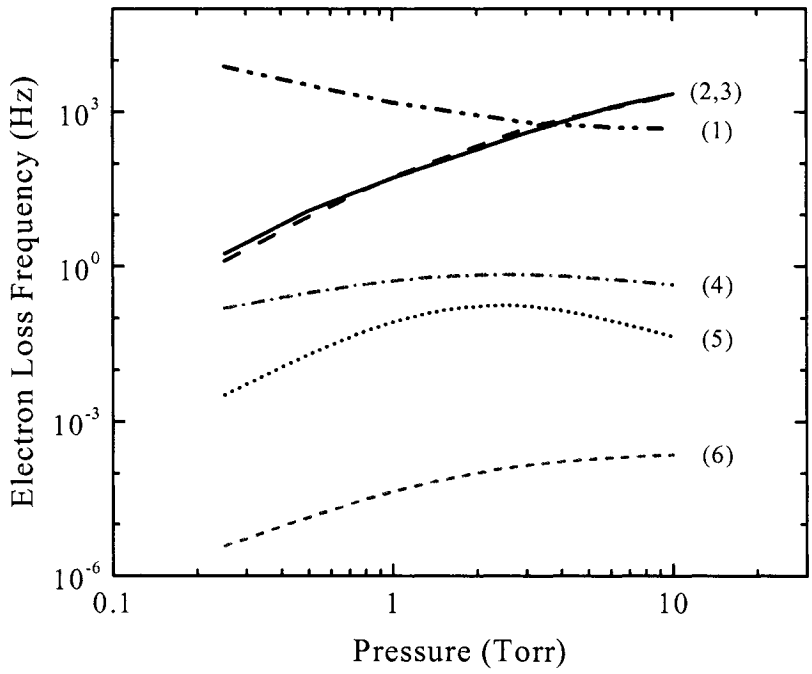

Figure 2.37. Spatially averaged electron loss mechanism as a function of pressure for a 160 W argon plasma. (1) Ambipolar diffusion (Blue dash-dot dot line), (2) effective recombination (red solid line), (3) dissociative recombination (green dashed line), (4) radiative recombination (cyan dash-dot line), (5) 3-Body electron recombination (magenta doted line) and (6) 3-Body atom recombination (orange dashed line).

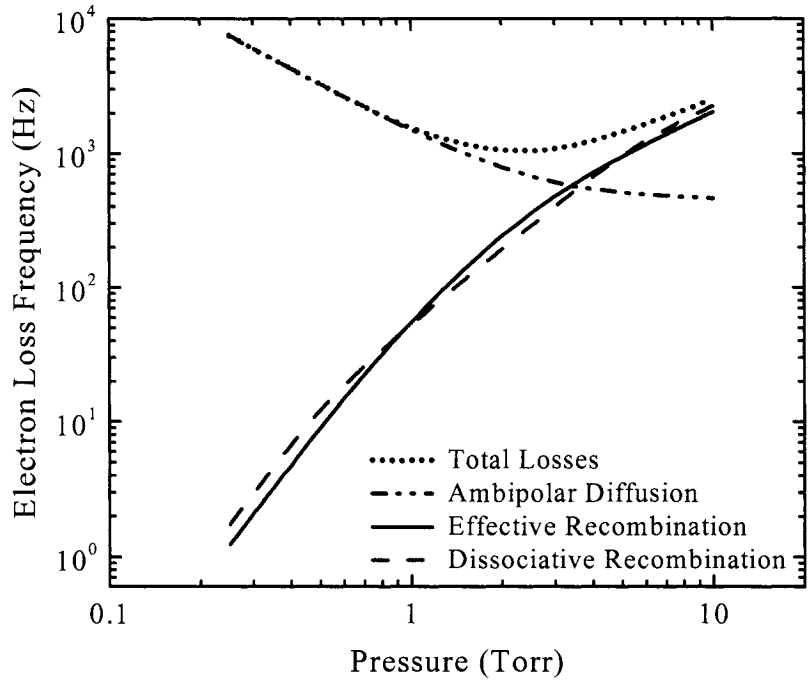

Figure 2.38. Comparison of the spatially averaged electron loss frequencies as a function of pressure for total (grey dotted line), ambipolar diffusion (Blue dash-dot line), effective recombination (red solid line), and dissociative recombination (green dashed line) losses (Argon plasma, power: 250W).

Figure 2.38 compares the electron loss frequency as a function of pressure for different loss mechanisms for argon plasma at 250 W. Here again the dissociative recombination mechanism, accurately described by the effective recombination approximation, appears as the dominant loss. The dominant role of diffusion losses at low pressures and dissociative recombination losses at higher pressures is clearly illustrated in both figures 2.37 and 2.38. The location of the transition point between diffusion- and volume-controlled discharges at a pressure of around 2-3 Torr coincides with the estimations made from the electrical and electron density data. Figure 2.39 illustrates how the spatially averaged effective recombination term (Eq. 2.94) utilized in

the numerical model compares with the expected spatially averaged dissociative recombination electron loss frequency (Eq. b.34) as a function of power for argon discharges at relatively high pressures. At these pressures, ambipolar diffusion is never relevant within the power range explored in our experiments.

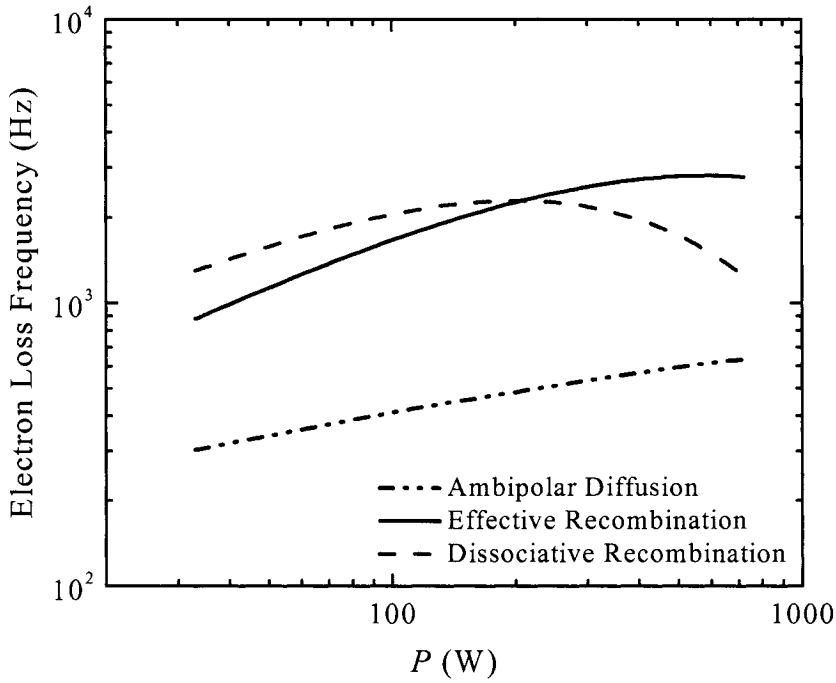

Figure 2.39. Ambipolar diffusion (Blue dash-dot line), effective recombination (red solid line) and dissociative recombination (green dashed line) spatially averaged electron loss frequencies as a function of power for a 10 Torr Argon plasma.

2.6. Conclusions

In this Chapter, TCTDs were analyzed from both purely circuital and microscopic points of view. For all conditions surveyed, the plasma impedance was observed to be real and inversely proportional to the electron density. In a first approximation, the

electric field can be considered independent of both power (current) and pressure, assuming an approximately constant value of 0.9 V/cm for the argon experiments and 3.5 V/cm for the oxygen discharges. A closer look at the dependence of the electric field on other discharge parameters showed that argon discharges exhibit a positive V-I characteristic that cannot be explained by a simple diffusion model, but that could be modeled by including a volume recombination term. In contrast, oxygen discharges showed a negative V-I characteristic in the range of conditions studied, likely due the heating and constriction of the plasma column.

Since diffusion losses are inversely proportionally to the gas pressure but volume losses are proportional to the gas pressure, a peak in the electron density or a minimum in the particle loss rate occurs approximately at 2 Torr where, for our experimental conditions in the argon plasmas, the diffusion losses are equal to the volume losses. This point also corresponds to a minimum in the electric field and maxima in the plasma current and plasma conductivity for constant discharge power.

Two models that included diffusion and volume recombination losses successfully matched the plasma density measurements in argon. The first model assumed a Bessel spatial electron distribution profile, while the second model provided the electron density distribution as part of the solution. Although both models result in similar values for electron peak densities, the effective recombination rates needed to fit the first, simpler model to the experimental data was noticeable higher that the values

reported in the literature. In contrast, the more elaborate model matches the experimental data using a value for the effective recombination rate within the published range.

Three different methods were utilized to estimate the plasma electron temperature. The predicted values from all models agree within 0.1 eV, ranging from about 2 eV at low pressures to about 1 eV at high pressures. The fact that models based on different assumptions results in similar predicted values for the electron temperature indicates that this quantity is mainly controlled by the ionization rate.

Finally, we were able to identify dissociative recombination as the most probable loss mechanism at high pressures.

In summary, this Chapter shows that most of the experimental behavior of TCTDs can be satisfactorily interpreted by the use of simple models based on general assumptions and experimental insight. These simple models constitute a first step in understanding the basic physics of TCTDs, and can be used both as an input for more elaborate models and as a guide for design and operation of these discharges.

2.7. References

Akhtar K., Scharer J. E., Tysk S. M. and Kho E. (2003), *Rev. Sci. Instrum.* **74**, 996-1001.

Bates D. R. and Khare S. P. (1965), *Proc. Phys. Soc.* **85**, 231-243.

Bhave R. N. and Cooper R. (1995), *Aust. J. Phys.* **48**, 503-513.

Bogdanov E. A., Kolobov V. I., Kudryavtsev A. A. and Tsendin L. D. (2002*), Technical Physics* **47**, 946–954.

Chevolleau T. and Fukarek W. (2000), *Plasma Sources Sci. Technol.* 9, 568-573.

Cohen I. M. and Whitman A. M. (1973), *Phys. Fluids* **16**, 307-314.

Denes L. J. and Lowke J. J. (1973), *Appl. Phys. Letters* **23**, 130-132.

Denneman J. W. (1990), *J. Phys. D: Appl. Phys.* **23**, 293-298.

Donnelley V. M. and Malyshev M. V. (2000), *Appl. Phys. Lett.* **77**, 2467-2469.

Ecker G. and Zoller O. (1964), *Phys. Fluids* **7**, 1996-2000.

Eckert H. U. (1971), *AIAA Journal* **9**, 1452-1456.

Eliason B. and Kogelschatz U. (1986), *Basic data for modeling of electrical discharges in gases: oxygen. Report KLR 86-11C*, Brown Boveri Konzernforschung, CH-5405 Baden.

Erickson R. W. and Maksimovic D. (2001), *Fundamentals of Power Electronics 2nd ed.*, Kluwer Academic Publishers, Norwell.

Francis G. (1956), The Glow Discharge at Low Pressures, in *Handbuch der Physik*, edited by S. Flügge, Vol. **XXII**, Springer-Verlag, Berlin.

Franklin R. N. (1976), *Plasma Phenomena in Gas Discharges*, Claredon Press, Oxford.
Godyak V. A., Piejak R. B. and Alexandrovich B. M. (1999), *J Appl.* Phys. **85**, 3081-3083.

Godyak V. A. and Sternberg N. (1990), *IEEE Trans. Plasma Sci.* **18**, 159- 168.

González J. J., Shaw, D. M., Watanabe, M., Uchiyama, H. and Collins, G. J. (2000), *Electrical model of an inductive ring discharge in argon, 53rd Annual Gaseous Electronics Conference*, Houston, Texas, Oct 24-27.

Gudmundsson J. T., Kouznetsov I. G., Patel K. K. and Lieberman M. A. (2001), *J. Phys. D: Appl. Phys.* **34**, 1100–1109.

Hebner G. A. (1996), *J Appl. Phys.* **80**, 2624-2636.

Kuo C. and Keto J. W. (1983), *J. Chem. Phys.* **78**, 1851-60.

Lichtenberg A. J., Vahedi V. and Liebermann M. A. (1994), *J. Appl. Phys.* **75**, 2339-2347.

Lichtenberg A. J., Kouznetsov I. G., Lee Y. T., Lieberman M. A., Kaganovich I. D. and Tsendin L. D. (1997), *Plasma Sources Sci. Technol.* **6**, 437–449.

Lieberman M. A. and Lichtenberg A. J. (1994), *Principles of plasma discharges and materials processing*, Wiley, New York.

Lister G. G. and Cox M. (1992), *Plasma Sources Sci. Technol.* **1**, 67-73.

Lister G. G., Li Y.-M. and Godyak V. A. (1996), *Appl. Phys.* **79**, 8993-8997.

Lowke J. J., Phelps A. V. and Irwin B. W. (1973), *J. Appl. Phys.* **44**, 4664-4671.

Niazi K., Lichtenberg A. J. and Lieberman M. A. (1995), *IEEE Trans. Plasma Sci.* **23**, 833-843.

Piejak R. B., Godyak V. A. and Alexandrovich B. M. (1992), *Plasma Sources Sci. Technol.* **1**, 179-186.

Pitaevskii L. P. (1962), *Soviet Physics-JETP* **15**, 919-921.

Singh H., Coburn J. and Graves D. B. (2001), *J. Vac. Sci. Technol. A* 19, 718-729.
Stamate E. and Ohe K. (1998), *J. Appl. Phys.* **84**, 2450-2458.

Stoffels E., Stoffels W. W., Vender D., Kando M., Kroesen G. M. W. and de Hoog F. J. (1995), *Phys. Rev. E* **51**, 2425-2435.

Tonnis E. J. and Graves D. B. (2002), *J. Vac. Sci. Technol. A* **20**, 1787-1795.

Vender D., Stoffels E., Stoffels W. W., Kroesen G. M. W. and de Hoog F. J. (1995), *Phys. Rev. E* **51**, 2436-2444.

von Engel A. (1965), *Ionized Gases 2nd ed.*, Claredon Press, Oxford.

Chapter 3 Electrical characteristics of the plasma sheaths in transformer-coupled toroidal discharges

3.1. Introduction

The use of transformer-coupled toroidal discharges (TCTDs) for applications such as the production of reactive gases (for example, atomic chlorine, fluorine and oxygen) has generated new technological challenges in several areas. One such technological challenge is related to the selection of the material for the chamber's walls. For semiconductor applications, dielectric chambers are not preferred due to the fragility of materials such as quartz and ceramics. Besides, the poor thermal properties of dielectric materials make them an inadequate choice for applications where high power densities are required. These problems have been addressed through the use of all-metal chambers with protective coatings. However, the use of all-metal chambers represents a drastic change in the plasma boundary conditions, with direct implications in the life of the chamber walls and wall coatings (González and Shabalin 2003; González et al. 2004a).

In this Chapter, we qualitatively describe the plasma interaction with different types of chambers. We also introduce a simple model that describes the voltage and current distribution across the sheath and along the plasma-wall boundary in all-metal

and dielectric TCTD chambers. Finally, we compare the results from the model with experimental data from an argon discharge in a metal chamber to show that the model provides an accurate representation of the underlying physics.

3.2. Problem statement

Plasmas join the chamber walls (and the electrodes in capacitive discharges) through a non-neutral boundary layer called the plasma sheath. The origin and properties of the plasma sheath have been discussed by several authors (Tonks and Langmuir 1929; Bohm 1949; Lam 1967; Franklin and Ockendon 1970; Sternberg and Godyak 2003; Riemann 2003; Franklin 2004). As electrons are more mobile than ions, the plasma-wall boundary is electron deficient, so positive ions produced in the plasma bulk are accelerated across the sheaths. The energy distribution of these ions is determined by several factors, such as the characteristics of the driving waveform, the gas pressure, etc. This energy distribution determines the amount of ion impact induced damage to the surface. In capacitive coupled plasmas (CCP), for example, the potential drop within the sheath can be as high as the total RF excitation voltage, reaching hundreds or even thousands of volts. This is also the case for some air-coupled inductive discharges with high capacitive coupling between the excitation coil and the grounded surfaces of the chamber. The high voltages developed on these plasmas have been successfully used for ion acceleration for materials processing in the semiconductor industry. However, energetic ions and high plasma sheath potentials are detrimental to the lifetime of the devices in applications such as lighting (Lister et al. 2004; Godyak 1994) or remote

plasma processing (González et al. 2004a). The lighting industry solved this problem by utilizing transformer-coupled toroidal discharges with glass chambers instead of CCPs: being electrodeless, and with a negligible capacitive coupling between the excitation coil and the plasma, these discharges develop sheath voltages of a few electron temperatures (e.g. $\phi_w = 4.7\ T_e$ for argon and $\phi_w = 2.8\ T_e$ for hydrogen). For such sheath voltages the ion bombardment energies are well below the sputtering and the ion enhanced etching thresholds (E_{th}) of the walls [e.g. $E_{th} = 50$ V for Al_2O_3 with Ar ions, Lee et. al. (1990)], hence minimizing contamination into the plasma and increasing the lifetime of the device (Godyak et al. 1994).

Although toroidal dielectric chambers are now commonplace in the lightning industry (Lister et al. 2004), they are not the preferred choice in high vacuum and/or high plasma power applications due to the fragility and poor thermal characteristics of materials such as quartz and ceramics. The introduction of all-metal chambers with protective coatings has helped to overcome these obstacles, greatly improving the design reliability of TCTDs. However, the use of all-metal chambers has deep implications in the interaction between the plasma and the walls that have not been yet thoroughly described in the literature. In the next Sections, we will discuss how metal chambers change the discharge boundary conditions, and how the presence of dielectric breaks in these vessels generates a discontinuity in the plasma wall boundary that radically changes the distribution of the sheath and plasma potential along the chamber.

3.3. Theory

In this Section, an analytical, self-consistent solution for collisional and collisionless RF sheaths in TCTDs that describes the temporal variation of voltages and currents across the sheath and along the chamber for both conductive and dielectric vessels is presented.

3.3.1. Model Hypotheses

Through the rest of this Chapter, some fundamental hypotheses will be assumed to hold within the range of plasma conditions of interest. This subsection presents these hypotheses and discusses their applicability and range of validity.

The model described later in this Chapter resembles that of Metze, Ernie and Oskam (1986), developed for parallel plate RF discharges operating at frequencies such that both electrons and ions respond instantly to time variations in the electric field of the sheath (i.e. $F << \omega_{pi}/2\pi < \omega_{pe}/2\pi$) (Pointu 1986). In this model, the physical properties of the plasma sheath are incorporated in an equivalent electrical circuit, where the sheath capacitances and the conduction currents through the sheath are time varying, and have a highly nonlinear dependence on the potentials across the plasma sheaths. The assumptions used to write and solve the model's equations are reviewed below:

1. The charged particles are only electrons and one type of positive ions. The presence of more than one type of positive ions will only slightly modify the model presented. In the case of discharges with electronegative gases, the negative ion density in high power TCTD is quite small in the plasma bulk and essentially zero at the edge of the plasma (Lichtenberg et. al. 1994), such that the edge region behaves essentially as electropositive (Lieberman and Lichtenberg 1994).

2. The electrons and ions have Maxwellian velocity distributions in the plasma bulk with temperatures T_e and T_i, respectively. The Maxwellian energy distribution applies to particles that experience only elastic collisions in the absence of electromagnetic fields. This is a good approximation for ions and other heavy particles in TCTD plasmas. However, for electrons the energy distribution function (EEDF) is determined by the balance or imbalance of the energy gains due to the local applied field and losses due to inelastic collisions. Electron-electron collisions play a compensating role in lengthening the tail of the EEDF. The effect of these collisions, when predominating over collisional processes, is to thermalize the EEDF, thereby yielding a Maxwellian distribution. For the case of argon, it is frequently assumed in the literature that for degrees of ionization above 10^{-4} the EEDF may be regarded as Maxwellian (Moisan et al. 1991). For degrees of ionization below 10^{-5}, the EEDF has generally a depleted high-energy tail. This kind of distribution can be approximated by the Druyvesteyn energy distribution function (figure 3.1), which predicts more electrons with average energy and fewer electrons at higher energies. This change in the shape of the

distribution function only affects the entrance speed of the ions to the sheath, which can be calculated from a generalized modified Bohm criterion (Riemann 1991).

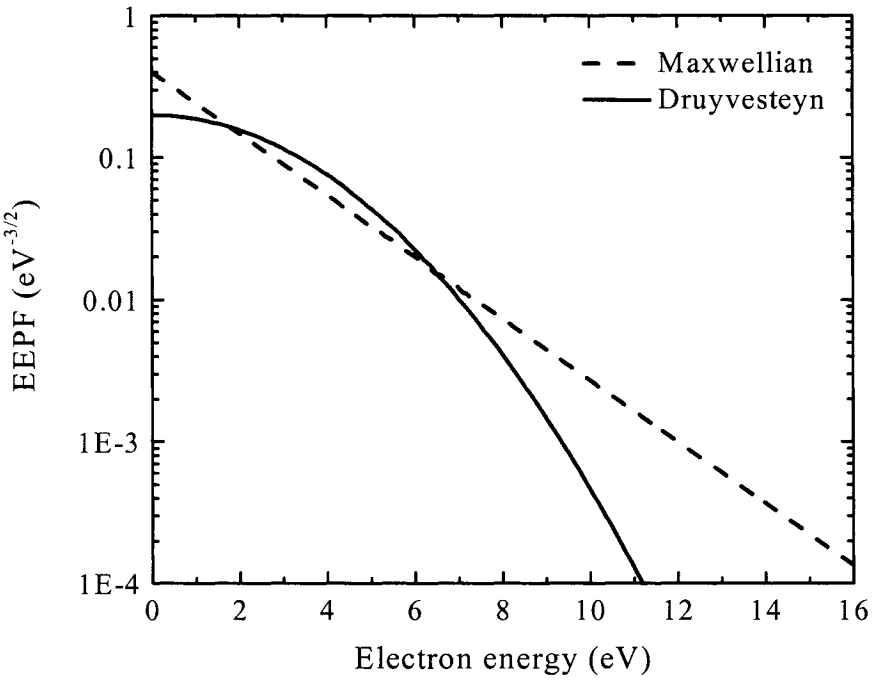

Figure 3.1. Electron energy probability function (EEPF) defined as $\varepsilon^{-1/2} f(\varepsilon)$ as a function of electron energy (ε) for $T_e = 2$ eV. If the velocity space is isotropic, a general equation for the EEDF can be expressed as $f(\varepsilon) = c_1 \sqrt{\varepsilon}\, \exp(-c_2\, \varepsilon^x)$ where ε is the electron energy, $c_1 = \dfrac{x}{\left(\frac{3}{2} T_e\right)^{3/2}} \dfrac{\Gamma\left(\frac{5}{2x}\right)^{3/2}}{\Gamma\left(\frac{3}{2x}\right)^{5/2}}$ and $c_2 = \dfrac{1}{\left(\frac{3}{2} T_e\right)^{x}} \dfrac{\Gamma\left(\frac{5}{2x}\right)^{x}}{\Gamma\left(\frac{3}{2x}\right)^{x}}$ (Amemiya H. 1997). Here $x = 1$ and $x = 2$ correspond to Maxwellian and Druyvesteyn electron energy distributions.

3. A modified Bohm sheath criterium can be applied to the plasma sheath boundary. The entrance speed of the ions into the plasma sheath is given by Godyak and Sternberg (1990) as

$$u_s = u_B \left(1 + \frac{\pi \lambda_{De1}}{2 \lambda_i} \right)^{-1/2} \tag{3.1}$$

where $u_B = (eT_e/M)^{1/2}$, M is the ion mass,

$$\lambda_{De1} = \left(\frac{\varepsilon_o T_e}{e n_s} \right)^{1/2}, \tag{3.2}$$

is the Debye length at the plasma-sheath interface,

$$\lambda_i = \frac{1}{\sigma_i n_g} \tag{3.3}$$

is the ion mean free path, n_g is the gas density and $\sigma_i \approx 10^{-4}$ cm^2 is the total ion-atom scattering cross for low energy argon ions (Lieberman and Lichtenberg 1994). This expression is assumed valid for the range of sheath conditions of interest. For the more general case, the entrance speed of the ions to the sheath can be calculated from the generalized Bohm criterium (Riemann 1991)

$$\frac{eT_e}{M}\int_0^{\infty}\frac{1}{u^2}f(u)\,du \le \left|T_e\frac{d(n_e+n_-)}{d\phi}\right|_{\phi=0} \tag{3.4}$$

where $f(u)$ is the one-dimensional speed distribution of the positive ions, $n_e + n_-$ is the sum of the densities of the negatively charged species, and ϕ is the potential, with $\phi = 0$ at the sheath/pre-sheath edge (figure 3.2). Equation (3.4) can be solved to include deviations from a Maxwellian distribution and the presence of negative ions.

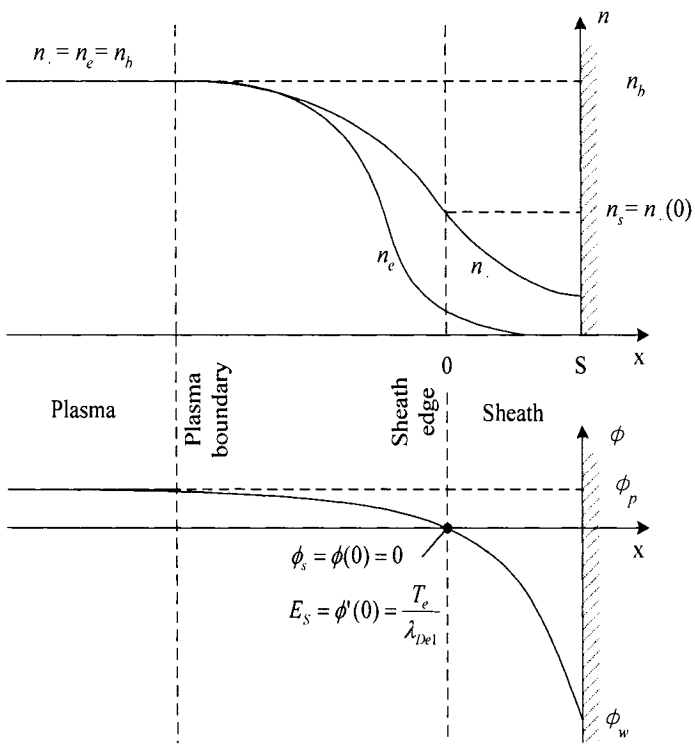

Figure 3.2. Qualitative behavior of the particle density and plasma potential at the wall, sheath and plasma boundaries (Sternberg and Godyak 2003).

4. The electrons have a Boltzmann density distribution in the pre-sheath and the plasma sheath. This assumption is satisfied if the plasma electrons are almost completely reflected by the sheath back into the plasma (Sternberg and Godyak 2003). Quantitatively, this condition is given by the inequality,

$$\exp\left(\frac{\phi_w}{T_e}\right) << 1 \tag{3.5}$$

where ϕ_w is the sheath potential at the wall and is always negative (figure 3.2). The electron density in the sheath can now be described by the Boltzmann equation

$$n_e(x) = n_s \exp\left(\frac{\phi(x)}{T_e}\right). \tag{3.6}$$

Here, n_s is the electron density at the boundary between the plasma and the sheath where the potential $\phi_s = \phi(x = 0) = 0$.

5. The electron temperature T_e is constant in time and the ion temperature T_i is equal to the neutral gas temperature T_g. These assumptions demand an excitation RF period shorter than the electron energy relaxation time $1/F < 4\tau_e$ and an electron energy relaxation frequency $(1/\tau_e)$ smaller than the ion-atom collisional frequency (ν_i) (see Table A.1). To analyze the range of validity for this assumption, let us consider the possible energy relaxation mechanisms. In the case of the weakly ionized plasmas that

are the subject of this study, the energy modulation due to mutual charged particle interactions can be neglected for the assumed charged particle number densities [i.e. the electron-ion collision frequency is much less than the electron-atom elastic collisional frequency $\upsilon_{e\text{-}i} << \upsilon_m$,Vahedi et. al. (1995)]. Inelastic interactions between electrons and atoms are also negligible, since they only involve a small fraction of the electrons in the high-energy tail of the electron energy distribution [i.e. $\upsilon_m^* << \upsilon_m$, where υ_m^* is the inelastic collisional frequency (Vahedi et al. 1995)]. Therefore, the dominant energy relaxation mechanism is elastic collisions with heavy particles. When such a process dominates, a large number of collisions (~$1/\delta$ collisions, where $\delta = (2m/M)$, m is the electron mass, and M is the atomic mass) are required for energy relaxation (Kolobov and Godyak 1995). Under these circumstances, the electron energy relaxation time τ_e can be expressed as:

$$\tau_e = (\delta \upsilon_m)^{-1} \tag{3.7}$$

Applying equation (3.7) to argon plasmas, the minimum RF excitation frequency for which this assumption stays valid is

$$F > \frac{1}{4\tau_e} = \frac{1}{4}\delta k_m n_g, \tag{3.8}$$

where k_m is the elastic electron-atom collisional rate for argon (figure b.1). From this expression, we see that the electron energy modulation at 10 mTorr and 10 Torr is small for excitation frequencies larger than 250 Hz and 15 kHz, respectively (Table A.1).

6. The electron and ion densities inside the plasma volume are constant in time. The validity of this assumption depends on the loss rate of the charged particles as well as the mechanism by which the plasma is maintained. This condition sets the minimum and maximum pressures for which the model is valid. Below the minimum pressure, the charged particle density is modulated by losses due to ambipolar diffusion, meaning that the characteristic ambipolar diffusion frequency $\langle \nu_{D_a} \rangle$ is greater than four times the RF excitation frequency F. Equivalently, above the maximum pressure the charged particle density is modulated by volume losses. The ambipolar diffusion characteristic frequency $\langle \nu_{D_a} \rangle$ is given by equation (2.95),

$$\langle \nu_{D_a} \rangle = \frac{D_a}{d_{eff} R_p^{\,2}} \tag{3.9}$$

where R_p is the radius of the plasma column and

$$D_a = \frac{k T_e}{M k_M n_g} \tag{3.10}$$

is the ambipolar diffusion coefficient, see equation (b.9). From these expressions, we can see that the charged particle density modulation due to ambipolar diffusion losses is small for pressures larger than 10 mTorr and frequencies greater than 75 kHz and 7 kHz for discharge radii of 0.8 cm and 3 cm, respectively (Table A.1).

7. The transit time τ_r of ions through the plasma sheath is not longer than $1/F$, where F is the frequency of the applied voltage. If this assumption is satisfied then the thickness of the plasma sheath at any given time t is equal to the DC sheath thickness corresponding to the instantaneous voltage $V_{sh}(t) = -\phi_w$ across the sheath.

The time for the ions to travel from the edge of the sheath to the wall can be estimated as (Kawamura et. al. 1999)

$$\tau_r = 3\left(-\frac{2e\phi_w}{M}\right)^{-\frac{1}{2}} s, \tag{3.11}$$

where s is the sheath thickness. For a totally collisionless plane sheath ($\lambda_i/\lambda_{De1} = 0$) the sheath thickness is expressed as

$$s = \lambda_{De1}\left\{\frac{1}{6}\left[2\left(2\frac{-\phi_w}{T_e}+1\right)^{1/2}-1\right]^{3/2}+\frac{1}{2}\left[2\left(2\frac{-\phi_w}{T_e}+1\right)^{1/2}-1\right]^{1/2}-\frac{2}{3}\right\}. \tag{3.12}$$

Note that for $-\phi_w/T_e >> 1$ equation (3.11) coincides with the Child-Langmuir law. For the collisional case ($\lambda_i/\lambda_{De1} \rightarrow \infty$) the sheath thickness is estimated as

$$s = \lambda_{De1}\frac{2}{3}\left[\left(\frac{5}{2}\frac{-\phi_w}{T_e}+1\right)^{3/5}-1\right] \tag{3.13}$$

where ϕ_w is the wall potential reference to the sheath edge (figure 3.3) (Godyak and Sternberg 1990). Figure 3.3 shows the relation between s/λ_{De1} and $-\phi_w/T_e$ for the extreme collisional and collisionless cases. Notice that the values of the sheath thickness are of the order of the plasma Debye length ($s \approx \lambda_{De1}$), and are not affected significantly by the plasma collisionality (λ_i/λ_{De1}) in the region where $-\phi_w/T_e < 10$.

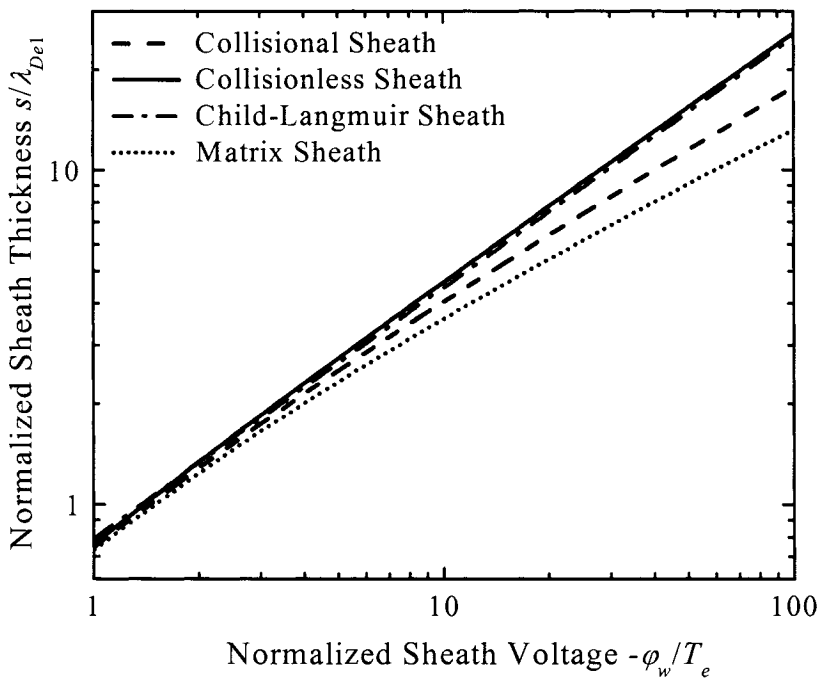

Figure 3.3. Normalized sheath thickness as a function of the normalized sheath voltage for a collisional (dashed line) and a collisionless (solid line) sheath (Godyak and Sternberg 1990). For reference, the corresponding curves for the ion matrix model (doted line) and the Child-Langmuir law (dash-doted line) are included (Lieberman and Lichtenberg 1994).

Utilizing equations (3.11), (3.12) and (3.13) we obtain an ion travel time of approximately 30 ns, for a plasma density at the sheath edge of 10^{11} cm^{-3} and a sheath voltage of 50 V. Therefore, this assumption appears to remain valid for frequencies up to approximately 8 MHz.

3.3.2. Case I: Chamber with dielectric walls

Let us start by analyzing the simple case of a TCTD with dielectric walls. Figure 3.4 shows a schematic cross-section of the toroidal discharge. The induced electromotive force V_{loop} around a closed loop is proportional to the rate of change of the concatenated magnetic flux $\Phi_{con}(t)$. For any closed path encircling the ferrite core we can write

$$V_{loop}(t) = \oint_{loop} \vec{E}(\vec{x},t)\cdot d\vec{l} = -\frac{1}{c}\int_{S}\frac{\partial \vec{B}(\vec{x},t)}{\partial t}\cdot \vec{n}\, da = -\frac{1}{c}\frac{d}{dt}\Phi_{con}(t). \qquad (3.14)$$

Integrating along the centerline of the plasma column (loop A) and utilizing that the electric field is constant along the integration path $\vec{E}(\vec{x},t) = E_p(t)\hat{\varphi}$, we can calculate the value of the electric field E_p at the centerline of the plasma as:

$$E_p(t) = \frac{\oint_{loop\ A} E_p(t)\cdot dl}{L_p} = \frac{V_{loop}(t)}{L_p}, \qquad (3.15)$$

where L_p is the plasma length. The electric field E_p is parallel to the walls and drives the toroidal plasma current.

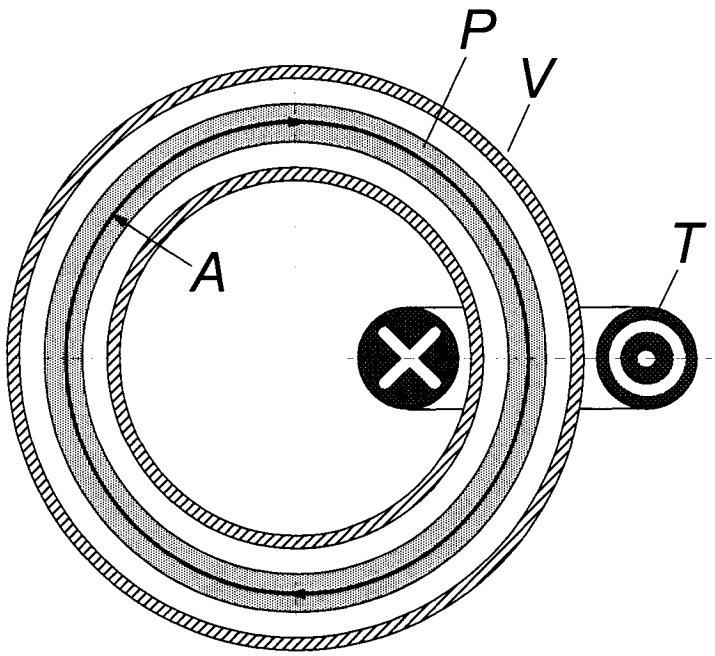

Figure 3.4. Cross sectional view of the toroidal chamber. Letters V, P and T indicate the vessel, plasma column and toroidal ferrite core, respectively, while A indicates the integration path used in the calculation. For simplicity, no other elements, such as the primary coil, are drawn.

In the direction of the small radius of the torus, the ambipolar electric field confines the electrons to the bulk region. Since we are considering a dielectric vessel, the wall charges are not free to move along the wall surface, implying zero net current to the wall at every point, $J_i - J_e\ (V_{sh}(t)) \equiv 0$. Therefore, the potential drop across the sheaths can be calculated by simply equating the ion flux

$$J_i = e n_s u_s = e n_s u_B \left(1 + \frac{\pi \lambda_{De1}}{2 \lambda_i}\right)^{-1/2} \tag{3.16}$$

to the electron flux at any point on the wall (Pointu 1986),

$$J_e(V_{sh}(t)) = \frac{1}{4} e n_s v_e \exp\left(-\frac{V_{sh}(t)}{T_e}\right), \tag{3.17}$$

where $V_{sh}(t)$ describes the instantaneous potential of any point of the wall with respect to the sheath edge as a function of time. In this expression, v_e is the mean electron velocity, which can be written as

$$v_e = \left(\frac{8eT_e}{\pi m}\right)^{1/2} \tag{3.18}$$

and n_s is the plasma density at the sheath boundary. This density can be estimated from the ion density n_0 at the center of the plasma, by equating equation (2.51) to the total current at the plasma sheath boundary such that

$$\Gamma_{R_p} = \frac{D_a n_0}{d_{eff} R_p} = n_s u_s . \tag{3.19}$$

Substituting (3.18) into (3.17) and equating (3.16) to (3.17) we obtain,

$$e n_s \left(1 + \frac{\pi \lambda_{De1}}{2\lambda_i}\right)^{-1/2} \left(\frac{eT_e}{M}\right)^{1/2} = \frac{1}{4} e n_s \left(\frac{8eT_e}{\pi m}\right)^{1/2} \exp\left(-\frac{V_{sh}(t)}{T_e}\right) \tag{3.20}$$

Solving for $V_{sh}(t)$, we obtain the potential drop across the sheath

$$V_{sh}(t) = \frac{T_e}{2}\left[\ln\left(\frac{M}{2\pi m}\right) - \ln\left(1 + \frac{\pi \lambda_{De1}}{2\lambda_i}\right)\right] \equiv -\phi_w \tag{3.21}$$

for $\lambda_{De1} / \lambda_i << 1$ we obtain the well know expression for the floating wall potential (Lieberman and Lichtenberg 1994)

$$V_{sh}(t) = \frac{T_e}{2} \ln\left(\frac{M}{2\pi m}\right) \equiv -\phi_w . \tag{3.22}$$

It is important to observe that the potential drop across the sheath is a function of both T_e and n_0 (through λ_{De1}). Therefore, it is constant in time (see hypothesis 5 and 6). The wall potential ϕ_w is negative and is linearly related to the electron temperature, with a factor proportional to the logarithm of the square root of the mass ratio. For hydrogen, for example, $\ln(M/2\pi m)^{1/2} \sim 2.8$, while for argon this factor is 4.7. Thus argon ions with initial energy $\varepsilon_s = T_e / 2$ at the sheath edge that fall through a collisionless sheath to a floating wall would bombard the wall with an energy of $\varepsilon_i = 4.7T_e + 0.5T_e = 5.2T_e$. For highly collisional sheaths, the bombarding energy will be some how smaller by an amount of $\frac{T_e}{2}\ln\left(1 + \frac{\pi \lambda_{De1}}{2\lambda_i}\right) \approx T_e$.

3.3.3. Case II: Chamber with metallic walls

Figure 3.5 shows a schematic cross section of a toroidal metallic chamber. The chamber is essentially the same as that presented in figure 3.4, except for the introduction of one dielectric break in the chamber, needed to interrupt closed current loops that otherwise would act as a shorted secondary for the excitation transformer.

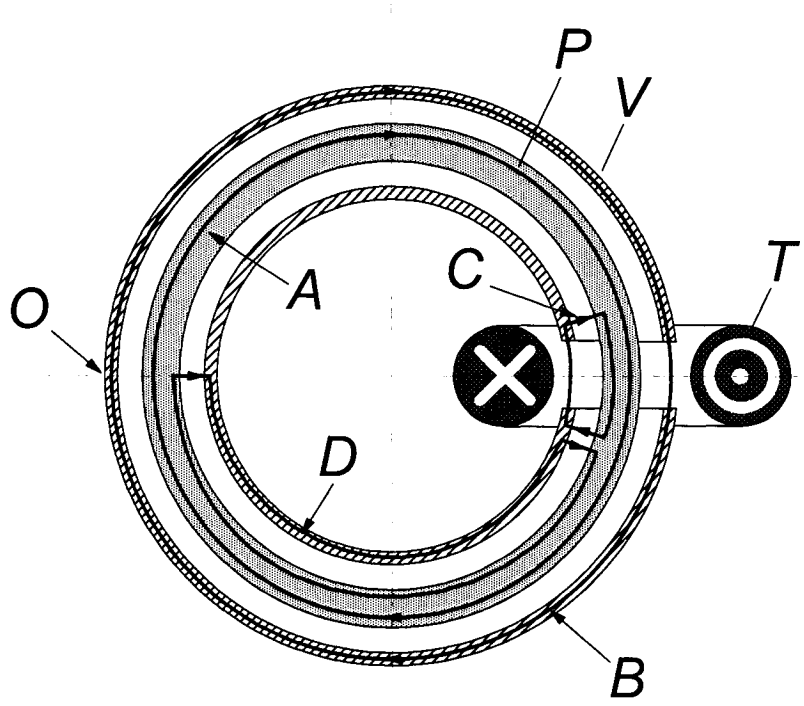

Figure 3.5. Cross sectional view of the toroidal chamber. Letters *V*, *P* and *T* indicate the vessel, plasma column and toroidal ferrite core, respectively. Letters *A* through *D* indicate different integration paths used in the calculations. The letter *O* indicates the origin of the dimensionless coordinate φ. For simplicity, no other elements, such as the primary coil, are drawn.

Replacing the dielectric chamber by a highly conductive metal chamber drastically changes the boundary conditions, as the vacuum chamber is now an equipotential surface. Let us start by calculating the sheath voltage around the chamber. The voltage across the chamber gap can be easily calculated integrating the electric field along the closed path *B* in figure 3.5:

$$\oint_{loopB} \vec{E}(\vec{x},t)\cdot d\vec{l} = V_{loop}(t) = E_c(t)L_c + E_g(t)L_g = E_g(t)L_g = V_g(t), \qquad (3.23)$$

where E_c is electric field within the chamber wall, E_g is electric field in the dielectric gap, L_c is length of the wall, L_g is length of the gap and V_g is the gap voltage. Here we have made use of the fact that E_c is zero for a metallic vessel. Both the change in the boundary conditions imposed by the metal chamber and the presence of a voltage drop across the gap V_g (equal to the single loop voltage V_{loop}) affects the value of the sheath voltage along the chamber. To calculate this voltage drop, let us start by integrating the electric field following a path that crosses the gap, both sheaths, and travels a short distance along the plasma column (loop *C*, which does not enclose any magnetic flux):

$$\oint_{loopC} \vec{E}(\vec{x},t)\cdot d\vec{l} = -E_g(t)L_g - \int_{sh1} \vec{E}_{sh1}(t)\,d\vec{l} + E_p(t)L_g + \int_{sh2} \vec{E}_{sh2}(t)\,d\vec{l} = 0, \qquad (3.24)$$

where E_{sh1}, E_{sh2} are the electric fields across the plasma sheaths immediately above and below the dielectric gap respectively. Substituting equations (3.15) and (3.23) into

equation (3.24), and assuming that L_g is small compared to the total plasma length L_p we obtain:

$$\int_{sh2} \vec{E}_{sh2}(t)\,d\vec{l} - \int_{sh1} \vec{E}_{sh1}(t)\,d\vec{l} = V_g(t) = V_{loop}(t) \qquad or$$
$$V_{sh2}(t) - V_{sh1}(t) = V_g(t) = V_{loop}(t), \tag{3.25}$$

where V_{sh2} and V_{sh1} are the voltage drops across the plasma sheaths immediately below and above the dielectric gap, respectively. Applying the same reasoning along loop *D*, we can write:

$$\oint_{loop\,D} \vec{E}(t)\cdot dl = -\int_{sh2} \vec{E}_2(t)\,d\vec{l} + E_p(t)\,\frac{L_p}{2} + \int_{sh3} \vec{E}_3(t)\,d\vec{l} - E_c(t)\,\frac{L_c}{2} = 0 \tag{3.26}$$

Using equations (3.15) and (3.23), and recalling that $E_c(t) \equiv 0$, we obtain

$$\int_{sh2} \vec{E}_{sh2}(t)\,d\vec{l} - \int_{sh3} \vec{E}_{sh3}(t)\,d\vec{l} = \frac{1}{2}V_g(t) = \frac{1}{2}V_{loop}(t) \quad \text{or}$$
$$V_{sh2}(t) - V_{sh3}(t) = \frac{1}{2}V_g(t) = \frac{1}{2}V_{loop}(t), \tag{3.27}$$

where E_{sh3} is the electric field across the plasma sheath for a point *O* diametrically opposed to the dielectric gap. Rearranging equation (3.25) and (3.27), we can write:

$$V_{sh2}(t) = \frac{1}{2} V_{loop}(t) + V_{sh3}(t) \quad \text{and} \quad V_{sh1}(t) = -\frac{1}{2} V_{loop}(t) + V_{sh3}(t) \tag{3.28}$$

These equations can be easily generalized to an arbitrary point located at a distance x from point O:

$$V_{shx}(t) = \frac{x}{L_p} V_{loop}(t) + V_1(t) \quad \text{or} \quad V_{sh}(\varphi, t) = \varphi\, V_{loop}(t) + V_1(t) \quad \text{with} \quad -\frac{1}{2} \le \varphi \le \frac{1}{2}, \tag{3.29}$$

where $\varphi = x/L_p$ is the dimensionless coordinate with respect to O expressed as a fraction of the plasma column length and $V_1(t) = V_{sh3}(t)$ (equation (3.29) reduces to equation (3.28) for φ = ½ and φ = -½). From equation (3.29) we observe that the voltage drop across the plasma sheath changes linearly along the chamber with its maximum always located at one side of the dielectric gap, in contrast with the case of dielectric vessels where the voltage drop across the plasma sheath is spatially independent (figure 3.5). Note that this qualitative difference arises only from the fact that we are now considering a metal chamber with a dielectric gap.

To complete the description of the plasma sheath for the case of metallic chambers, let us calculate the temporal dependence of the voltage and the temporal and spatial characteristics of the current density through the sheath. The expression for the total current density will depend upon the value of the excitation frequency. For sufficiently low excitation frequencies, the total current density J_{sh} can be approximated

by the conduction current density J_{cond}, given by the static plasma probe I-V characteristic (probe characteristic) (Pointu 1986),

$$J_{sh}(V_{sh}(\varphi,t)) \cong J_{cond}(V_{sh}(\varphi,t)) = J_i - J_e \exp\left(-\frac{V_{sh}(\varphi,t)}{T_e}\right), \tag{3.30}$$

where J_i and J_e are the saturated electron and ion current density, respectively. Their values are defined by equations (3.16) and (3.17); given the following expressions:

$$J_e = en_s\left(\frac{eT_e}{2\pi m}\right)^{\frac{1}{2}} \quad \text{and} \quad J_i = en_s\left(\frac{eT_e}{M}\right)^{\frac{1}{2}}\left(1+\frac{\pi\lambda_{De1}}{2\lambda_i}\right)^{-1/2}, \tag{3.31}$$

where n_s is defined in equation (3.19) as the density at the sheath edge (figure 3.2). At high frequencies the total sheath current needs to be modified to include also a displacement current density, which accounts for changes in the charge stored in the sheath (Metze et al. 1986; Sobolewski 1995):

$$J_{sh}(V_{sh}(\varphi,t)) = J_i - J_e \exp\left(-\frac{V_{sh}(\varphi,t)}{T_e}\right) + b\frac{\partial}{\partial t}\left(V_{sh}(\varphi,t)\right), \tag{3.32}$$

where the sheath capacitance per unit area, represented by b, is assumed to be constant.

To calculate the temporal dependence of the voltages, let us start by finding the potential drop along the plasma loop, which is given by

$$V_{loop}(t) = V_0 \sin(\omega t), \tag{3.33}$$

where V_0 is the amplitude of the transformer single turn voltage. Taking (3.29) and (3.33) into account, the most general expression for the potential drop across the plasma sheath at an arbitrary position φ can be written as:

$$V_{sh}(\varphi,t) = V_1(t) + \varphi\, V_0 \sin(\omega t) \tag{3.34}$$

where V_1 is an unknown function of time that represents the sheath voltage at position $\varphi = 0$. To find an expression for $V_1(t)$, we use the fact that the total current from the plasma to the chamber should be zero at all times:

$$I(t) = \int_{-1/2}^{1/2} J_{sh}(V_{sh}(\varphi,t))\, d\varphi \equiv 0 \quad ;\forall\, t \tag{3.35}$$

Assuming that the capacitance of the sheath can be neglected ($b = 0$ in equation 3.32), the solution for equations (3.34) and (3.35) can be expressed as follows:

$$J_i + J_e \exp\left(-\frac{V_1(t)}{T_e}\right) * \frac{T_e}{V_0 \sin(\omega t)} * \left(\exp\left(-\frac{V_0 \sin(\omega t)}{2T_e}\right) - \exp\left(+\frac{V_0 \sin(\omega t)}{2T_e}\right)\right) = 0. \tag{3.36}$$

Solving for the unknown function $V_1(t)$ yields:

$$V_1(t) = T_e \ln\left(\frac{J_e}{J_i} * \frac{\sinh\left(\frac{V_0 \sin(\omega t)}{2T_e}\right)}{\frac{V_0 \sin(\omega t)}{2T_e}}\right) = \phi_w + T_e \ln\left(\frac{\sinh\left(\frac{V_0 \sin(\omega t)}{2T_e}\right)}{\frac{V_0 \sin(\omega t)}{2T_e}}\right) \tag{3.37}$$

where ϕ_w is the undistorted floating potential, for which the total conduction current through the sheath is zero (3.21). From (3.34), and (3.37), we find the potential drop across the plasma sheath

$$V_{sh}(\varphi,t) = T_e \ln\left(\frac{J_e}{J_i} * \frac{\sinh(\nu(t))}{\nu(t)}\right) + 2\varphi T_e \nu(t) = -\phi_w + T_e \ln\left(\frac{\sinh(\nu(t))}{\nu(t)}\right) + 2\varphi T_e \nu(t) \tag{3.38}$$

where *v(t)* is a dimensionless voltage defined as

$$\nu(t) = \frac{V_0 \sin(\omega t)}{2T_e}. \tag{3.39}$$

The functional dependence of the sheath voltage (3.38) is illustrated in figure 3.6 as a function of relative position from the dielectric gap and time, relative to the RF gap voltage phase. The sheath voltage presents a DC offset that is given by the wall floating potential calculated in equation (3.21). Superimposed to it is the rectified sheath voltage $T_e \ln\left(\frac{\sinh(\nu(t))}{\nu(t)}\right)$ and the RF gap voltage scaled by the relative distance ($\varphi = x / L_p$) to the dielectric gap (see figure 3.7).

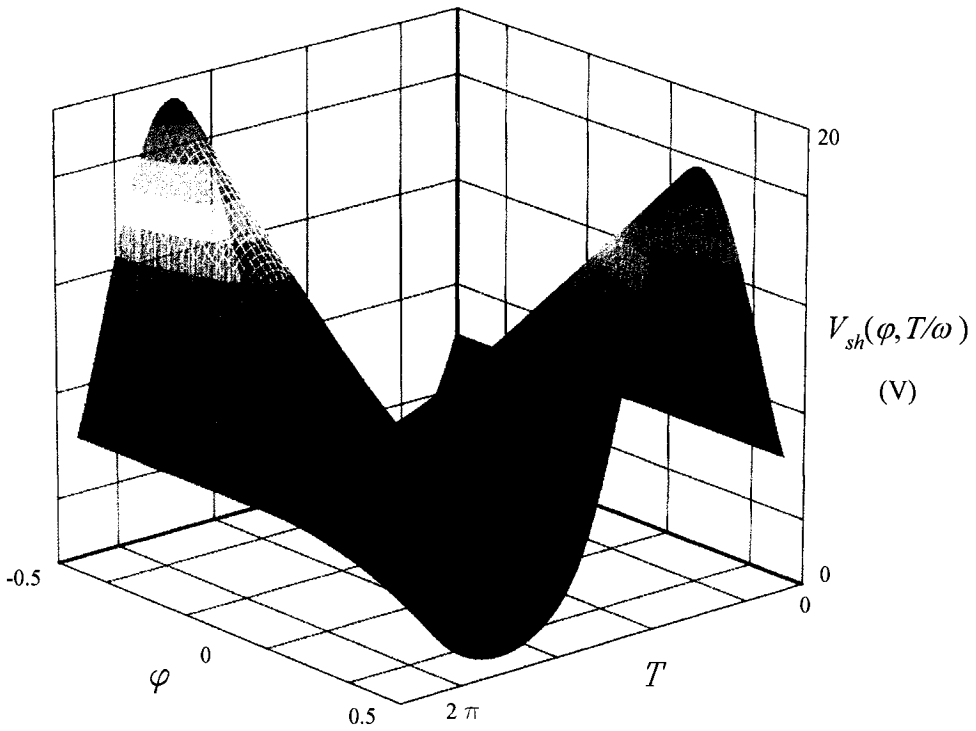

Figure 3.6. Sheath voltage $V_{sh}(\varphi, T/\omega)$ dependence on both dimensionless time (or RF phase $T = \omega t$) and the dimensionless chamber position ($\varphi = x / L_p$).

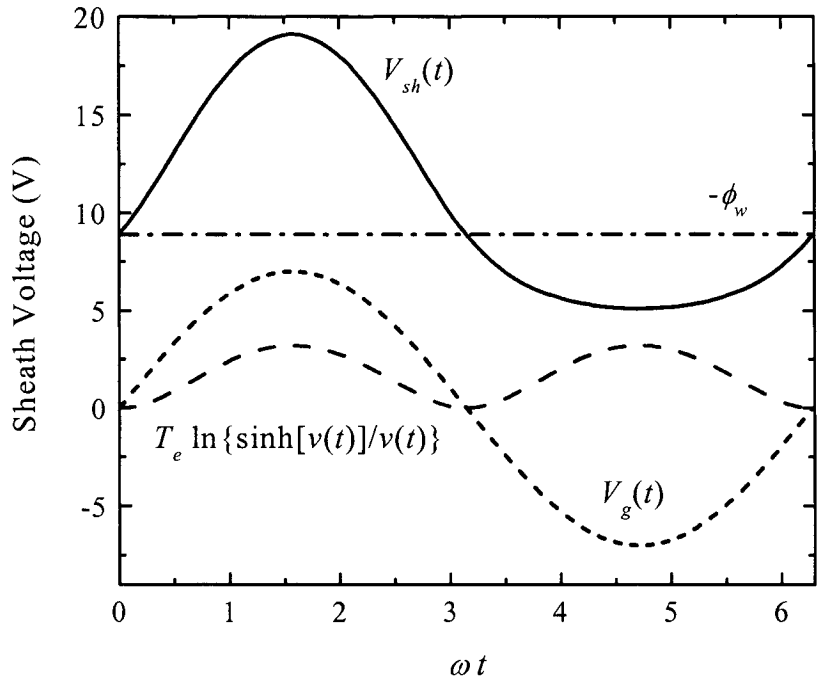

Figure 3.7. The total sheath voltage (red line) is composed of a DC offset (pink line) equal to the wall floating potential calculated in equation (3.21), the rectified sheath voltage $T_e \ln\left(\frac{\sinh(v(t))}{v(t)}\right)$ (green line), and the RF gap voltage scaled by the relative distance ($\varphi = x / L_p$) to the dielectric gap (blue line). All curves are plotted for a value of $\varphi = 0.5$, next to the dielectric gap were the peak voltage reaches its maximum and minimum values.

The sheath conduction current density at an arbitrary position φ, can be estimated from (3.30) and (3.38) as

$$J_{cond}(V_{sh}(\varphi,t)) = J_i\left(1 - \frac{v(t)}{\sinh(v(t))} * \exp(-2\varphi v(t))\right) \tag{3.40}$$

Equation (3.40) gives the particle current density at any point and time assuming that the displacement current through the sheath is negligible [b = 0 in equation (3.32)]. The shape of the current waveform predicted by (3.40) for conditions relevant to the experiments described in Section 3.4 is shown with a solid line in figure 3.8. The effect of a small sheath capacitance can be estimated by assuming that the corresponding displacement current is small and will not affect the voltage $V_1(t)$. From equation (3.21), we obtain the capacitive current density contribution as figure 3.9,

$$J_{cap}(V_{sh}(\varphi,t)) = b\,\frac{\partial}{\partial t}V_{sh}(\varphi,t) = b\,T_e\omega\,\cot(\omega t)\,\left[\left(\nu(t)\,\coth(\nu(t))-1\right)+2\varphi\,\nu(t)\right] \qquad (3.41)$$

which gives us the total current density through the sheath

$$J_{sh}(V_{sh}(\varphi,t)) = J_i\left(1-\frac{\nu(t)}{\sinh(\nu(t))}*\exp(-2\varphi\,\nu(t))\right) + b\,T_e\,\omega\,\cot(\omega t)\,\left[\left(\nu(t)\,\coth(\nu(t))-1\right)+2\varphi\,\nu(t)\right] \qquad (3.42)$$

Figure 3.8 shows a comparison between the conduction current density J_{cond} calculated using equation (3.40) and the total sheath current density (3.42), which includes the capacitive correction of equation (3.41) for a capacitance of b = 70 pF/cm^2. It can be noticed that the presence of a small capacitive coupling causes only a small asymmetry in the conduction current density waveform.

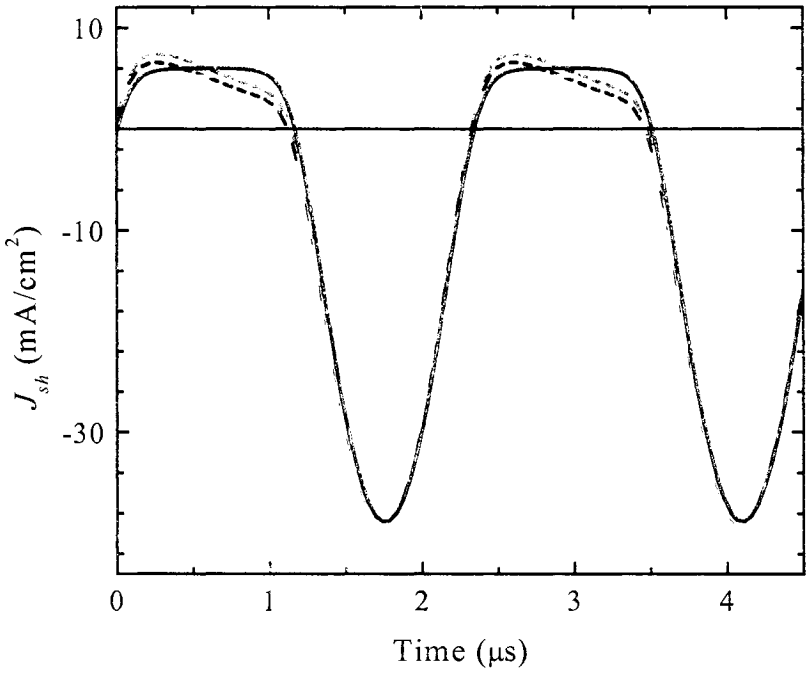

Figure 3.8. Calculated sheath current density J_{sh} at position $\varphi = 0.5$ for T_e = 1.9 V, $J_i = 6.1$ mA/cm^2, and $n_e = 3.0 \times 10^{11}$ cm^{-3}. The solid and dashed lines correspond to $b = 0$ F/cm^2 (negligible sheath capacitance) and $b = 70$ pF/cm^2, respectively.

As shown by equation (3.15), the new boundary conditions imposed by the voltage drop across the dielectric gap, cause the electron current from the plasma to concentrate on one side of the dielectric gap during the peak of RF voltage (3.42), alternating sides for every RF semi cycle. In contrast, the ion current to the wall is uniformly distributed along the chamber, but the ion energy is the highest at the opposite side of the gap where the electron current is concentrated (figure 3.9). This concentration of high-energy ions close to the dielectric gaps is the main source for wall erosion and particle generation in metal chambers.

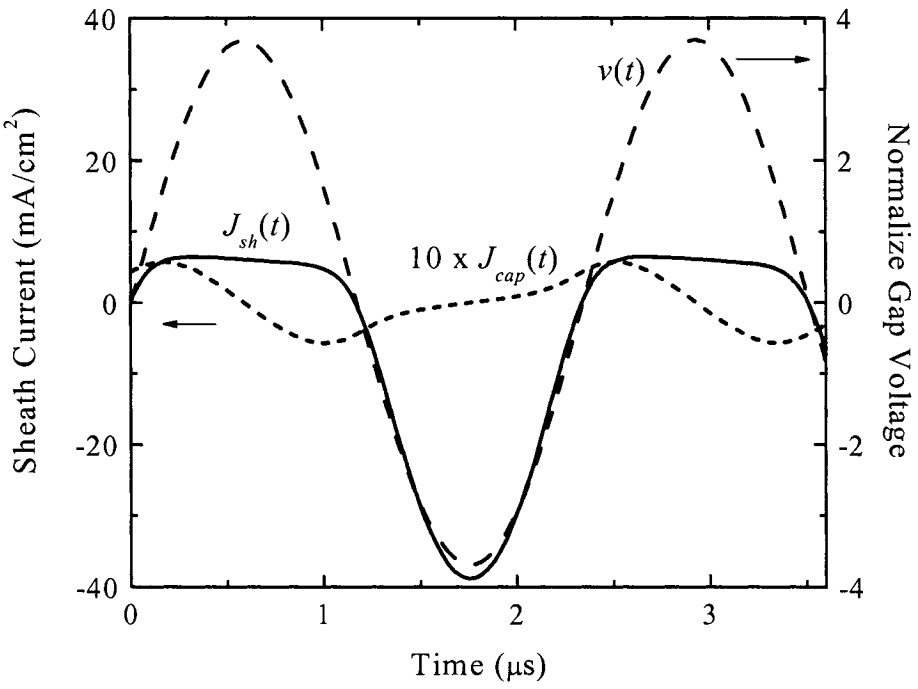

Figure 3.9. The calculated sheath displacement current density multiplied by 10 (10 × J_{cap}) in the blue dotted line, the total sheath current density (J_{sh}) in the solid red line and the normalize gap voltage (v) are shown as a function of time. The corresponding experimental conditions are the following: $\varphi = 0.5$, $T_e = 1.9$ V, $J_i = 6.1$ mA/cm^2, $n_e = 3.0$ x 10^{11} cm^{-3}, and $b = 70$ pF/cm^2.

3.4. Experimental

The simple model described in Section 3.3 allows for predicting the value of the sheath voltage and current as a function of time and position around the chamber. To assess the accuracy of the model predictions, measurements of the voltage in the gap(s) and the total current to the wall were performed for argon plasmas in a toroidal, all-metal chamber.

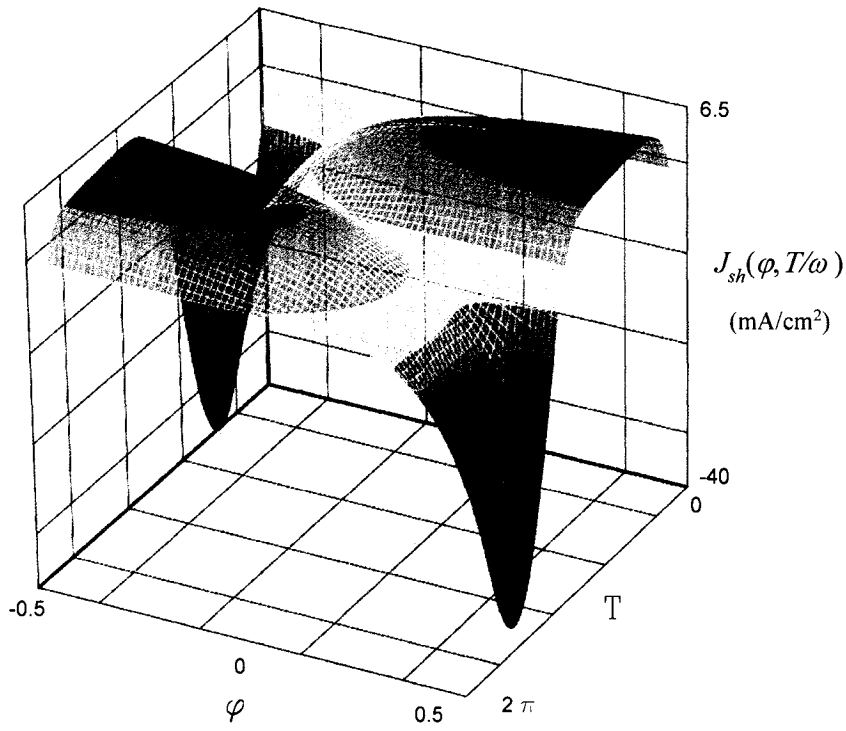

Figure 3.10. Sheath current density $J_{sh}(\varphi, T/\omega)$ dependence on dimensionless time (or RF phase ($T = \omega t$)) and dimensionless chamber position ($\varphi = x / L_p$).

3.4.1. Chamber

The experimental setup is shown in figure 3.11. A modified, non-anodized chamber from a commercial remote plasma source, Advanced Energy's Rapid-F RPS, was utilized for these measurements. The toroidal aluminum vacuum chamber has a cross section of 28 cm^2, a total volume of 1500 cm^3, and a total wall area of 1100 cm^2. The chamber consists of three subsections, S_1, S_2, and S_3. A ferrite-core transformer (4) concentric with one of the dielectric spacers provides the plasma excitation. Subsection S_3 is a small aluminum ring, one inch thick, installed between sections S_1 and S_2. All three subsections are separated from each other by means of three dielectric spacer

assemblies, *BC, FG* and *ED* (figure 3.11), whose function is to provide vacuum seal and electrical isolation between the chamber subsections.

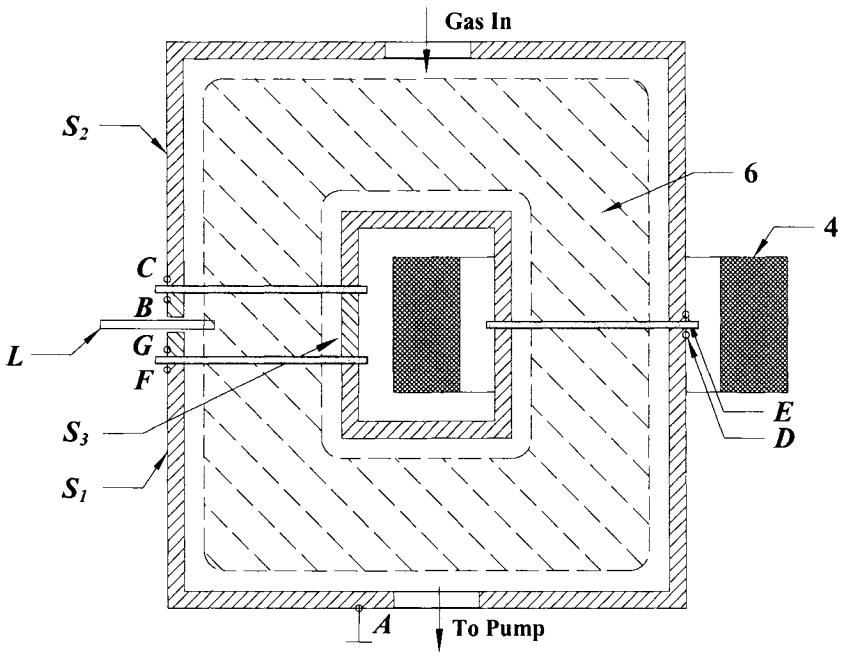

Figure 3.11. Schematic representation of the chamber used to measure the sheath properties in argon plasmas. The chamber consisted of three subsections, S_1, S_2 and S_3, isolated from each other by the dielectric gaps *BC, FG* and *ED*. The current probe, indicated by L, is installed in subsection S_3 (in close proximity to one of the dielectric gaps).

To maintain the vacuum integrity of the chamber, the dielectric assemblies must seal against the metal sections of the chamber forming a high vacuum seal. Figure 3.12 shows a schematic cross section of the dielectric break assembly. The vacuum seal is made of an elastic dielectric material, such as an o-ring (204). In addition, to extend the lifetime of the seal and minimize plasma contamination, an alumina ring protects (202) the vacuum seal from the reactive species present inside the plasma chamber.

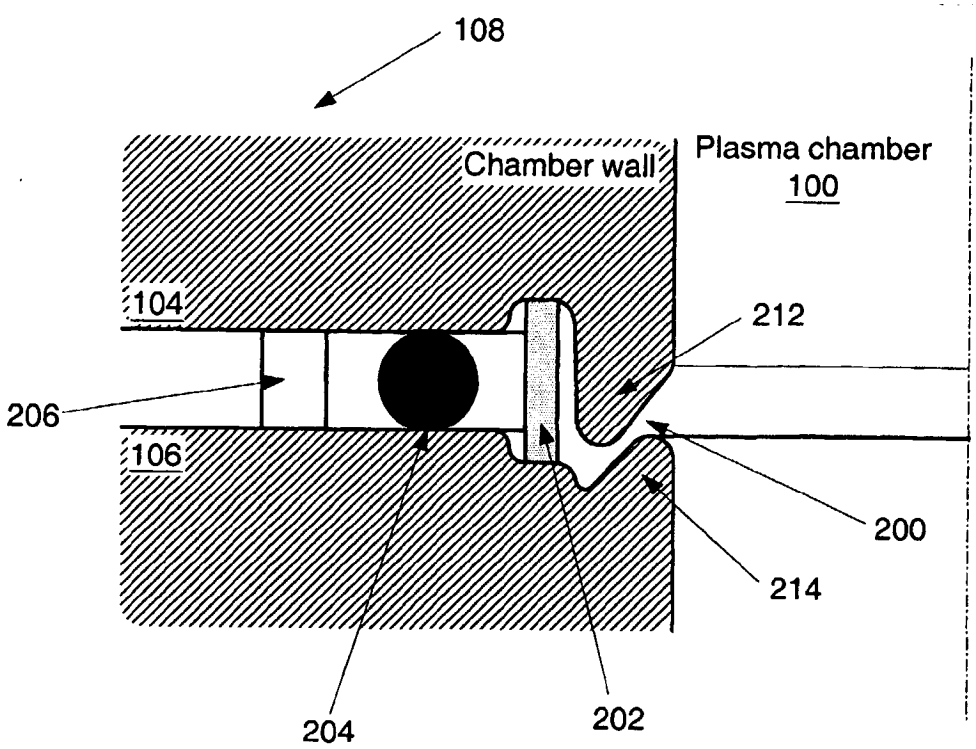

Figure 3.12. The dielectric break comprises a gap 200, an alumina protective shield 202, an o-ring vacuum seal 204, and a spacer 206, which are all located between the two housing portions 104 and 106 of the plasma chamber (González et al. 2004b).

Section S_1 is connected to the vacuum pumping system and is permanently connected to ground. The vacuum pumping system configuration is similar to that described in Chapter 2. The gas is fed through a plastic tube the top half portion of the chamber S_2, which can be grounded by shorting either the *ED* or the *BC* gap. Selecting the location of the shorted gap defines the relative position of the current probe *L* with respect to the gap, that is next to it or diametrically opposed. Figure 3.13 shows the equivalent schematic representations for both configurations. When either gap is shorted, the chamber behaves as a single-gap chamber. In the case when section S_2 is left floating,

the chamber behaves as a two-gap chamber. Gap *GF* is always kept shorted guaranteeing that section S_3 is always at ground potential. By inserting a low impedance current sensor between points *G* and *F*, the total plasma current to the walls of section S_3 can be measured.

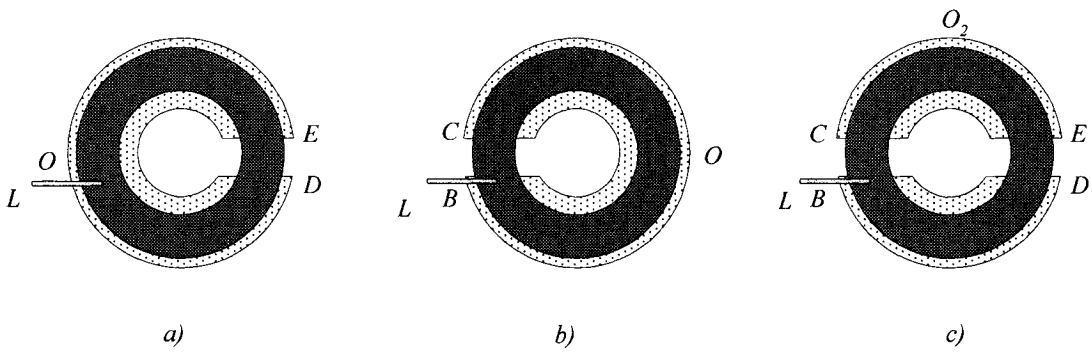

Figure 3.13. Schematic diagrams of the equivalent chamber configurations for different gap settings; a) gap *BC* shorted and *ED* open b) gap *ED* shorted and *BC* open and c) gap *ED* and *BC* open. Points O and O_2 are the origin for the coordinate variable φ.

3.4.2. Power Supply, Match and Transformer

The plasma excitation and the power delivery system are similar to those described in Chapter 2. The primary of the transformer is excited by a 50-Ω output impedance power supply (Advanced Energy PDX 2500) through a capacitive, L-type matching network operating at 427 KHz.

3.4.3. Electrical measurements

The RF voltage in the gap(s) was measured directly with a differential voltage probe (Tektronix P-5200). Special care was taken in routing the probe cables so not to create any loops around the ferrite and minimize the effect of stray magnetic fields.

The current to the walls was measured using an electrostatic probe installed close to the dielectric break *BC* in the grounded section of the chamber S_3 (figure 3.11). The probe was made out of a stainless steel rod 3.2 mm in diameter protruding 9 mm into the vacuum chamber. The probe diameter was much larger than the estimated plasma sheath thickness (~100 μm), and the current density to the probe and to the walls was assumed to be the same. As mentioned above, shorting one of the gaps allowed for the analysis of a chamber with only one dielectric break. Although the electrostatic probe was kept at the same physical position at all times, shorting *BC* or *ED* effectively located the probe at the relative positions $\varphi \approx 0$ or $\varphi \approx \frac{1}{2}$, respectively.

The current from the probe was measured using a fast transimpedance amplifier that kept the probe at ground potential. The circuit configuration of the transimpedance amplifier is shown in figure 3.14. Notice that the electrostatic probe is modeled here as two sections connected in series. The first section is formed by a current source in parallel with the sheath capacitance, while the second section is a parallel RC circuit that represents the equivalent impedance of the oxide film on the probe surface (a full justification of the probe model is given below). The amplifier's input impedance

generally limits the bandwidth of the frequency response. The gain-bandwidth product is usually a figure of merit to consider when evaluating the performance of a transimpedance amplifier. The feedback resistor R_f determines the transimpedance, and hence the sensitivity of the amplifier. Large values for R_f increase sensitivity, but reduce the amplifier's bandwidth since it contributes to the preamplifier's input load impedance. In general, the gain-bandwidth product of the amplifier and the minimum noise margin required at measuring point limit the circuit sensitivity. The diodes D_1 and D_2 operate as protection diodes. The amplifier U_1 is a wideband operational amplifier, with low input impedance and high output impedance.

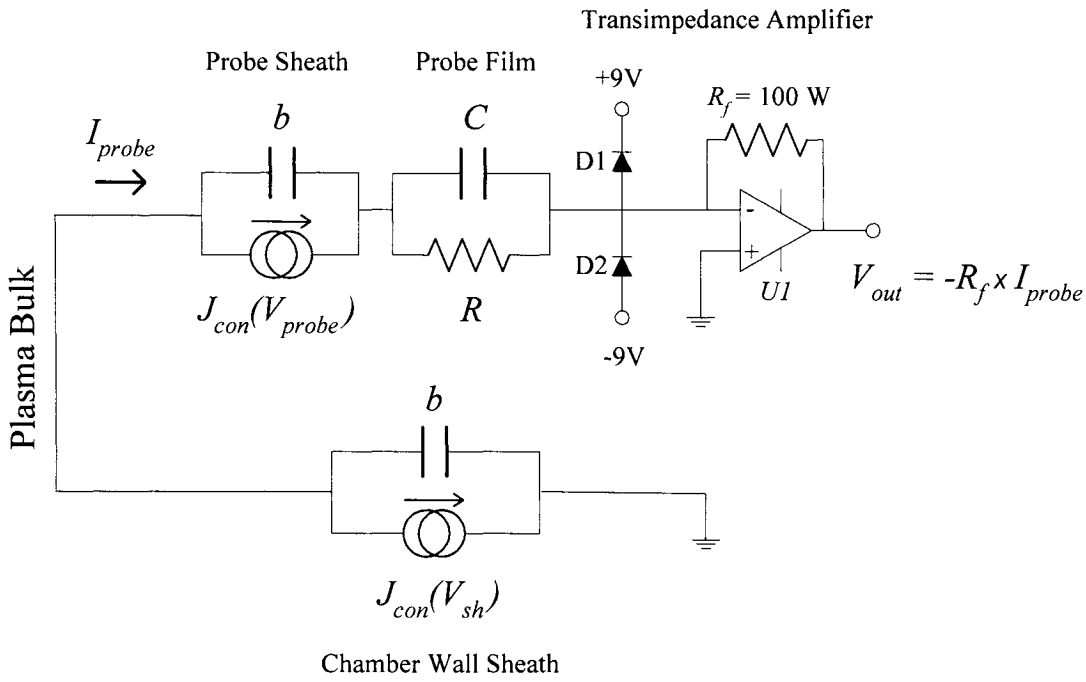

Figure 3.14. Current measuring schematic (transimpedance amplifier)

Both the signal from the differential probe and the output of the transimpedance amplifier were acquired simultaneously utilizing a four-channel Tektronix TDS3054B digitizing oscilloscope.

3.5. Results

Voltage and current measurements were performed for a plasma power of 350 W and an argon pressure of 300 mTorr. Three series of experiments were carried out. In the first series, the *ED* gap was shorted so that the probe was located next to the dielectric break ($\varphi \approx 0.5$). In the second series, *ED* gap was left open and the *BC* was shorted, making the probe lie diametrical opposed to the gap ($\varphi \approx 0$). In the last series, both gaps were left open dividing the loop voltage between the two active gaps. The probe current and gap voltage measured at $\varphi \approx 0.5$ as a function of time are shown in figure 3.15. The RF voltage amplitude at the dielectric gap was 14 V and the probe current was between -12 mA and 6 mA. Assuming that the current density to the probe and to the walls are similar, we can estimate the total ion (and electron) current to the walls to be about 6 A, when the peak plasma current (J_p) is 50 A, validating our assumption of a constant electric field along the plasma ($E_p(t) = J_p(t)/\sigma$), used in equation (2.1).

The measured probe current waveforms had almost no DC bias, which is in disagreement with the model predictions. Figure 3.15 shows the measured and predicted current waveforms for the probe, making evident the discrepancy between model and

measurements. Since our probe was made of stainless steel, this discrepancy can be explained by the existence of a native oxide film on the probe surface that partially blocked the DC component of the collected current. Usually, electrostatic probe measurements are very sensitive to contamination of the probe surface (Demidov 2002).

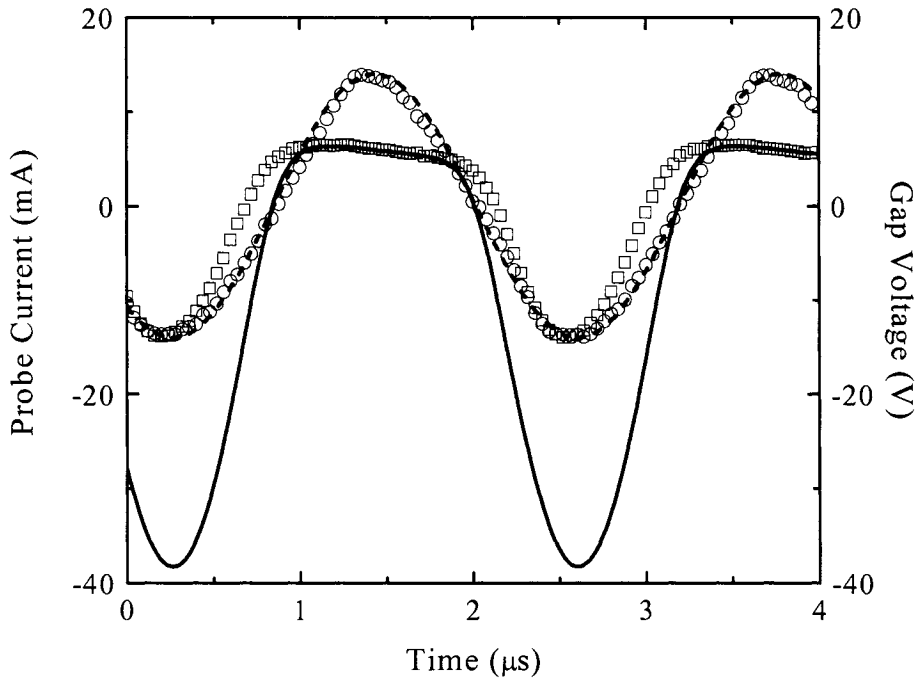

Figure 3.15. RF gap voltage and probe current for the probe close to the open gap *CB* (*ED* gap shorted, $\varphi = 0.5$), for a plasma power of 350 W and an argon gas pressure of 300 mTorr. Circles and squares indicate measured values of voltage and current, respectively. The dotted blue line indicates the sinusoidal excitation assumed for the model calculations. The solid red line is the calculated value of the current with no compensation for the oxide film on the probe, given by equation (3.35) for $T_e = 1.9$ V, $b = 23$ pF/cm^2, $J_i = 6.1$ mA/cm^2, and $n_e = 3.0\ 10^{11}$ cm^{-3}.

3.5.1. Probe model

The electrical characteristics of the oxide film can be simulated by a capacitor in parallel with a resistor (to accounts for the small DC component in the measured signal) (González and Shabalin 2003), figure 3.16 shows the equivalent circuit model utilized to represent the probe and plasma sheath interaction. Ignoring any perturbation of the plasma potential by the probe, the voltage at the probe has to be equal to the difference between the voltage across the plasma sheath, V_{sh}, and the voltage across the probe oxide film, V_{film}:

$$V_{probe}(\varphi,t) = V_{sh}(\varphi,t) - V_{film}(\varphi,t) \tag{3.43}$$

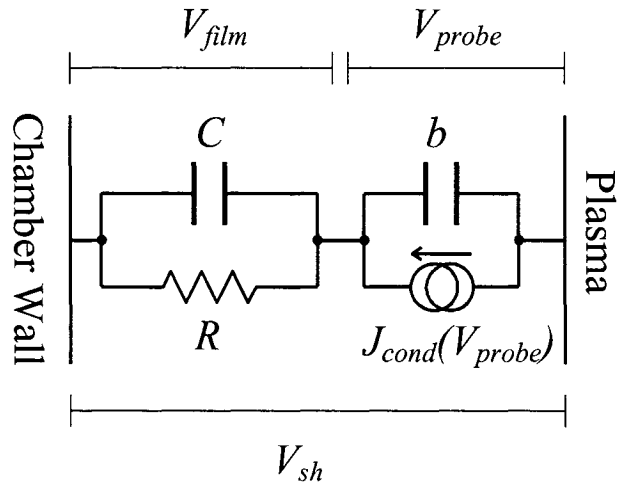

Figure 3.16. Equivalent circuit used to model the interaction between the probe and the plasma sheath. The symbols C and R represent the capacitance and resistance of the probe oxide film, respectively. The plasma sheath is described by the capacitance b and the voltage-controlled current source J_{cond}. V_{film}, V_{probe} and V_{sh} represent the voltage drop across the probe's oxide film, the probe's plasma sheath and the wall's plasma sheath, respectively.

At the same time, conservation of current results in the following expression:

$$C\frac{\partial V_{film}(\varphi,t)}{\partial t}+\frac{V_{film}(\varphi,t)}{R}=J_{cond}(V_{sh}(\varphi,t)-V_{film}(\varphi,t))+b\frac{\partial(V_{sh}(\varphi,t)-V_{film}(\varphi,t))}{\partial t}, \tag{3.44}$$

in addition, from equations (3.38) to (3.39) we obtain

$$J_{cond}(V_{sh}(\varphi,t)-V_{film}(\varphi,t))=J_i\left(1-\frac{\nu(t)}{\sinh(\nu(t))}\exp[-2\varphi\nu(t)]\exp\left[\frac{V_{film}(\varphi,t)}{T_e}\right]\right). \tag{3.45}$$

Using equation (3.45), and numerically solving the differential equation (3.44) for $V_{film}(\varphi, t)$ we obtain the probe current as a function of position and time:

$$J_{probe}(V_{film}(\varphi,t))=J_{sh}(V_{sh}(\varphi,t))-J_e\exp\left(\frac{V_{film}(\varphi,t)}{T_e}\right), \tag{3.46}$$

where $J_{sh}(\varphi,t)$ is the sheath current from equation (3.30). A fit to the experimental data results in $C > 23$ nF/cm^2 and $R \approx 2.2$ kΩcm^2 for the oxide film.

The addition of the current probe response to the sheath model results in an excellent agreement between experimental and predicted waveforms (see figure 3.17).

The calculation assumed $V_0 = 14$ V, $T_e = 1.9$ V, $\varphi = 0.5$ (position close to the open gap), $J_i = 6.1$ mA/cm^2, and $b = 23$ pF/cm^2.

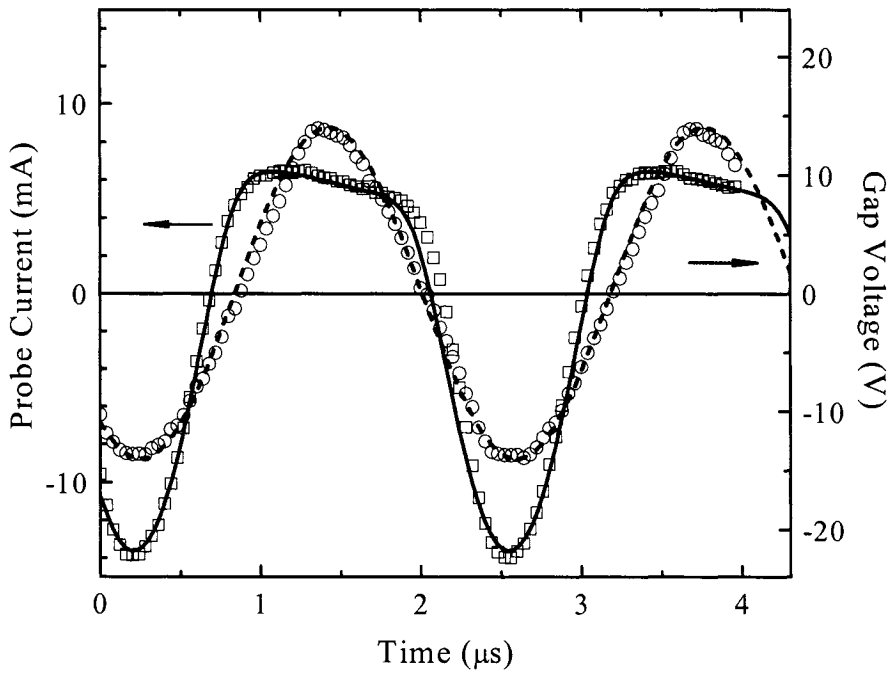

Figure 3.17. RF gap voltage and probe current for the probe close to the open gap *CB* (*ED* gap shorted, φ = 0.5), for a plasma power of 350 W and an argon gas pressure of 300 mTorr. Circles and squares indicate measured values of voltage and current, respectively. The dotted blue line indicates the sinusoidal excitation assumed for the model calculations. The solid red line is the calculated value of the current given by equation (3.46) for $T_e = 1.9$ V, $b = 23$ pF/cm^2, $J_i = 6.1$ mA/cm^2, and $n_e = 3.0\ 10^{11}$ cm^{-3}.

3.5.2. Data analysis

The results for the second series of experiments, where the gap BC was shorted ($\varphi \approx 0$), are show in figure 3.18. The measured and predicted waveforms were taken and calculated under the same experimental conditions and using the same values for the

probe parameters as in the first set of measurements ($\varphi \approx 0.5$, figure 3.17). The calculated waveforms once again closely follow the experimental data points.

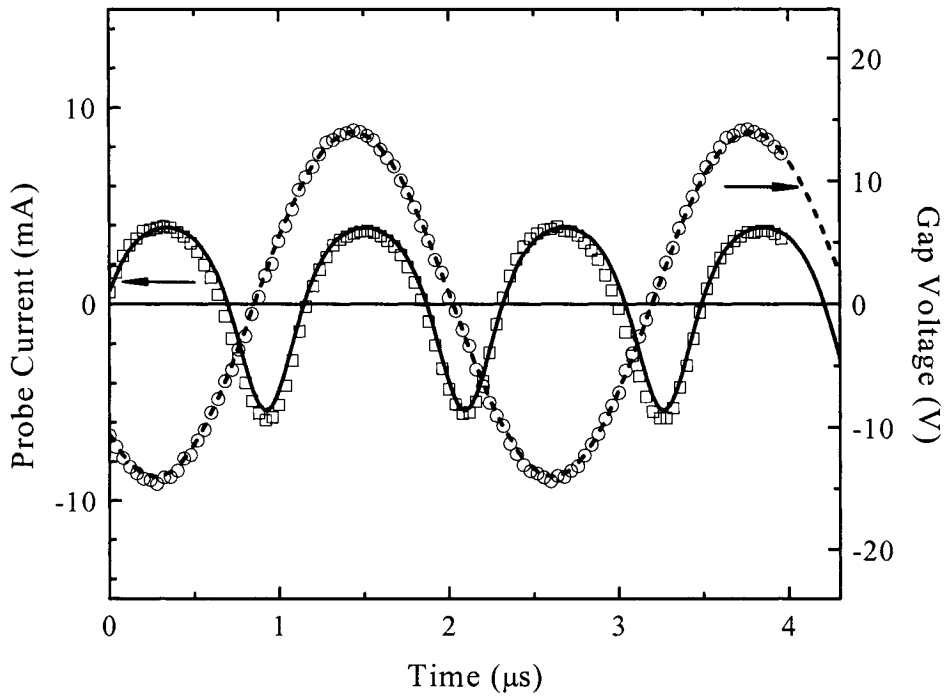

Figure 3.18. RF gap voltage and probe current for a position diametrically opposed to the open gap *ED* (*CB* gap shorted, $\varphi = 0$), for a plasma power of 350 W and an argon gas pressure of 300 mTorr. Circles and squares indicate measured values of voltage and current, respectively. The dotted blue line indicates the sinusoidal excitation assumed for the model calculations. The solid red line is the calculated value of the current given by equation (3.46) for the same parameters used in figure 3.17.

Finally, the measurements performed with both gaps open, and the same experimental condition that the two previous cases are shown in figure 3.19. In this configuration, the loop voltage is distributed between both gaps, so $V_{AB} \approx V_{CD} \approx V_{loop}/2$. The dimensionless coordinate of the probe is now $\varphi \approx 0.5$, with the new origin located at O_2 (figure 3.12), half the way between the gaps. The model prediction is again in very

good agreement with the experimental data. Note that the model parameters were kept at the same values as in figure 3.19 with exception of $V_0 = V_{loop}/2 = 7$ V, which matches the measured gap voltage (see figure 3.19).

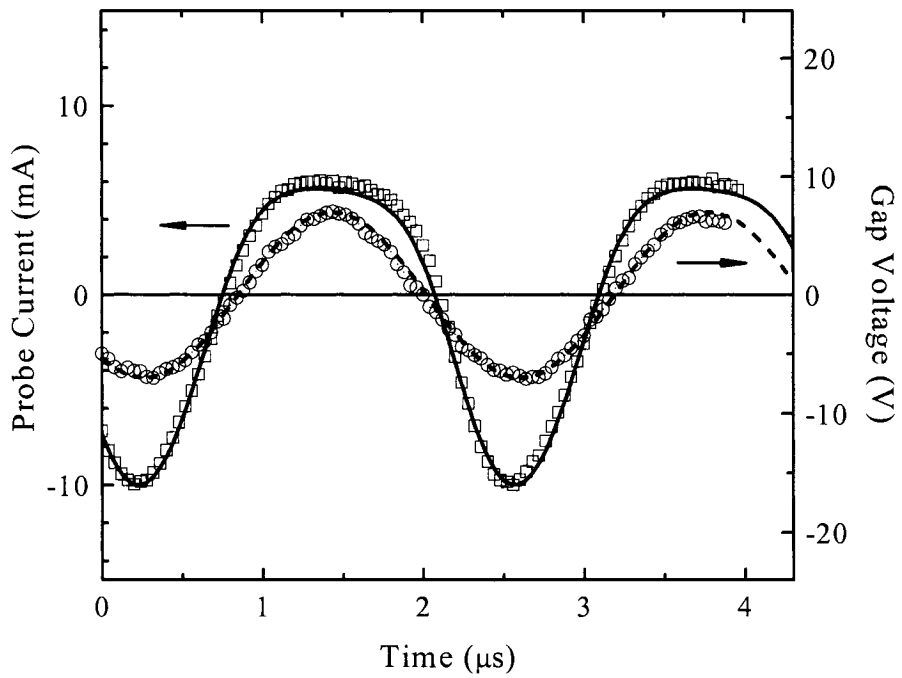

Figure 3.19. RF gap voltage and probe current for the probe close to an open gap (both gaps open, $\varphi = 0.5$), for a plasma power of 350 W and an argon gas pressure of 300 mTorr. Circles and squares indicate measured values of voltage and current, respectively. The dotted blue line indicates the sinusoidal excitation assumed for the model calculations. Note that in this case where both gaps are open the loop voltage is distributed between the gaps ($V_{CB} = 7$ V). The solid red line is the calculated value of the current given by equation (3.46) for the same parameters used in figure 3.17.

3.6. Summary

This Chapter presents a simple model that describes the temporal and spatial characteristics of the voltage and current in conductive toroidal chambers. The model predicts that the potential difference between plasma and chamber wall changes linearly with the position along the torus. As a result, during the peak of RF voltage the electron current from the plasma is concentrated on one side of the dielectric gap, right next to it. The ion current to the wall is uniformly distributed, but the ion energy is the highest next to the gap, on the opposite side to the electron current.

Comparison of the model prediction with actual results from experiments performed in argon shows that the model succeeds in capturing the essential aspects of the electrical interaction between the plasma and the walls. The results of the model can be used both as a guide in the design of transformer-coupled chambers, and as a laboratory tool for extracting information about the electron temperature and density of these plasmas.

3.7. References

Amemiya H. (1997), *J. Phys. Soc. Japan* **66,** 1335-1338.

Bohm D. (1949), "*The Characteristics of Electrical Discharges in Magnetic Fields*", ed. A. Guthrie and R. K. Wakerling, McGraw-Hill, New York.

Demidov V. I., Ratynskaia S. V. and Rypdal K. (2002), *Rev. Sci. Instrum.* **73**, 3409-3439.

Godyak V. A. and Sternberg N. (1990), *IEEE Transactions on Plasma Science* **18**, 159-168.

Franklin R. N. and Ockendon J. R. (1970), *J. Plasma Phys.* **4**, 371-385.

Franklin R. N. (2004), *J. Phys. D: Appl. Phys.* **37**, 1342-1345.

Godyak V. A., Piejak R. B. and Alexandrovich B. M. (1994), *Capacitively couple RF fluorescent lamp with RF magnetic enhancement*, United States Patent 5300860.

González J. J. and Shabalin A. (2003), *Plasma Sources Sci. Technol.* **12**, 317-323.

González J. J., Shabalin A. and Tomasel F. G. (2004a), *Mechanism for minimizing ion bombardment energy in a plasma chamber*, United States Patent 6724148.

González J. J., Dillon S., Shabalin A. and Tomasel F. G. (2004b), *Vacuum seal protection in a dielectric break*, United States Patent Application 20040149697.

Kawamura E., Vahedi V., Lieberman M. A. and Birdsall C. K. (1999), *Plasma Sources Sci. Technol.* **8,** R45–R64.

Kolobov V. I. and Godyak V. A. (1995), *IEEE Trans. Plasma Sci.* **23,** 503-531.

Lam S. H. (1967), *Proc. 8th Int. Conf. on Phenomena in Ionized Gases-Invited Lectures*, p 545, IAEA, Vienna.

Lee Y. H., Zhou Z. H., Danner D. A., Fryer P. M. and Harper J. M (1990), *J. Appl. Phys.* **68**, 5329-5336.

Lieberman M. A. and Lichtenberg A. J. (1994), "Principles of plasma discharges and materials processing", Wiley, New York.

Lichtenberg A. J., Vahedi M. A., Lieberman M. A. and Rognlien T. (1994), *J. Appl. Phys.* **75**, 2339-2347.

Lister G. G., Lawler J. E., Lapatovich W. P. and Godyak V. A. (2004), *Rev. Mod. Phys.* **76**, 541-598.

Metze A., Ernie D. H. and Oskam H. J. (1986), *J. Appl. Phys.* **60**, 3081-3087.

Moisan M., Barbeau C., Claude R., Ferreira C. M., Margot J., Paraszczak J., Sá A. B., Sauvé G. and Wertheimer M. R. (1991), *J. Vac. Sci. Technol. B* **9**, 8-25.

Pointu A. M. (1986), *J. Appl. Phys.* **60**, 4113-4118.

Riemann K-U. (1991), *Phys. Fluids B-Plasma* **3**, 3331-3338.

Riemann K-U. (2003), *J. Phys. D: Appl. Phys. 36*, 2811-2820.

Sobolewski M. A. (1995), *IEEE Trans. Plasma Sci.* **23**, 1006-1022.

Sternberg N. and Godyak V. (2003), *IEEE Trans. Plasma Sci.* **31**, 665-677.

Tonks L. and Langmuir I. (1929), *Phys. Rev.* **34**, 876-922.

Vahedi V., Lieberman M. A., DiPeso G., Rognlien T. D. and Hewett D. (1995), *J. Appl. Phys.* **78**, 1446-1458.

Chapter 4 Applications

4.1. Introduction.

Perfluorocompound (PFC) gases such as CF_4, C_2F_6, C_3F_8, C_4F_8 and others have been used extensively for in-situ chamber cleaning and etching processing for silicon nitride or silicon dioxide. Although these compounds are chemically and toxicologically benign, they strongly absorb in a portion of the infrared spectral region and have long lifetimes, often thousands of times that of CO_2. Several years ago, NF_3 was presented as a likely candidate to replace PFCs in stripping and reactor cleaning applications. Nitrogen trifluoride is environmentally preferable to PFCs because it has a much shorter atmospheric lifetime. Besides, NF_3 is easy to dissociate, and its discharges are not polymerizing. Due to these properties, this gas has since been utilized routinely in remote cleaning applications. However, due to cost, shortage of supply, and safety problems related to handling of NF_3, there has been a renewed interest in investigating PFCs, this time for remote plasma cleaning applications.

This Chapter presents results of the use of a TCTD as remote plasma source (Advanced Energy's Xstream AMN) for processing halocarbons in remote plasma cleaning applications.

4.2. Experimental setup.

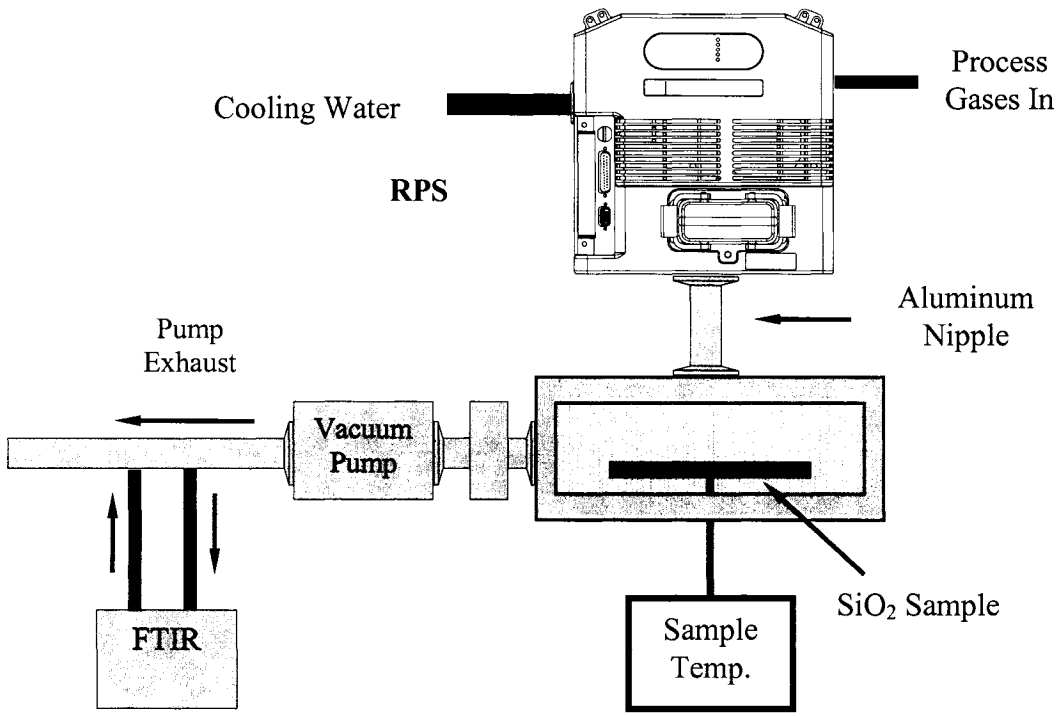

Figure 4.1. Experimental setup

Figure 4.1 shows a schematic representation of the vacuum system used for the experiments. The remote plasma source (RPS) was connected to a small aluminum vacuum chamber (dimensions) through a 12-cm-long aluminum nipple. A quartz disk 12.7 cm in diameter and 0.635 cm thick was placed in the vacuum chamber directly below the output of the remote plasma source. The temperature of the quartz disk was monitored on the backside of the disk with a thermocouple attached with a high thermal

conductivity epoxy. The thermal contact between the disk and the bottom wall of the chamber was enhanced by using silicon grease. The products from dissociation and reaction were pumped out from the chamber and diluted with N_2 in the mechanical pump. The exhaust of the pump was sampled and analyzed with a FTIR gas analyzer (Online Technologies 2010 Multi-gas analyzer). For gravimetric determinations, a digital scale with a resolution of 1 mg was used.

4.3. Results and discussion.

Typical recipes for fluorine production from halocarbons use oxygen as an additive. O xygen acts as a gatherer for carbon, avoiding polymerization in the chamber walls and substrate (Flamm 1989). For all the halocarbons studied, the main products at the exhaust present in the FTIR spectrum were observed to be CO_2, COF_2, CF_4, CO, SiF_4 and HF. Figure 4.2 shows the flows of the different byproducts as a function of time for a typical run. The recipe consisted of 300 sccm of C_3F_8 and 800 sccm of O_2 at 1.5 Torr, with a plasma power of 8 kW. Notice that while the flow of carbon bearing gases reaches steady state very rapidly, the flow of SiF_4 slowly increases with time, due to heating of the quartz disk being etched (see discussion below). When RF power is turned off, the flow of all byproducts decays to zero. Since the mass flow controller for C_3F_8 is turned off after the RF off signal, the flow of C_3F_8 exhibits a peak at the end of the run. To verify that the above-mentioned PFC gases are the only significant byproducts of the process, the atomic balance for different elements was also checked as a function of time.

Figure 4.3 shows an example of such calculations. Notice that the atomic balance for carbon adds up to 100% of the flow of the parent gas (C_3F_8), while the balance for fluorine and oxygen is significantly lower. However, the disagreement for these two elements is to be expected, as the FTIR is unable to detect the concentration of homonuclear diatomic molecules.

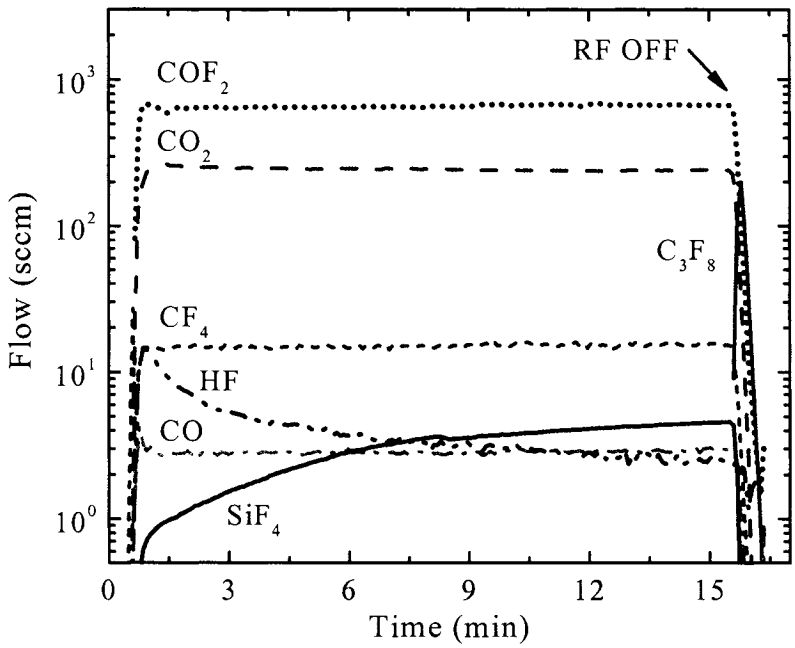

Figure 4.2. Measured flows for the different byproducts at the exit of the pumping line by the FTIR for 300 sccm of C_3F_8 and 800 sccm of O_2 at 1.5 Torr, with a plasma power of 8 kW.

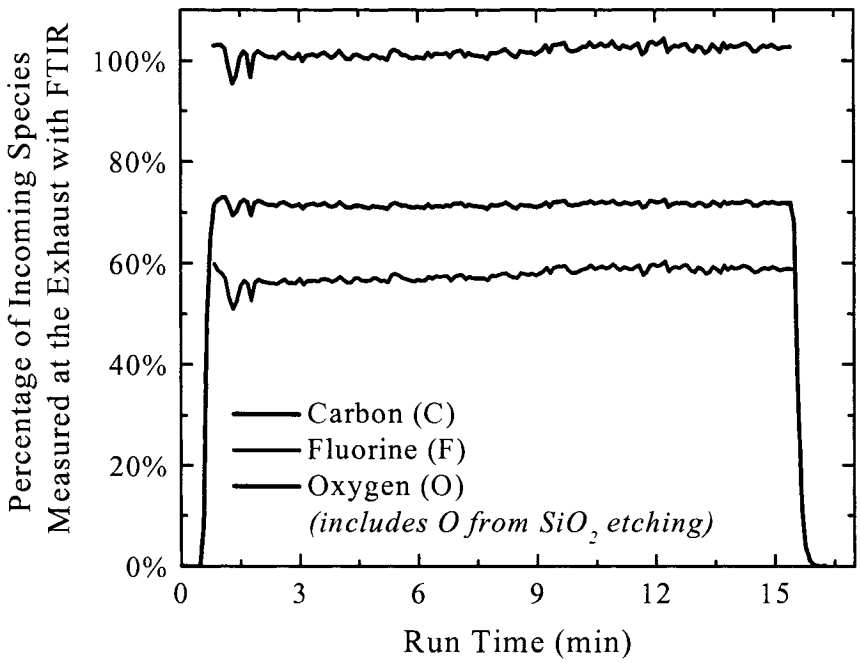

Figure 4.3. Atomic balance for carbon, oxygen and fluorine atoms.

The number of silicon atoms removed from the surface of the quartz disk was assumed to be equal to the number of SiF_4 molecules measured at the pump exhaust. In this way, the etch rate is proportional to the flow of SiF_4 gas at the exhaust. Comparing the integrated flow of SiF_4 to gravimetric measurements indicated that the assumption was correct within 10%. Temperature on the wafer changed as the hot gases leaving the RPS and the exothermic reactions occurring on the surface heated the quartz disk. Assuming that the main etching reaction is atomic fluorine etching SiO_2, the following expression (Flamm 1989) was fit to the data from several runs:

$$SiF_4 flow = C_1(p_F)T^{-1/2}e^{-C_2/T}, \quad (4.1)$$

where C_1 is a function of the partial pressure of fluorine p_F, T (K) is the surface temperature, and C_2 is proportional to the activation energy E_A of the process ($C_2 = E_A/R$). The assumption was corroborated by the results of several runs where the temperature of the substrate and SiF_4 flow were recorded as a function of time at constant flow and pressure of the feeding gas. Figure 4.4 show data from a typical run. For all cases studied C_2 fell within the 1700 ± 50 K range, value that is slightly lower than that reported for etching of SiO_2 by atomic fluorine (Flamm 1989). This may indicate that other processes with lower activation energy are competing on the surface of the sample.

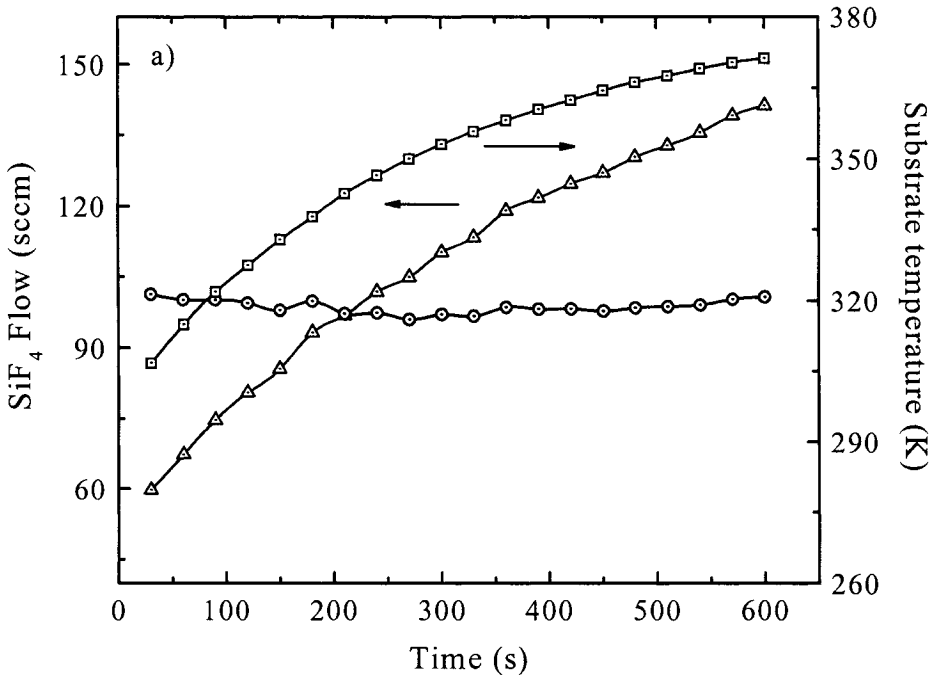

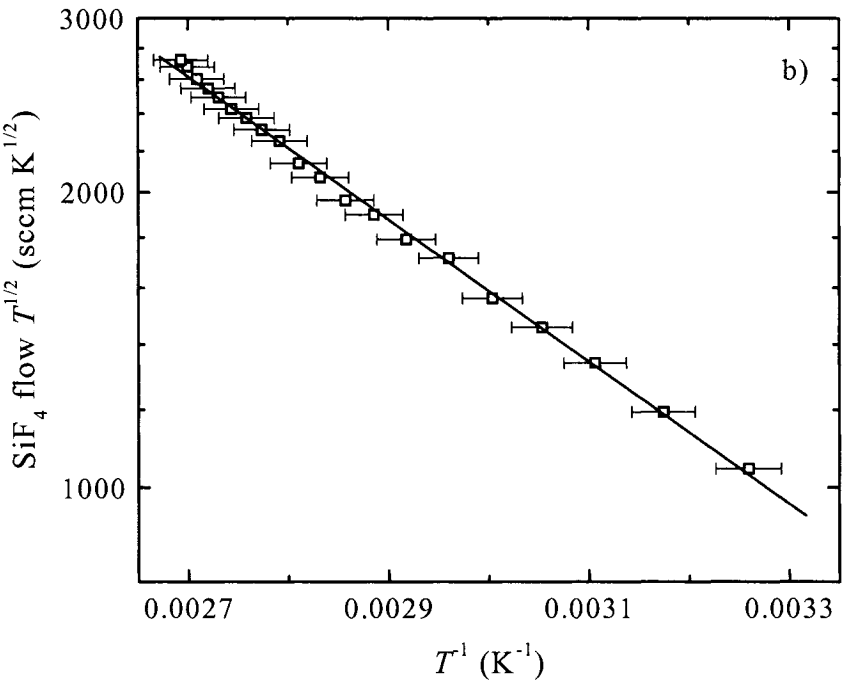

Figure 4.4. Data from SiO_2 etching using NF_3. a) As the etching process progresses, the temperature of the SiO_2 substrate (red squares) increases due to heating by the hot gases exiting the RPS and also from exothermic reactions occurring on the surface. As a result of this temperature increase, the SiF_4 flow (green triangles) proportional to the etch rate, also increases with time. The dependence of the SiF_4 flow with temperature can be described by equation (4.1), as evidenced by plot (b). The slope of the fitting straight line corresponds to $C_2 \approx 1700$ K. Using equation (4.1) to normalize the data to an arbitrary reference temperature of 70°C, results in the data points shown in blue in plot (a).

Figure 4.5 shows data for NF_3 etch of SiO_2. At low pressures, the etch rate is independent of the flow rate, indicating that the process is not limited by the availability of fluorine atoms. After a linear increase for low pressures, the etch rate starts to level off, reaching a maximum at a pressure value that depends on flow of the feeding gas. For SiO_2 etching, the initial step of the surface reaction, described by Eq. (4.1), is the slowest rate determining the overall reaction rate (Flamm 1989). In processes were the surface reaction is rate limiting, it can be easily shown that the relationship between reaction rate and pressure is linear for low pressures, but becomes constant as pressure is increased. Leveling off to a constant value for increasing pressure is expected in a system limited by surface reactions. The decrease in etch rate observed for higher pressures may be due to fluorine recombination into F_2. Molecular fluorine has been observed to be inefficient in etching thermal oxide (Flamm et al. 1979). This hypothesis is consistent with the increase in the concentration of F_2 with increasing pressures measured by Stueber et al. (2003). A similar drop in etch rate with increasing pressures has been observed in other atomic gases with high recombination rates; such as the case of etching parylene-N with atomic oxygen (Callahan et al. 2001).

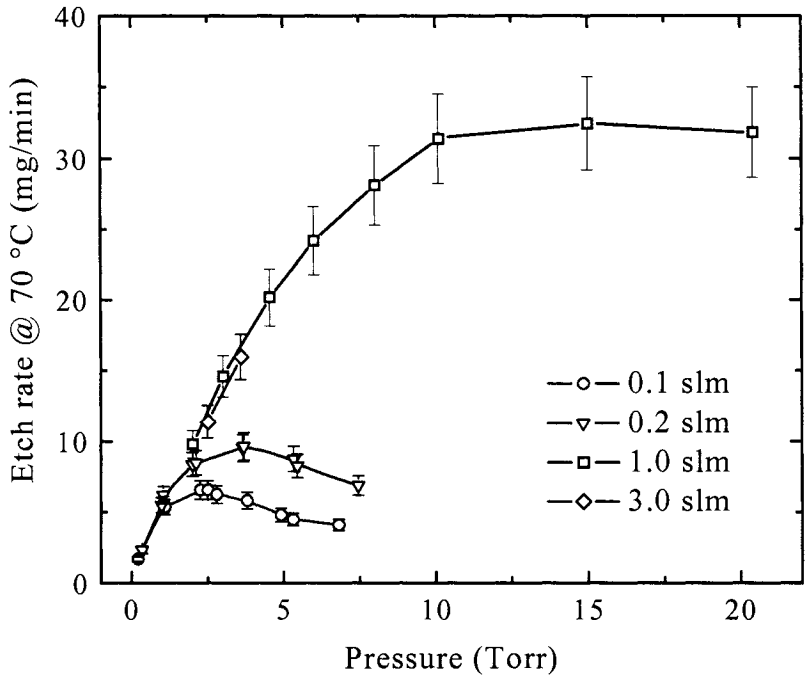

Figure 4.5. Etch rate of SiO_2 as a function of NF_3 pressure for different flows. Error bars represent both run-to-run variations and the uncertainty of the coefficient C_2 in Eq. (4.1). Multiplying the values on the vertical axes by 300 results in values of etch rate expressed Å/min. The power set point was 8 kW.

Figures 4.6 - 4.9 show the results of etching measurements for different halocarbons. Notice that the general behavior observed is similar to that of NF_3. The highest pressure points for all figures correspond to the maximum operating plasma voltage (i.e. single loop voltage) allowed by the RPS. The highest flow plotted for each gas is close to the maximum that the unit can handle. Flows slightly higher than the maximum reported in these figures can be achieved for a very narrow range of pressures. The lowest pressure at which data points could be acquired was limited by the pumping speed of the system.

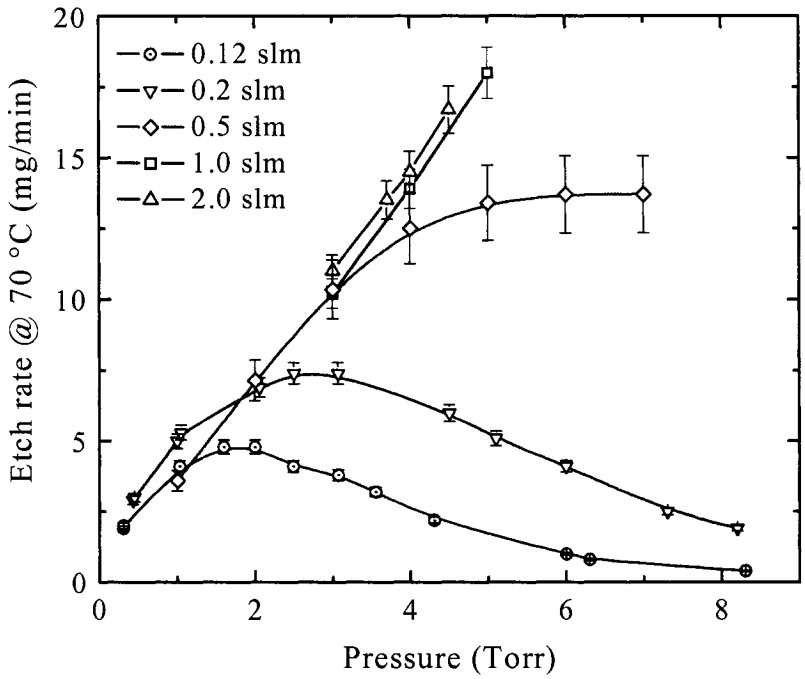

Figure 4.6. Etch rate of SiO_2 as a function of total pressure of CF_4/O_2 mixtures for different feeding gas flows. The flow ratio CF_4:O_2 was kept at 1:1. The CF_4 flow for the different runs is indicated in the figure. The power set point was 8 kW.

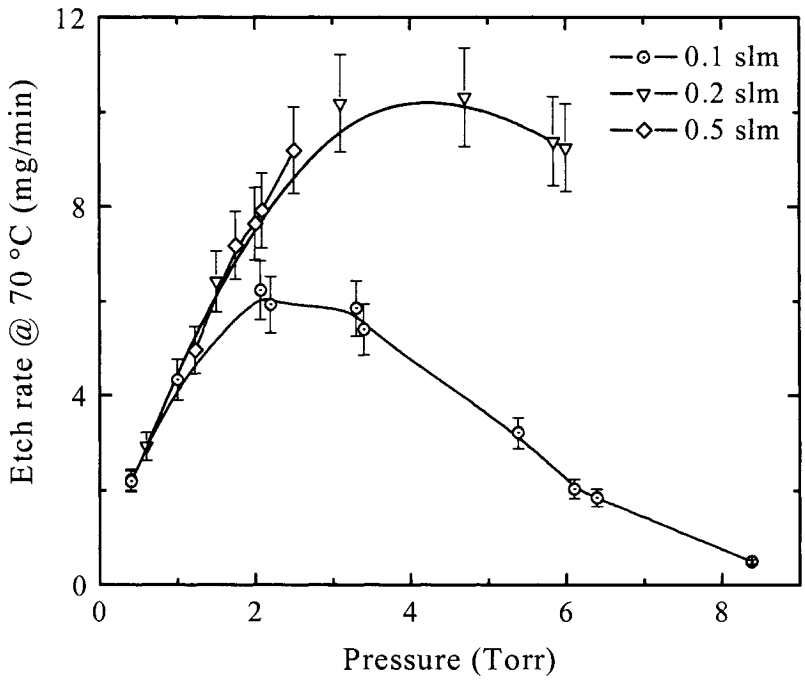

Figure 4.7. Etch rate of SiO_2 as a function of total pressure of C_2F_6/O_2 mixtures for different feeding gas flows. The flow ratio C_2F_6:O_2 was kept at 1:2. The C_2F_6 flow for the different runs is indicated in the figure. The power set point was 8 kW.

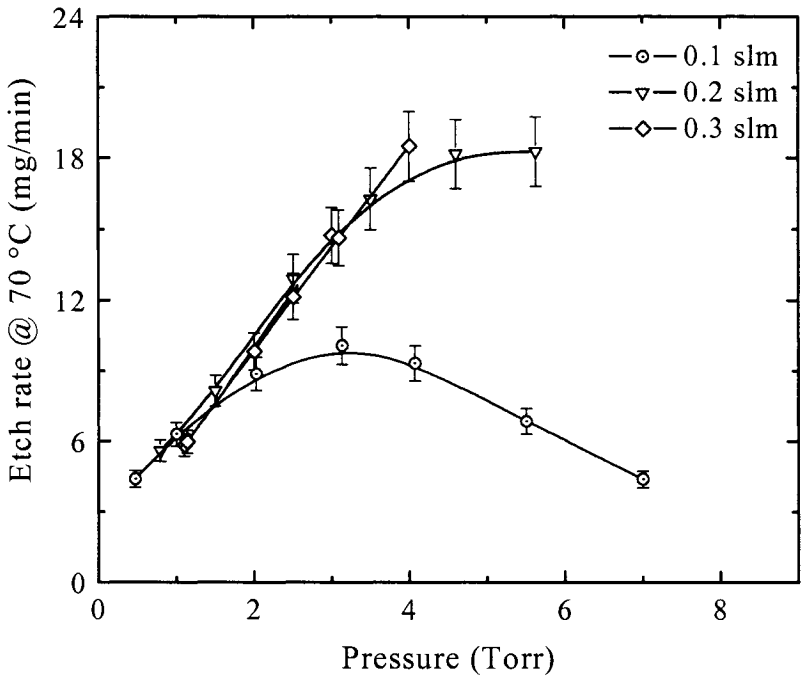

Figure 4.8. Etch rate of SiO_2 as a function of total pressure of C_3F_8/O_2 mixtures for different feeding gas flows. The flow ratio C_3F_8:O_2 was kept at 1:3. The C_3F_8 flow for the different runs is indicated in the figure. The power set point was 8 kW.

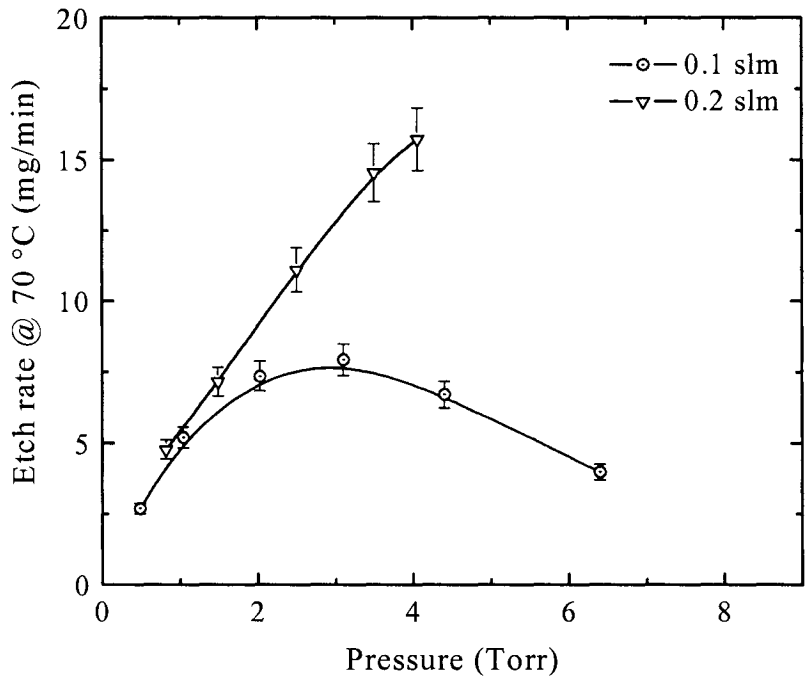

Figure 4.9. Etch rate of SiO_2 as a function of total pressure of C_4F_8O/O_2 mixtures for different feeding gas flows. The flow ratio $C_4F_8O:O_2$ was kept at 1:3. The C_4F_8O flow for the different runs is indicated in the figure. The power set point was 8 kW.

Choosing a certain pressure and flow of NF_3 as a reference makes it is easier to compare the performance of halocarbons against NF_3. Let us select 1 slm, 3 Torr as a typical condition to run NF_3 clean. From figure 4.5, the etch rate at those conditions is approximately 15 mg/min or 4,500 Å/min at 70°C. As shown in figures 4.6 and 4.8, similar etch rates are achieved flowing 1-2 slm of CF_4 with O_2 (1:1) at about 4 Torr, or 0.2-0.3 slm of C_3F_8 with O_2 (1:3) at about 3.3 Torr. For C_2F_6/O_2 (1:2) and C_4F_8O/O_2 (1:3) mixtures those rates are not possible to achieve within the RPS operating range (see figures. 4.7 - 4.9). Adding argon to the feeding gas can extend the operating range of the

RPS. Argon reduces the impedance of the plasma discharge, allowing for operation at higher pressures and flows. Figures 4.10 - 4.12 show the effect of adding different amounts of argon to halocarbon/oxygen mixtures.

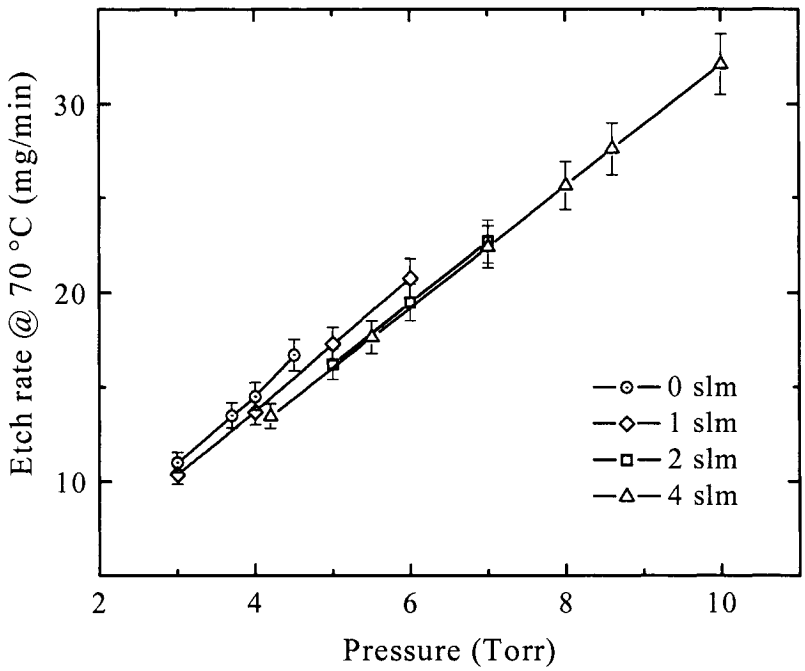

Figure 4.10. Etch rate of SiO_2 as a function of total pressure of $CF_4/O_2/Ar$ mixtures for different flows of argon dilution. The flow ratio CF_4:O_2 was kept constant at 2 slm of CF_4 and 2 slm of O_2. The Ar flow dilution for the different runs is indicated in the figure. The power set point was 8 kW.

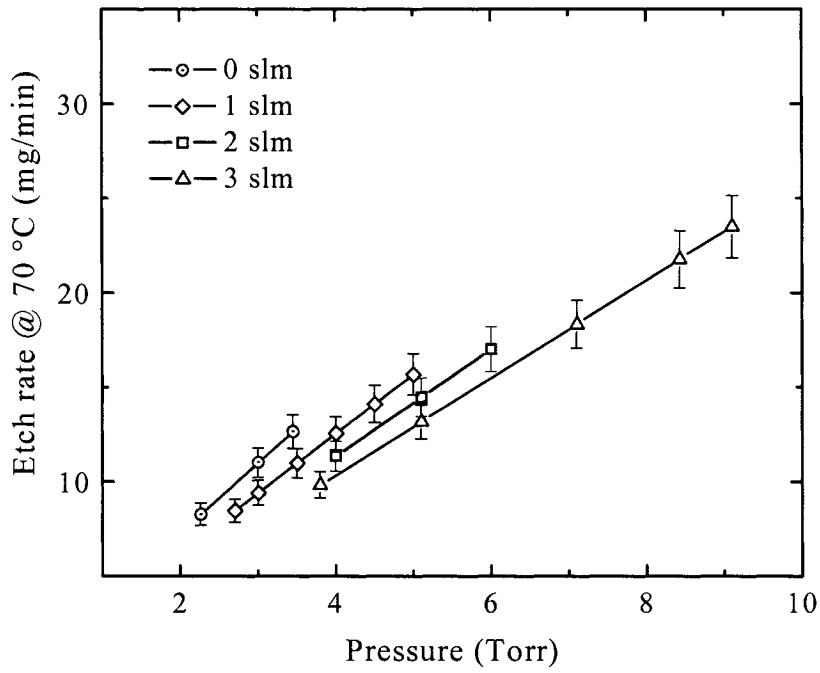

Figure 4.11. Etch rate of SiO_2 as a function of total pressure of $C_2F_6/O_2/Ar$ mixtures for different flows of argon dilution. The flow ratio C_2F_6:O_2 was kept constant at 1 slm of C_2F_6 and 2 slm of O_2. The Ar flow dilution for the different runs is indicated in the figure. The power set point was 8 kW.

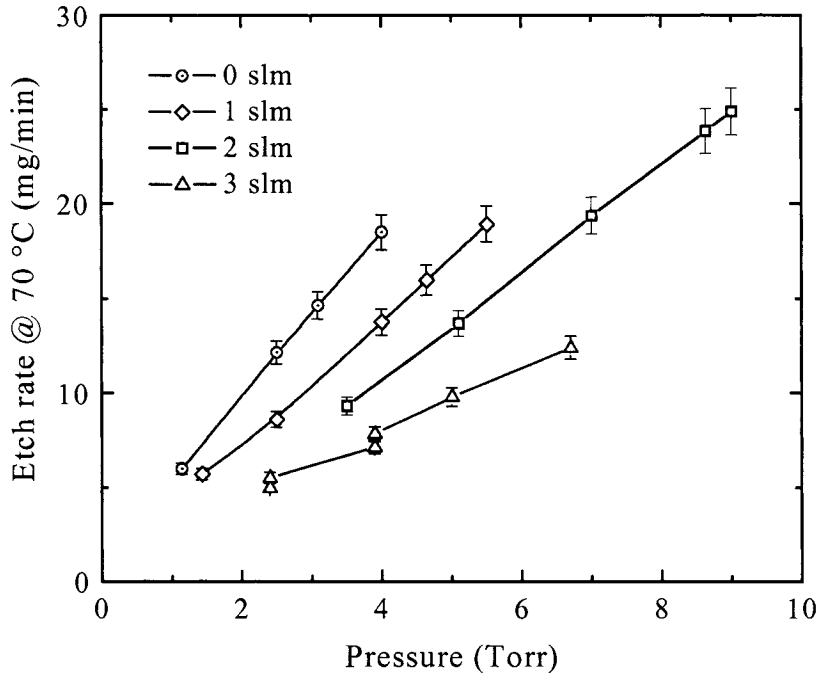

Figure 4.12. Etch rate of SiO_2 as a function of total pressure of $C_3F_8/O_2/Ar$ mixtures for different flows of argon dilution. The flow ratio C_2F_8:O_2 was kept constant at 0.3 slm of C_2F_8 and 0.9 slm of O_2. The Ar flow dilution for the different runs is indicated in the figure. The power set point was 8 kW.

For CF_4 it is interesting to note that, while the addition of argon makes it possible to operate at high flows and higher pressures, the dilution does not decrease the etch rate for a given pressure. The addition of argon allows in this case to access a region of significantly higher etch rates. For C_2F_6, the addition of argon increases the operating range while slightly decreasing the etch rate for a given pressure. In the case of C_3F_8, the addition of argon increases the operating range of the RPS but significantly decreases the etch rate for a given pressure in such a way that the extended operating range does not result in etch rates higher than those obtained with just C_3F_8/O_2 mixtures.

4.4. Conclusions.

In summary, the experimental results show that the SiO_2 etch rates obtained using halocarbons/oxygen mixtures compare well with those achieved using pure NF_3. Within the gases studied, CF_4 and C_3F_8 appear as the most promising candidates. In the case of CF_4, the additions of argon results not only in a wider operating range, but also in higher etch rates.

4.5. References

Callahan R. R. A., Raupp G. B. and Beaudoin S. P. (2001), *J. Vac. Sci. Technol. B* **19**, 725-731.

Flamm D. L. Mogab C. J. and Sklaver E. R. (1979), *J. Appl. Phys.* **50**, 6211-6213.

Flamm D. L. (1989), *Plasma Etching: An Introduction*, D. M. Manos and D. L. Flamm, eds., Academic, New York.

Stueber G. J., Clarke S. A., Bernstein E. R., Raoux S., Porshnev P. and Tanaka T. (2003), *J. Phys. Chem. A* **39**, 7775 – 7782.

Chapter 5 Conclusions and Future Work

In summary, the work presented herein offers answers to important issues related to the understanding, design and operation of transformer-coupled toroidal discharges. The first part of this dissertation analyzes the basic mechanisms of power coupling and power deposition into the plasma, and the processes occurring in the plasma bulk. The simple, yet effective models presented in this part of the study allow for a reasonably accurate description of TCTDs from both electrical and microscopic points of view. In the process of building these models, the relative importance of the different fundamental processes and the range of validity for the different approximations utilized are discussed.

The general circuit analysis in Chapter 2 shows that the plasma bulk in TCTDs could be regarded as the resistive load of a single turn secondary transformer. This is also true for plasmas in electronegative gases, which for the powers and pressures of interest behave as electropositive discharges. Charged particle concentrations are derived from the measurement of the total power absorbed by the plasma (a non-intrusive electrical measurement), using a model that included volume and diffusion losses. The model is contrasted against electron density measurements, giving the right trends and predicting electron densities within 50% of the experimental measurements for a wide range of power and pressure.

Chapter 3 presents a simple model that describes the temporal and spatial characteristics of the voltage and current in conductive toroidal chambers. The model predicts that the potential difference between plasma and chamber wall changes linearly with the position along the torus. As a result, during the peak of RF voltage the electron current from the plasma is concentrated on one side of the dielectric gap, right next to it. The ion current to the wall is uniformly distributed, but the ion energy is the highest at the opposite gap side to where the electron current is concentrated.

The good agreement obtained between the models and the experimental data for argon discharges shows that the simple models capture the essential features of TCTDs. Therefore, the results of the model can be used both as a guide in the design of transformer-coupled chambers, and as a laboratory tool for extracting information about the electron temperature, density, and other quantities of interest on these plasmas.

Further work continuing this research should focus on the integration of simple plasma models, such as the ones described in this Thesis, with sets of equations describing the chemical processes occurring in both the plasma bulk and the inner surface of the chamber. Such an integrated model would allow for the predictions of the concentration of various species as a function of discharge parameters such as power, pressure, flow, etc.

Appendix A

A.1 TCTDs Characteristic Operating Parameters

Table A.1. Typical ranges for the characteristic parameters of high-density TCTD plasmas.

Parameter	Symbol	Units	Range	Ref.
Pressure	p	Torr	0.01 – 10	
Power density	P/V	W/cm^3	0.1 – 10	
Gas temperature	T_g	K	400 – 1,300	Fig. 2.17
Ion temperature	T_i	eV	0.03– 0.1	$T_i = T_g$
Electron temperature	T_e	eV	3 – 1	Fig. 2.33
Gas density	n_g	cm^{-3}	$3\times10^{14} - 9\times10^{16}$	
Peak Plasma density	n_0	cm^{-3}	$10^{11} - 10^{14}$	
Fractional ionization	n_0/n_g		$4\times10^{-4} - 1\times10^{-3}$	
RF frequency	F	Hz	$2\times10^5 - 6\times10^5$	
Electron-atom elastic collisional frequency	ν_m	Hz	$4\times10^7 - 2\times10^9$	(b.17)
Electron-electron collisional frequency	ν_{ee}	Hz	$9\times10^5 - 3\times10^9$	b
Electron energy relaxation frequency	$1/\tau_e$	kHz	$10^3 - 6\times10^4$	(3.7)
Ion-atom collisional frequency	ν_i	Hz	$5\times10^5 - 2\times10^8$	a
Ion plasma frequency	$\omega_{pi}/2\pi$	Hz	$10^7 - 3\times10^8$	b

Electron plasma frequency	$\omega_{pe}/2\pi$	Hz	$3\times10^{9} - 9\times10^{10}$	b
Ambipolar diffusion characteristic frequency	ν_{Da}	Hz	$3\times10^{5} - 2\times10^{3}$	(3.9)
Recombination frequency	ν_{Rec}	Hz	$3\times10^{-5} - 5\times10^{3}$	(2.94)
Ion mean free path	λ_i	cm	$10^{-1} - 3\times10^{-4}$	(3.3)
Electron mean free path	λ_m	cm	$3 - 3\times10^{-2}$	a
Plasma bulk Debye length	λ_{De}	cm	$4\times10^{-3} - 7\times10^{-5}$	a
Plasma density at the sheath edge	n_s	cm^{-3}	$9\times10^{10} - 10^{11}$	(3.19)
Sheath current density	J_{sh}	A/cm^2	$4\times10^{-3} - 2\times10^{-3}$	(2.51)
Debye length at the sheath edge	λ_{De1}	cm	$4\times10^{-3} - 2\times10^{-3}$	(3.2)
Sheath thickness	s	cm	0.02 – 0.03	(3.13)
Ion sheath transit time	τ_r	s	$3\times10^{-8} - 4\times10^{-8}$	(3.11)
Sheath voltage	V_{sh}	V	50	
Electron-atom elastic collision rate	k_m	cm^3/s	$2\times10^{-7} - 3\times10^{-8}$	Fig. b.1
Ion-atom collisional cross section	σ_i	cm^2	4×10^{-14}	a
Ambipolar diffusion coefficient	D_a	cm^2/s	$2\times10^{5} - 10^{2}$	(b.9)

a Lieberman and Lichtenberg (1994)
b Huba (1994)

A.2 References

Huba J. D. (1994), *NRL Plasma Formulary*, Naval Research Laboratory, Washington, DC.

Lieberman M. A. and Lichtenberg A. J. (1994), *Principles of plasma discharges and materials processing*, Wiley, New York.

Appendix B

B.1 Diffusion and Mobility

The momentum conservation equation for a slow time variation, neglecting the inertia $(\vec{u}\cdot\nabla\vec{u})$ and magnetic forces and keeping only the collisional term for one neutral species, can be written as

$$qn\vec{E} - \vec{\nabla}p - mn\nu_m\vec{u} = 0 \qquad \text{(b.1)}$$

where we assumed that the background species are at rest and the momentum transfer frequency ν_m is constant, independent of the drift velocity u. Taking an isothermal plasma, such that $\vec{\nabla}p = kT\vec{\nabla}n$, and solving (b.1) for u, we obtain

$$\vec{u} = \frac{q\vec{E}}{m\nu_m} - \frac{kT}{m\nu_m}\frac{\vec{\nabla}n}{n} \qquad \text{(b.2)}$$

Equation (b.2) can be written

$$\vec{\Gamma} = \pm \mu n \vec{E} - D \vec{\nabla} n \tag{b.3}$$

where $\vec{\Gamma} = n\vec{u}$ is the particle flux, and

$$\mu = \frac{|q|}{m \nu_m} \tag{b.4}$$

and

$$D = \frac{kT}{m \nu_m} \tag{b.5}$$

are the macroscopic mobility and diffusion constant, respectively.

In Section 2.3.1, we use equations (2.26) and (2.27) to define the ambipolar diffusion coefficient as

$$D_a = \left(\frac{\mu_i D_i + \mu_e D_e}{\mu_i + \mu_e} \right) \tag{b.6}$$

The ambipolar diffusion coefficient can usually be simplified by noting that $\mu_e >> \mu_i$ in a weakly ionized discharge. Dropping μ_i in the denominator of (b.6), we get

$$D_a \approx \frac{\mu_i D_i + \mu_e D_e}{\mu_e} \ , \tag{b.7}$$

and using (b.4) and (b.5) we finally obtain

$$D_a \approx D_i \left(1 + \frac{T_e}{T_i} \right) . \tag{b.8}$$

From (b.8) we see that the ambipolar diffusion is tied to the slower species, in this case the ions, but that it is increased by a term proportional to the ratio of the temperatures. In the usual case of weakly ionized plasmas, in which $T_e >> T_i$, we can further simplify (b.8) into

$$D_a = \frac{k T_e}{M \nu_M} . \tag{b.9}$$

B.2 Electron Ionization and Elastic Cross Sections

To obtain ν_{iz}, we must evaluate

$$\nu_{iz} = n_g \langle \sigma_{iz} u \rangle \tag{b.10}$$

where σ_{iz} is the cross section for an ionizing collision. In most cases, σ_{iz} can be approximated as a linear function of the electron energy for energies greater than some threshold value (Cherrignton 1979). Therefore, for a given gas we can choose an ionizing threshold energy and a slope, to describe σ_{iz}. Expanding then the Thomson cross section (Liebermann and Lichtenberg 1994) near $\varepsilon = \varepsilon_{iz}$ we obtain

$$\begin{aligned} \sigma_{iz} &= \sigma_0 \frac{(\varepsilon - \varepsilon_{iz})}{\varepsilon_{iz}} \qquad \varepsilon > \varepsilon_{iz} \\ \sigma_{iz} &= 0 \qquad\qquad\qquad \varepsilon \le \varepsilon_{iz} \end{aligned} \tag{b.11}$$

where ε_{iz} is the ionization energy, $\varepsilon = \frac{1}{2}\, m\, u^2/e$, $\sigma_0 = (e/4\,\pi\,\varepsilon_0\,\varepsilon_{iz})^2$, and

$$\nu_{iz} = n_g \frac{\sigma_0}{\varepsilon_{iz}} \langle (\varepsilon - \varepsilon_{iz}) u \rangle \qquad \varepsilon > \varepsilon_{iz}\,. \tag{b.12}$$

For a Maxwellian distribution

$$f(\varepsilon) = \frac{2\sqrt{\varepsilon}}{\sqrt{\pi}\,(k T_e)^{3/2}} \exp\left(-\frac{\varepsilon}{k T_e}\right), \tag{b.13}$$

the ionization frequency is

$$\nu_{iz} = \int_{\varepsilon_{iz}}^{\infty} n_g \frac{\sigma_0}{\varepsilon_{iz}} (\varepsilon - \varepsilon_{iz}) \sqrt{\frac{2\varepsilon}{m}} \frac{2\sqrt{\varepsilon}}{\sqrt{\pi}\,(k T_e)^{3/2}} \exp\left(-\frac{\varepsilon}{k T_e}\right) d\varepsilon \tag{b.14}$$

Integrating we obtain

$$\nu_{iz} = k_{iz}(T_e) n_g \tag{b.15}$$

with

$$k_{iz}(T_e) = \sigma_0 \bar{v}_e \left(1 + \frac{\varepsilon_{iz}}{2T_e}\right) \exp\left(-\frac{\varepsilon_{iz}}{T_e}\right) \tag{b.16}$$

where $\bar{v}_e = (8eT_e/\pi m)^{1/2}$ is the mean electron speed.

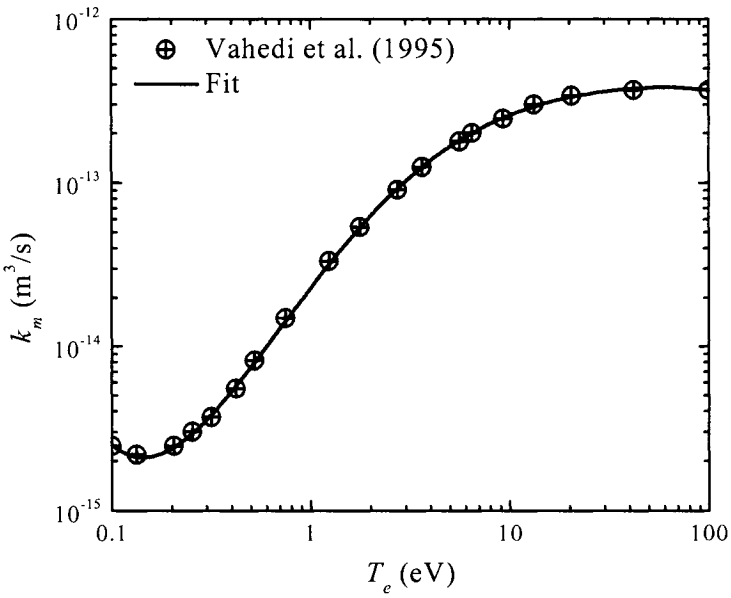

Figure b.1. Electron elastic collision rate constant k_m versus T_e in argon (Vahedi et al. 1995).

As a crude analytical approximation to the atom elastic collision rate constant (k_m) over a limited range of T_e, we fitted a fifth order polynomial to the datb. Using this fit, we can calculate the momentum transfer frequency as

$$\nu_m(T_e) = n_g k_m(T_e) \tag{b.17}$$

Figure b.1 shows the electron-atom elastic collisional rate constant as a function of the electron temperature. This rate constant was obtained by integrating the experimentally measured cross section (Vahedi et al. 1995) over a Maxwellian electron energy distribution.

B.3 Energy Loss per Electron Ion Pair Created

One of the most vital quantities for finding the electron density using a global model is the electron collision energy loss per electron ion pair created by ionization, $\varepsilon_c(T_e)$ (Liebermann and Lichtenberg 1994). This quantity strongly depends on the rate of excitations, and is given by

$$\varepsilon_c = \varepsilon_{iz} + \sum_i \varepsilon_{ex,i} \frac{k_{ex,i}}{k_{iz}} + \frac{k_{el}}{k_{iz}} \frac{3M}{m} T_e \tag{b.18}$$

where ε_{iz} is the ionization energy, $\varepsilon_{ex,i}$ is the energy for the i-th excitation process, k_{iz} is the ionization rate constant (b.16), $k_{ex,i}$ is the rate constant for the i-th excited state and k_{el} is the elastic scattering rate const. The terms on the RHS of (b.18) account for the loss of electron energy due to ionization, excitation and elastic (polarization) scattering against neutral atoms. These are usually the dominant energy loss mechanisms in weakly ionized electropositive discharges. The quantity $(3\ m/M)T_e$ is the mean energy lost per electron for a polarization scattering. The resulting values for argon as a function of temperature are shown in figure b.2.

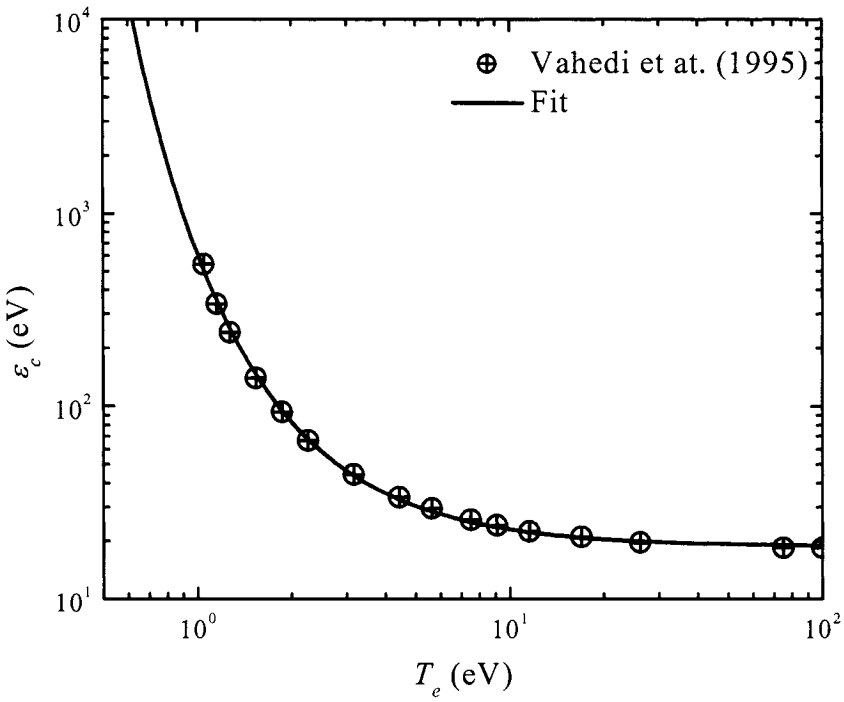

Figure b.2 Collisional energy lost per electron-ion pair created ε_c, versus *Te* in argon (Vahedi et al. 1995).

The quantity ε_e is the mean kinetic energy lost per electron lost (Vahedi et al. 1995), which for Maxwellian electrons is

$$\varepsilon_e = 2T_e . \tag{b.19}$$

The ion-bombarding energy ε_i is the sum of the ion energy entering the sheath and the energy gained by the ion as it traverses the sheath. The ion velocity when it enters the sheath is u_B, corresponding to a directed energy of $T_e/2$. The sheath voltage V_{sh} for an insulating wall is (see Chapter 3 for a complete description)

$$V_{sh} = \frac{T_e}{2} \ln\left(\frac{M}{2\pi m}\right) \tag{b.20}$$

The ion kinetic energy lost at the surface is then

$$\varepsilon_i = V_{sh} + \frac{T_e}{2} . \tag{b.21}$$

Summing the three contributions yields the total energy loss per electron ion pair lost from the system (Vahedi et al. 1995):

$$\varepsilon_T = \varepsilon_c + \varepsilon_e + \varepsilon_i . \tag{b.22}$$

B.4 Effective Electron Collisional Frequency

Plasma conductivity is a fundamental parameter defining electrical characteristics of a plasma device and is a basic parameter in models of gas discharge plasmas. The electrical conductivity of cold a plasma (σ_{bk}) expresses the relation between the local current density J and the local electric field E through Ohm's law (see Eq. 2.1)

$$\sigma_{bk} = \frac{E}{J} = \frac{n_e e^2}{m_e (\nu_e + j\omega)}, \tag{b.23}$$

where e and m_e are the electron charge and mass, respectively, n_e is the plasma density, ν_e is the electron transport collision frequency in the radio frequency field and ω is the RF field frequency. Equation (b.23) is applicable for a cold, collision-dominated plasma where the RF field electron heating is solely due to electron-atom and electron-ion collisions.

The electron transport collision frequency in an argon discharge was calculated by Godyak et al. (1999) from the plasma conductivity measured with a magnetic probe in a stove top ICP at 6.78 MHz. Figure b.3 shows the experimental values obtained by Godyak et al. (1999) and the function used to fit the experimental data.

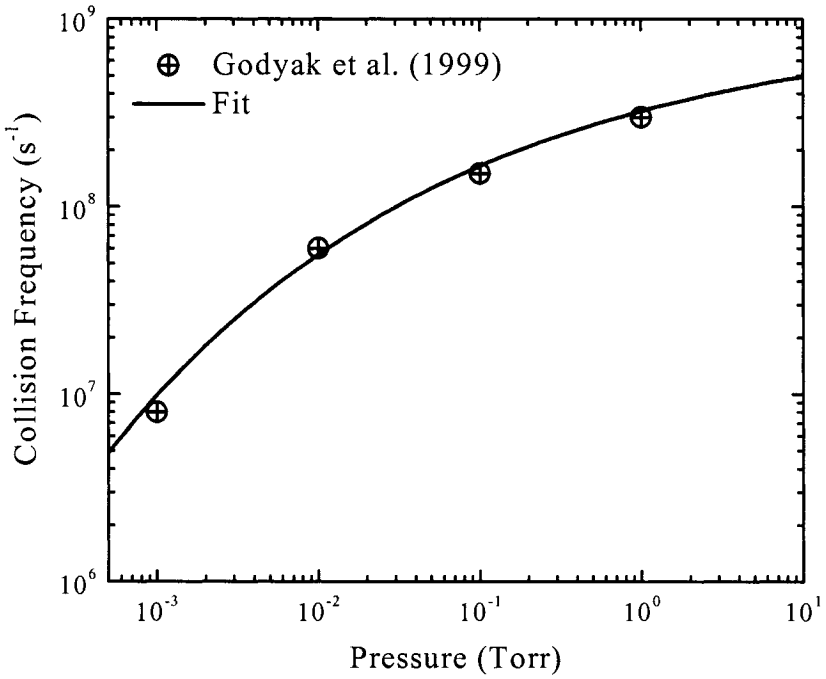

Figure b.3. Electron transport effective collision frequency (ν_e) as a function of pressure (Godyak et al. 1999).

B.5 Recombination Losses

The recombination process, being of a collisional microscopic nature, is considerably more complicated in its details than diffusion. The probability for a recombination event to occur will depend upon the relative kinetic energies of the electron and the ion and on how the energy and momentum can be conserved in the recombination process. In the next Sections, we will describe some of the particular recombination processes that may take place in rare gas TCTD plasmas.

Radiative Recombination

In this process an electron and ion recombine, and the extra energy is given off in the form of radiation (photons)

$$X^+ + e \rightarrow X + h\nu . \tag{b.24}$$

This process has a relative low probability because of the difficulty of conserving energy and momentum, and so is usually important only at low densities, where the probability for other recombination mechanisms is very low. Bates and Dalgarno (1962), and Raizer (1991) quote the total radiative recombination coefficient to be approximately $k_{rad} = 10^{-12}$ cm^3/s.

Three-Body Recombination

The probability of an electron-ion recombination occurring is substantially increased if a third body is present to take away the excess energy. Of course, the density of the third body needs to be reasonably high for such a recombination event to occur. The third body can be a neutral, a positive ion or an electron. In general, there are roughly as many electrons available as positive ions, and since electrons are much more effective in removing excess energy, we will ignore positive ions.

The recombination rate when the third body is an electron follows the scheme

$$X^+ + e + e \rightarrow X + e ; \tag{b.25}$$

This is usually the dominant process in high density, low temperature equilibrium plasmas where $T_g \approx T_e \sim 1$ V, and the concentration of molecular ions is too low for dissociative recombination to be significant. The rate coefficient for this process is given by (Zel'dovich and Raizer 1966)

$$k_{3B} = 8.75 \times 10^{-27}\ \mathrm{cm^6/s}\ \ T_e(eV)^{-\frac{9}{2}} n_e \quad . \tag{b.26}$$

For the range of electron temperatures and densities of our interest this constant is rather small ($k_{3B} \approx 10^{-14}$ cm^3/s), and therefore can be neglected.

Neutral atoms or molecules are, of course, far less efficient in removing excess energy than electrons with a recombination coefficient $\beta_{3B} \approx 10^{-34}$ cm^6/s (Raizer 1991). This process is not typical for discharges conditions and can manifest itself only at very weak ionization and very high pressures.

Dissociative Recombination

In this case, a molecular ion plus an electron make a radiation-less transition to an unstable molecule, which causes the atoms forming the molecule to move apart and gain kinetic energy due to their mutual repulsion.

$$XY^+ + e \leftrightarrow (XY)^* \rightarrow X + Y^* \tag{b.27}$$

The importance of this process is due to its high efficiency and large recombination coefficient. For the neutral densities of our interest, it is quite possible to have sizeable densities of molecular ions present. This is clearly shown in Fitzwilson and Chanin (1973), who reported measurements of the ratio of molecular to atomic ion densities in Ar, Kr, and Xe discharges. This process can be important even in plasmas where atomic ions predominate, since atomic ions can be converted into molecular ions by collisional processes. For instance, in argon we have

$$Ar^+ + 2Ar \rightarrow Ar_2^+ + Ar \qquad \text{(b.28)}$$

with reported values for the conversion rate k_{conv}, consistently in the range between 1.9×10^{-31} and 4.7×10^{-31} cm^6/s (Bhattacharya 1970; Fitzwilson and Chanin 1973; Bogaerts and Gijbels 1999).

The rate of recombination under plasmas conditions such as are encountered in the discharges discussed here is controlled by the equilibrium rate of formation of the Ar_2^+ molecular ion. These ions may be formed by atomic ion to molecular conversion (b.28) or by Hornbeck-Molnar process (Gaur and Chanin 1969). The Hornbeck-Molnar process

$$Ar^* + Ar \rightarrow Ar_2^+ + e \qquad \text{(b.29)}$$

probably contributes little to the Ar_2^+ population since E/P for these high density discharges is of the order of 0.1 V/(cm Torr) (Loeb 1955). This would result in a population of the excited states that engage in the Hornbeck-Molnar process of such a low value that the rate of Ar_2^+ formation by collision of excited and ground state atoms would be several orders of magnitude less than the rate from atomic ion to molecular conversion.

The loss of Ar_2^+ is assumed to occur by diffusion to the walls or by dissociative recombination,

$$Ar_2^+ + e \rightarrow Ar + Ar\,, \tag{b.30}$$

which are known to be much more efficient than other (e.g. three-body) recombination process (Biberman et al. 1987). The value obtained by Fitzwilson and Chanin (1973) for the dissociative recombination coefficient was $k_{diss} = 4.5\times10^{-9}$ cm^3/s for an electron temperature of 14,000 K.

To obtain the electron rate of loss by dissociative recombination, we need to calculate the Ar_2^+ molecular ion density, which is obtained from the balance equation for the ion and the plasma neutrality condition,

$$\begin{aligned} &\vec{\nabla}\cdot D_{a2}\vec{\nabla}n_{2+}(r) + k_{conv}\, n_+(r) n_g{}^2 - k_{diss}\, n_{2+}(r) n_e(r) = 0 \\ &n_e(r) = n_{2+}(r) + n_+(r) \end{aligned} \tag{b.31}$$

where $n_{2+}(r)$ is the Ar_2^+ density and D_{a2} is the Ar_2^+ ambipolar diffusion coefficient. Following the same procedure than in (2.45) and (2.46), we obtain the particle conservation equation for the volume averaged particle densities.

$$-\frac{D_{a2}}{d_{eff}R_p^{\ 2}}n_{2+} + A_{eff}\,k_{conv}\,n_+\,n_g^{\ 2} - B_{eff}\,k_{diss}\,n_{2+}\,n_e = 0$$

$$n_e = n_{2+} + n_+ \tag{b.32}$$

where now n_{2+}, n_+ and n_e are the particle peak densities and A_{eff}, B_{eff} and d_{eff} are defined by (2.50) and (2.52) respectively. Here it is assumed that the ions and electrons have the same density spatial profile.

Solving for Ar_2^+ peak density we obtain

$$n_{2+} = \frac{A_{eff}\,k_{conv}\,n_g^{\ 2}\,n_e}{\frac{D_{a2}}{d_{eff}\,R_p^{\ 2}} + A_{eff}\,k_{conv}\,n_g^{\ 2} + B_{eff}\,k_{diss}\,n_e}, \tag{b.33}$$

and the spatially averaged electron loss frequency for dissociative recombination is

$$\langle \nu_{diss} \rangle = B_{eff}\,k_{diss}\,n_{2+}\,. \tag{b.34}$$

Utilizing equation (b.33), we can calculate the Ar^{+}_{2} molecular concentration as a function pressure. Figure b.4 shows this dependency for a 160W discharge, these results are in agreement with the experimental results obtained by Fitzwilson and Chanin (1973) in the positive columns of small diameter noble gas discharges.

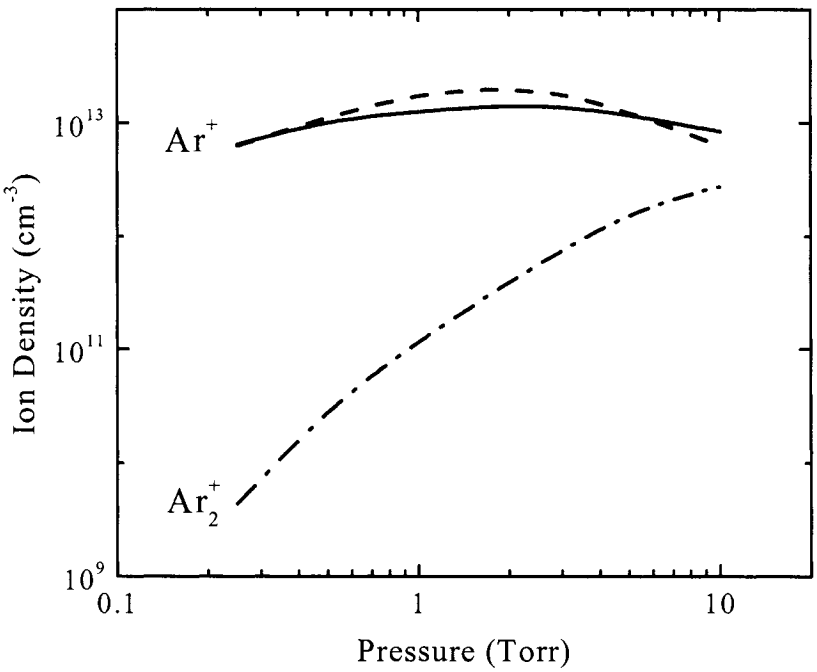

Figure b.4. Atomic and molecular ion densities versus pressure for a 160 W argon plasma. The blue dashed line corresponds to the Ar^{+} atomic ion density predicted by the model, the solid red line corresponds to the experimental measurements and the green dash-dot line corresponds to the Ar_2^{+} molecular ion density predicted by the model (Eq. b.33).

B.6 References

Bates D. R. and Dalgarno A. (1962), *Electronic Recombination in Atomic and Molecular Processes*, 1-57, Academic Press.

Bhattacharya A. K. (1970), *J. Appl. Phys* **41**, 1707-1710.

Biberman L. M., Vorob'ev V. S. and Iakubov I. T. (1987), *Kinetics of Non-equilibrium Low-temperature Plasmas*, Plenum, New York.

Bogaerts A. and Gijbels R. (1999), *J. Appl. Phys* **86**, 4124-4133.

Cherrignton B. E. (1979), *Gaseous electronics and Gas Lasers*, Pergamon Press, Headington Hill, Oxford.

Fitzwilson R. L., and Chanin L. M. (1973), *J. Appl. Phys* **44**, 5337-5346.

Gaur J. P. and Chanin L. M. (1969), *Phys. Rev.* **182**, 167–175.

Godyak V. A., Piejak R. B. and Alexandrovich B. M. (1999), *J Appl.* Phys. **85**, 3081-3083.

Lieberman M. A. and Lichtenberg A. J. (1994), *Principles of plasma discharges and materials processing*, Wiley, New York.

Loeb L. B. (1955), *Basic Processes in Gaseous Electronics*, University of California Press, Berkeley.

Raizer Y. P. (1991), *Gas Discharge Physics*, Springer Verlag, Berlin Heidelberg.

Vahedi V., Lieberman M. A., DiPeso G., Rognlien T. D. and Hewett D. (1995), *J. Appl. Phys.* **78**, 1446-1458.

Zel'dovich Y. A. and Raizer Y. P. (1966), *Physics of Shocks Waves and High-Temperature Hydrodynamic Phenomena*, Academic Press, New York.

Appendix C

For clarity and organizational purposes, this Appendix contains results and data complementary to those discussed in Chapter 2.

C.1 Supplementary data to Section 2.5.2

Figures c.1 and c.2 complements the electrical data presented in Section 2.5.2 for argon (figure c.1) and oxygen (figures c.2) discharges.

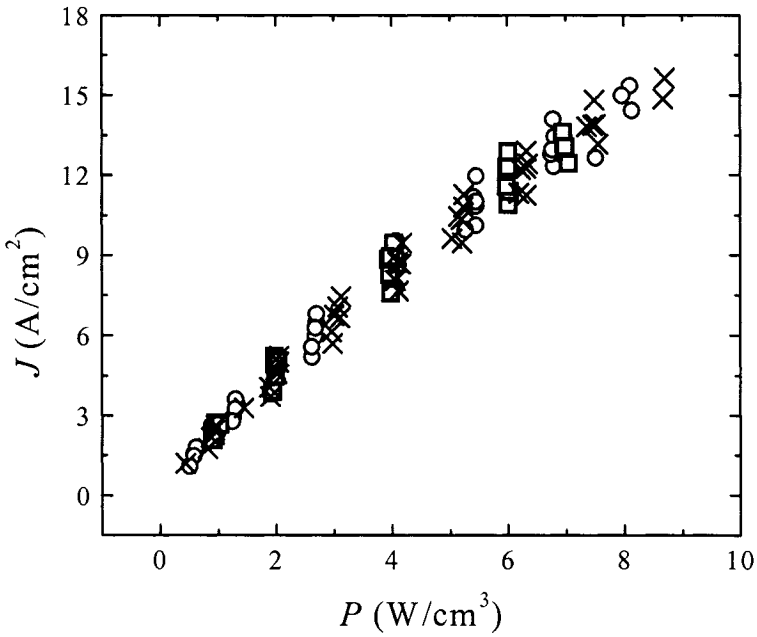

Figure c.1. Linear dependence between the current density and the power density for discharge pressures between 250 mTorr and 10 Torr of argon. The red crosses (×), green circles (○) and the blue squares (□) correspond to data from discharge tubes *"C"* (41.4 cm), *"B"* (32.4 cm) and *"A"* (22.4 cm), respectively.

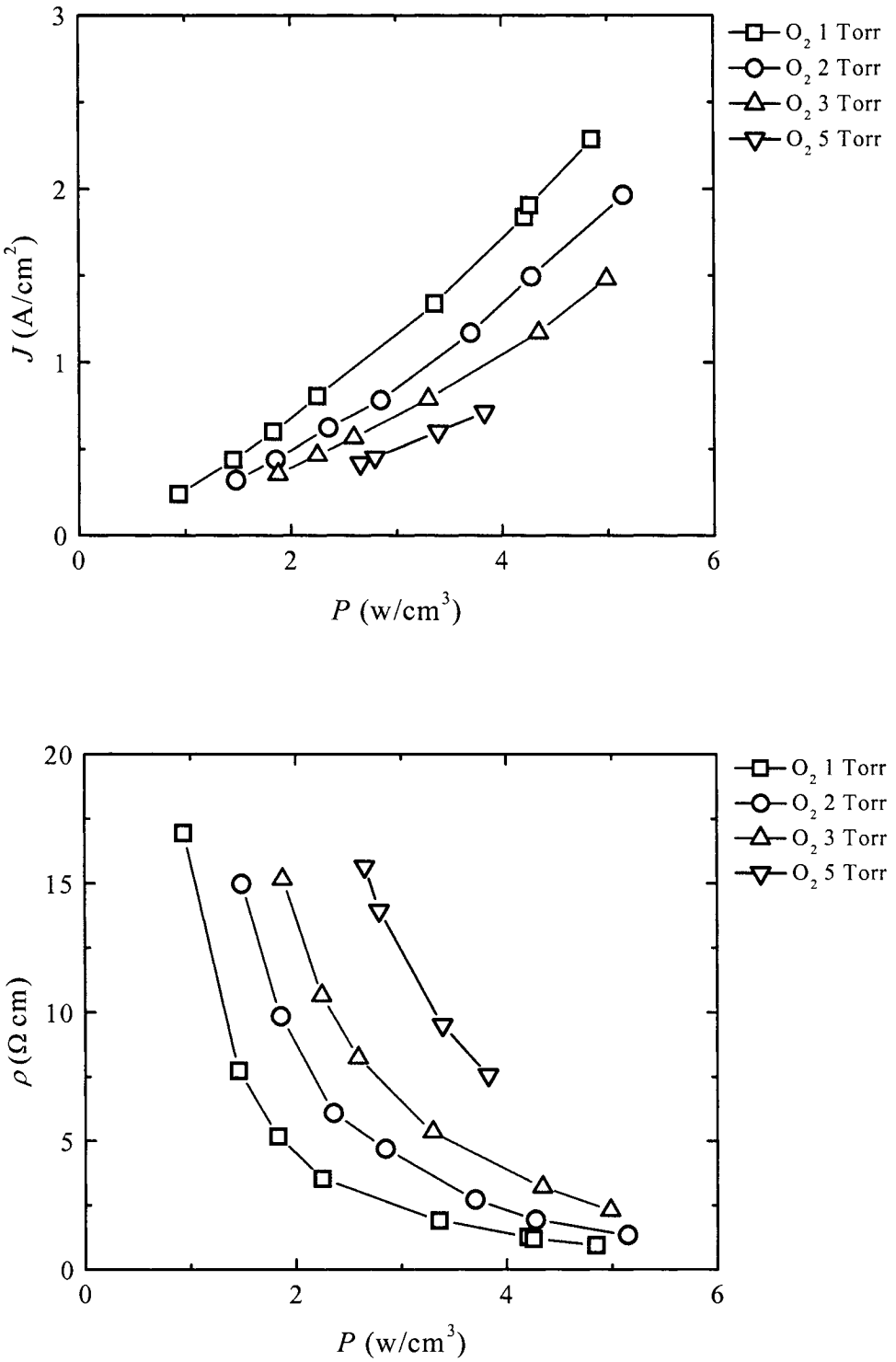

Figure c.2. Plasma current density and resistivity versus power density for 4 slm of oxygen flow at different pressures

C.2 Supplementary data to Section 2.5.3

Using the experimental electrical data as the input parameters as was described in Section 2.5.2, the plasma density in an argon discharge was calculated for a range of plasma powers and pressures. The calculated results for the electron density from the ambipolar diffusion model and a model that includes volume recombination are compared to the electron density values obtained from the ion saturation current measurements

Figures b3 to b12 show a comparison between the experimental data and the predictions from a purely diffusive and diffusion + recombination models as a function of pressure for different power levels. Figures b13 to b18 compare the electron density measurements with the model as a function of power for pressures between 250 mTorr and 10 Torr. In this graphs the red squares represent the experimental points, the blue circles with a solid line correspond to the diffusion model and the green pluses with the dashed line corresponds to the full (diffusion + recombination) model.

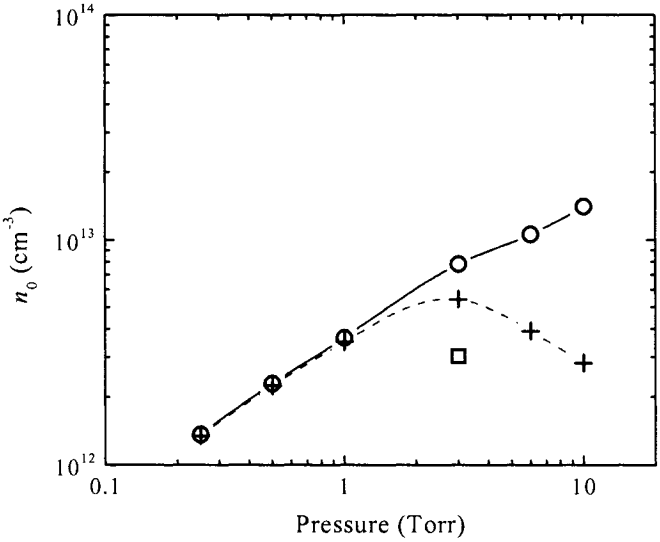

Figure c.3. Comparison between experimental data and the predictions from a purely diffusive and diffusion + recombination models (Argon, 36 W, tube *"C"*).

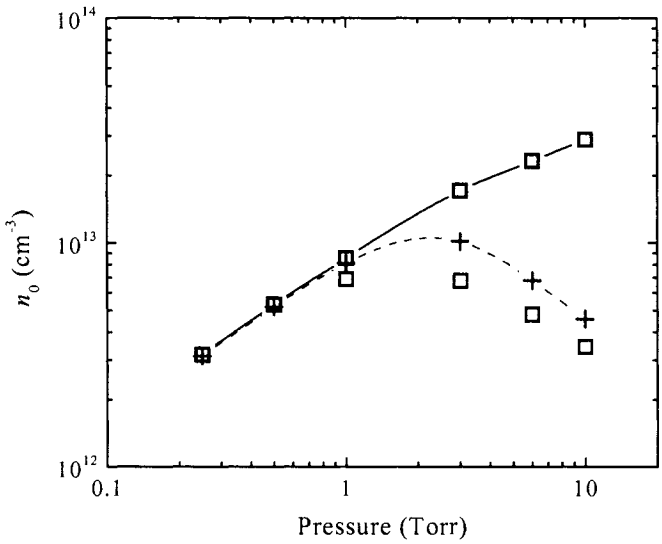

Figure c.4. Comparison between experimental data and the predictions from a purely diffusive and diffusion + recombination models (Argon, 75 W, tube *"C"*).

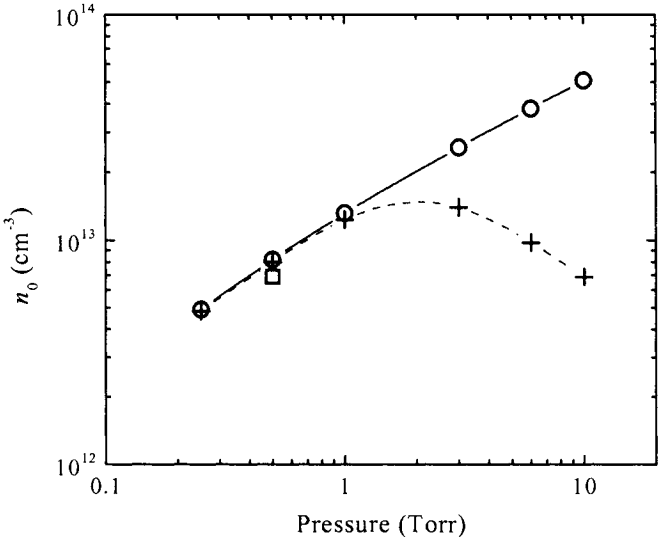

Figure c.5. Comparison between experimental data and the predictions from a purely diffusive and diffusion + recombination models (Argon, 120 W, tube *"C"*).

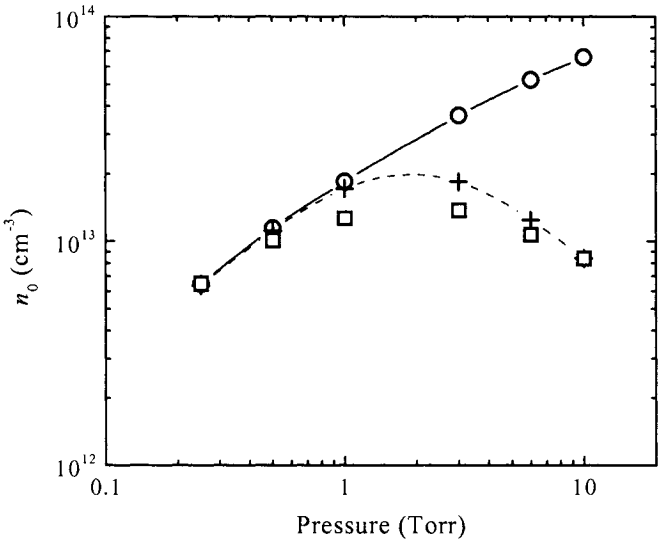

Figure c.6. Comparison between experimental data and the predictions from a purely diffusive and diffusion + recombination models (Argon, 165 W, tube *"C"*).

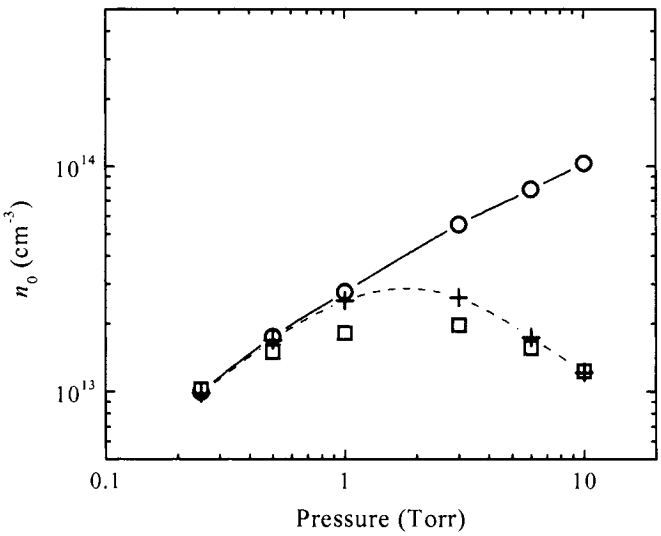

Figure c.7. Comparison between experimental data and the predictions from a purely diffusive and diffusion + recombination models (Argon, 250 W, tube *"C"*).

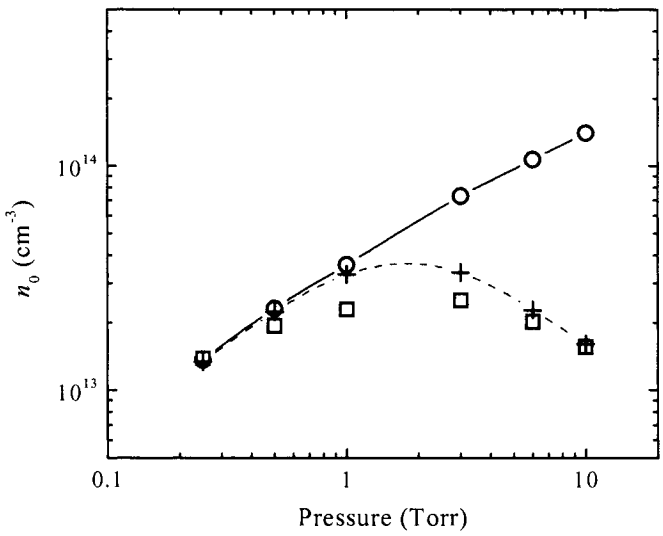

Figure c.8. Comparison between experimental data and the predictions from a purely diffusive and diffusion + recombination models (Argon, 340 W, tube *"C"*).

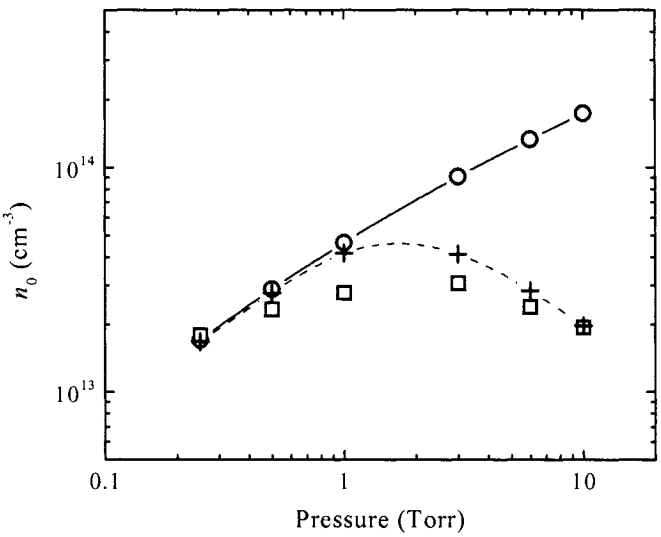

Figure c.9. Comparison between experimental data and the predictions from a purely diffusive and diffusion + recombination models (Argon, 430 W, tube *"C"*).

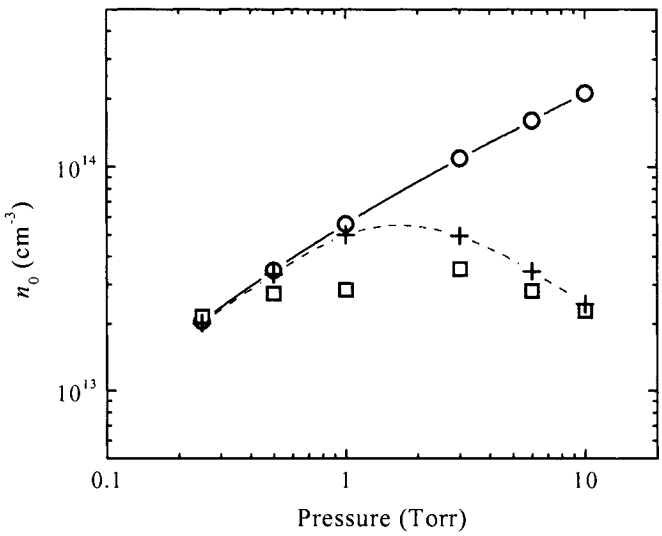

Figure c.10. Comparison between experimental data and the predictions from a purely diffusive and diffusion + recombination models (Argon, 525 W, tube *"C"*).

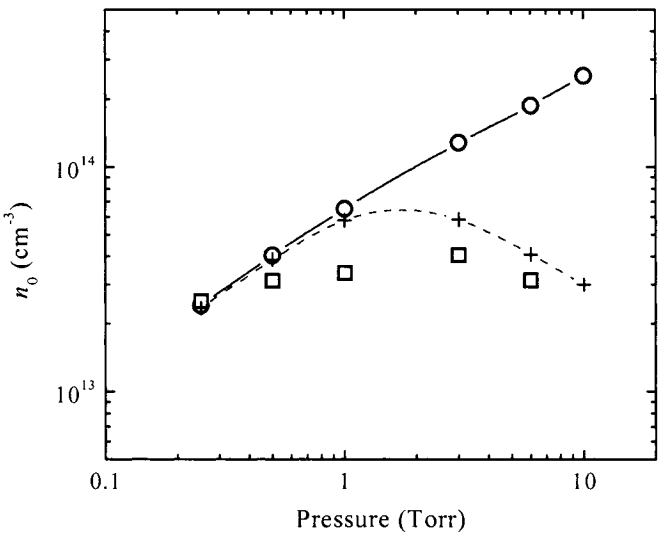

Figure c.11. Comparison between experimental data and the predictions from a purely diffusive and diffusion + recombination models (Argon, 625 W, tube *"C"*).

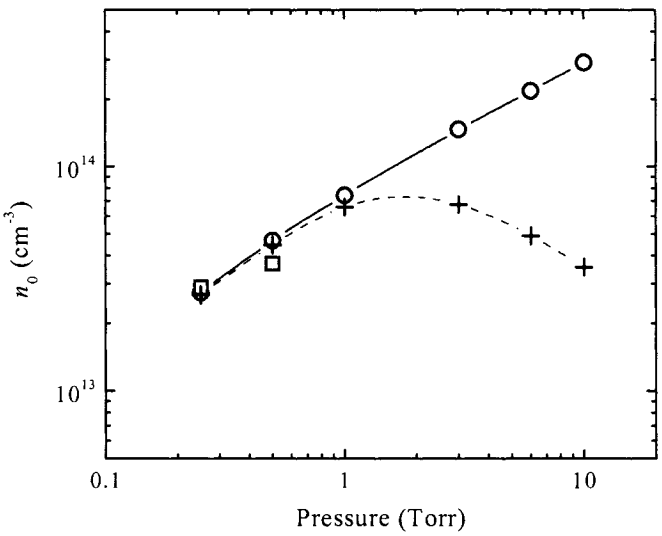

Figure c.12. Comparison between experimental data and the predictions from a purely diffusive and diffusion + recombination models (Argon, 720 W, tube *"C"*).

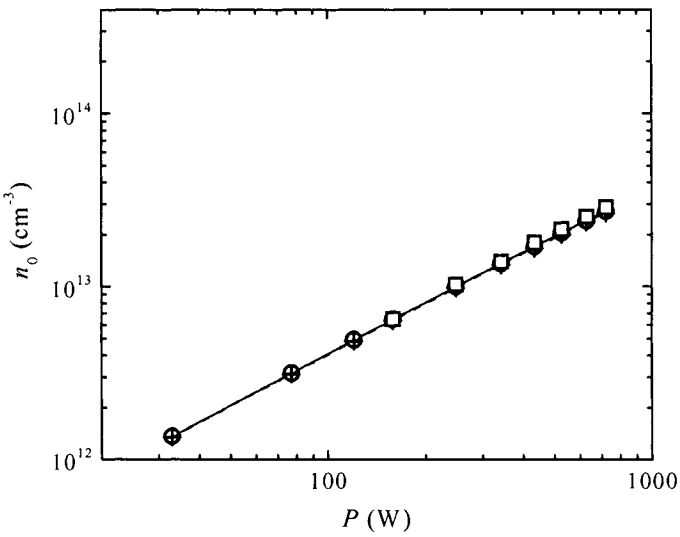

Figure c.13. Electron density versus power for a 250 mTorr argon discharge (tube *"C"*).

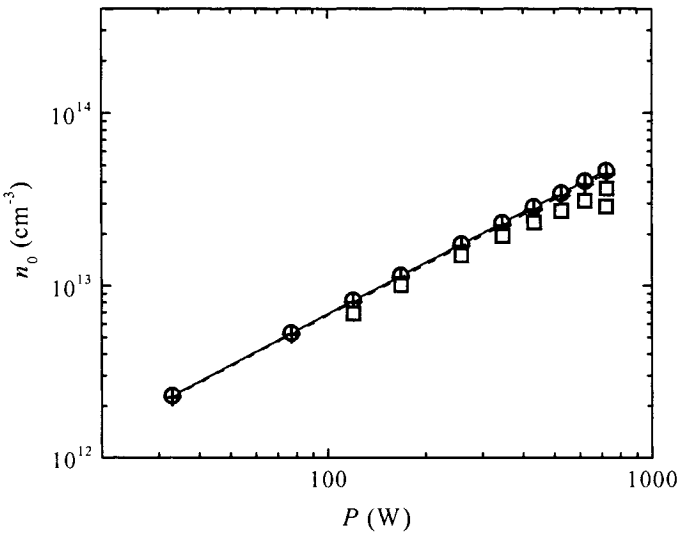

Figure c.14. Electron density versus power for a 500 mTorr argon discharge (tube *"C"*).

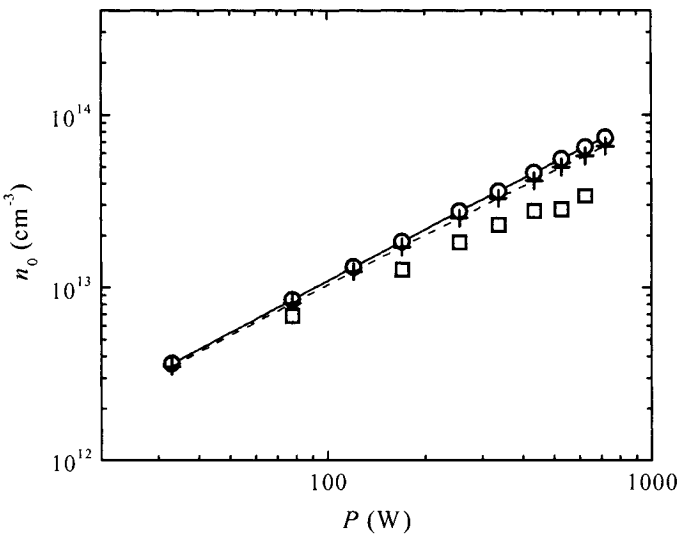

Figure c.15. Electron density versus power for a 1 Torr argon discharge (tube *"C"*).

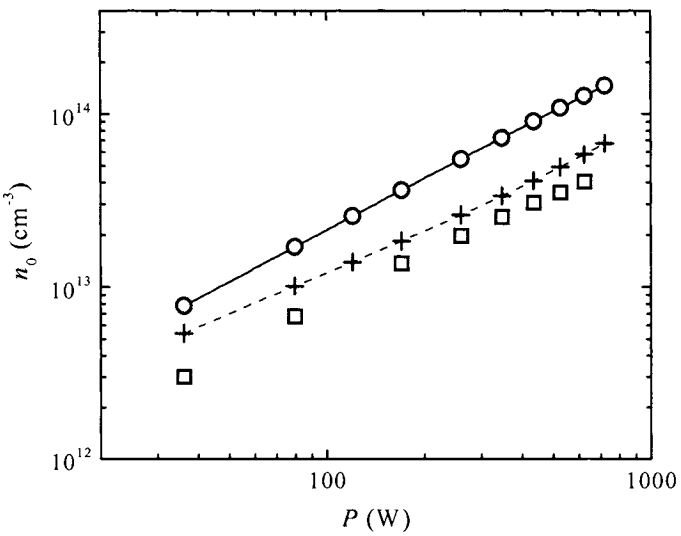

Figure c.16. Electron density versus power for a 3 Torr argon discharge (tube *"C"*).

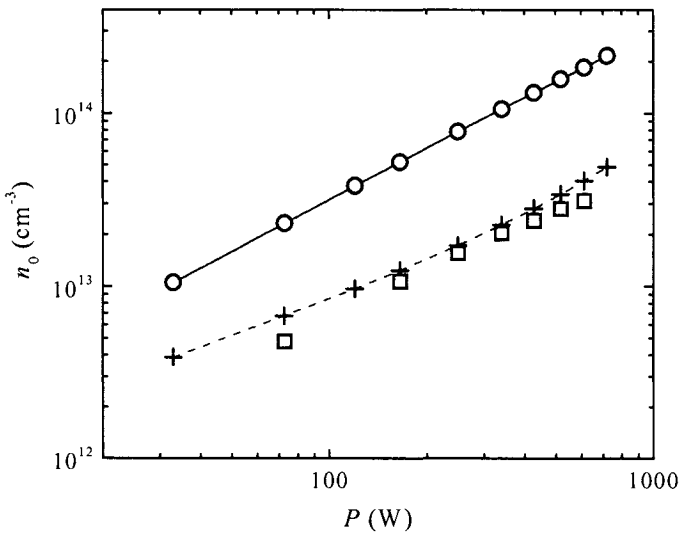

Figure c.17. Electron density versus power for a 6 Torr argon discharge (tube *"C"*).

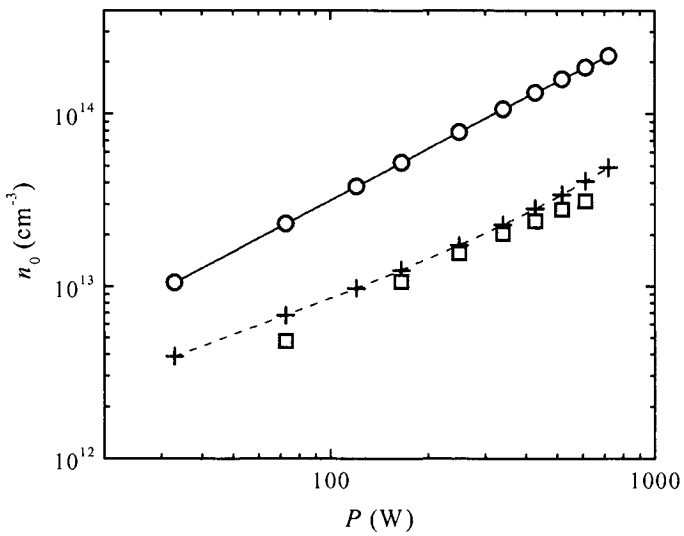

Figure c.18. Electron density versus power for a 10 Torr argon discharge (tube *"C"*).

C.3 Supplementary data to Section 2.5.5

Figures c.19 to c.28 show how the experimental and predicted values for the plasma resistance, current and voltage as a function of pressure compare for a given power. Figures c.29 and c.30 show the experimental and predicted values for the plasma current and resistance as a function of power for a pressure of 6 Torr. The red squares represent the experimental points; the blue circles with a solid line correspond to the model predicted values.

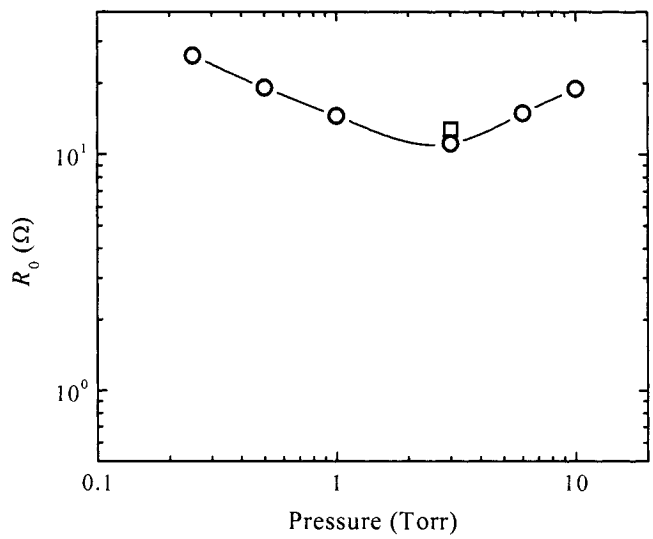

Figure c.19. Experimental and calculated plasma resistance as a function of pressure for an argon plasma on discharge tube *"C"* (power: 36 W).

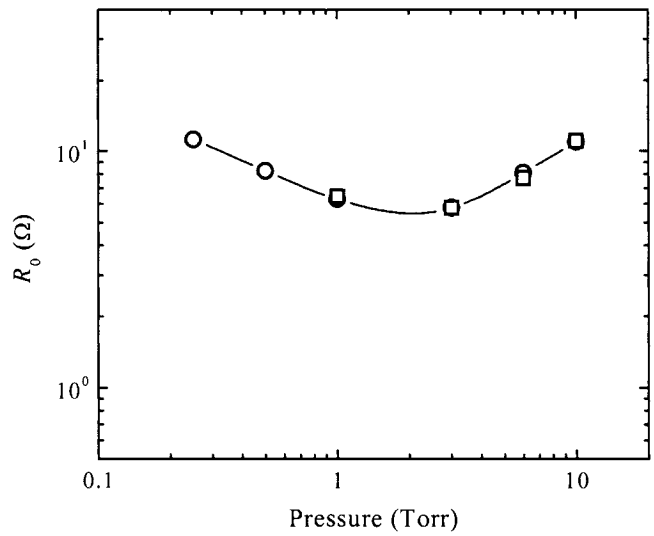

Figure c.20. Experimental and calculated plasma resistance as a function of pressure for an argon plasma on discharge tube *"C"* (power: 75 W).

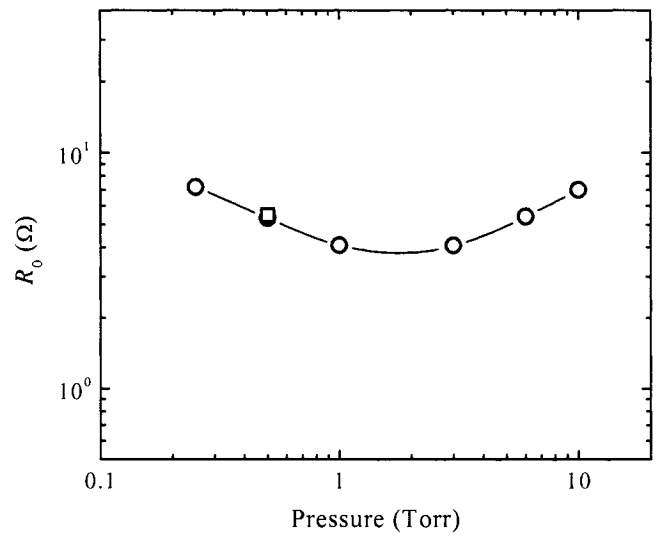

Figure c.21. Experimental and calculated plasma resistance as a function of pressure for an argon plasma on discharge tube *"C"* (power: 120 W).

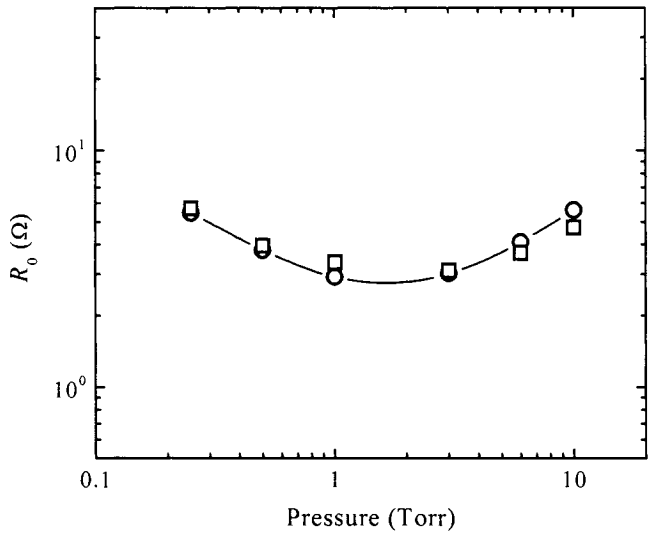

Figure c.22. Experimental and calculated plasma resistance as a function of pressure for an argon plasma on discharge tube *"C"* (power: 165 W).

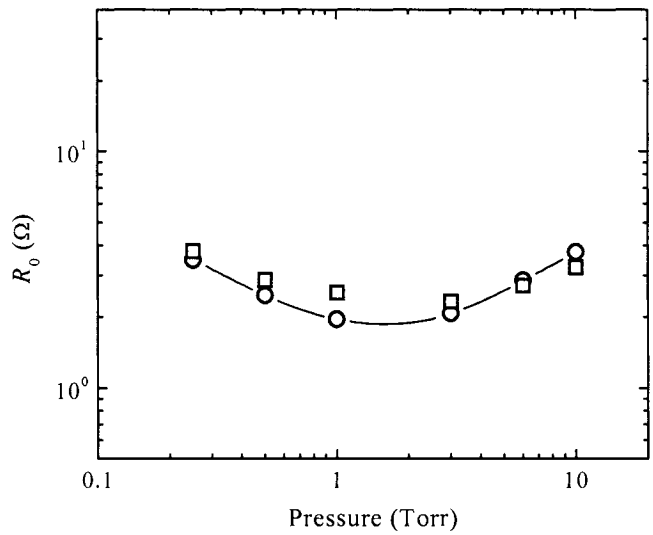

Figure c.23. Experimental and calculated plasma resistance as a function of pressure for an argon plasma on discharge tube *"C"* (power: 250 W).

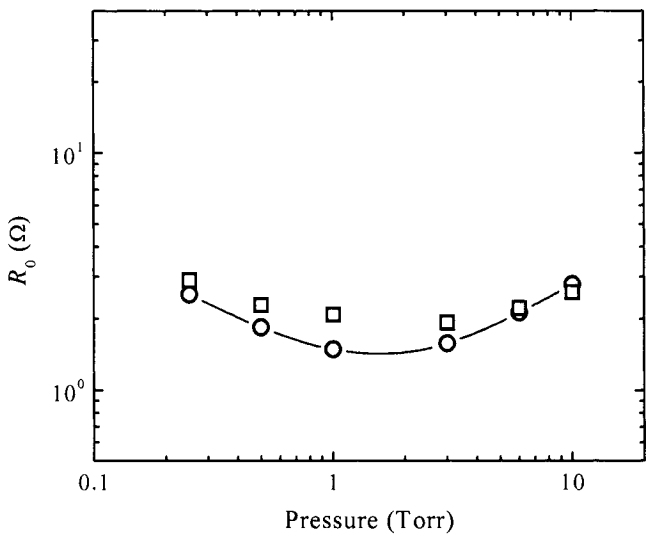

Figure c.24. Experimental and calculated plasma resistance as a function of pressure for an argon plasma on discharge tube *"C"* (power: 340 W).

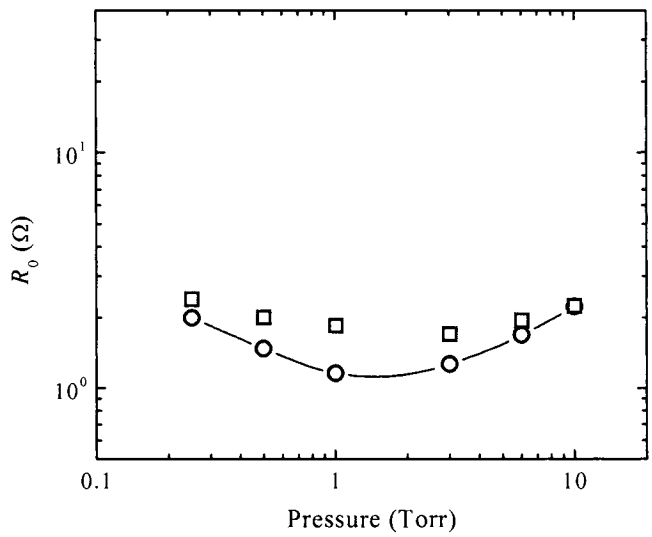

Figure c.25. Experimental and calculated plasma resistance as a function of pressure for an argon plasma on discharge tube *"C"* (power: 430 W).

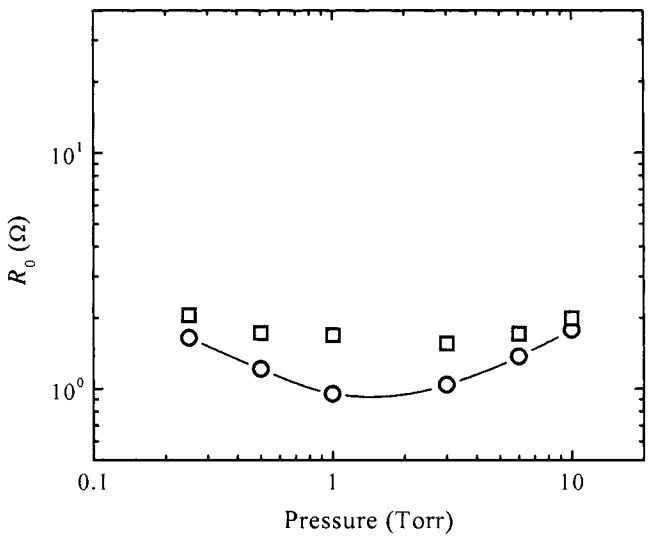

Figure c.26. Experimental and calculated plasma resistance as a function of pressure for an argon plasma on discharge tube *"C"* (power: 525 W).

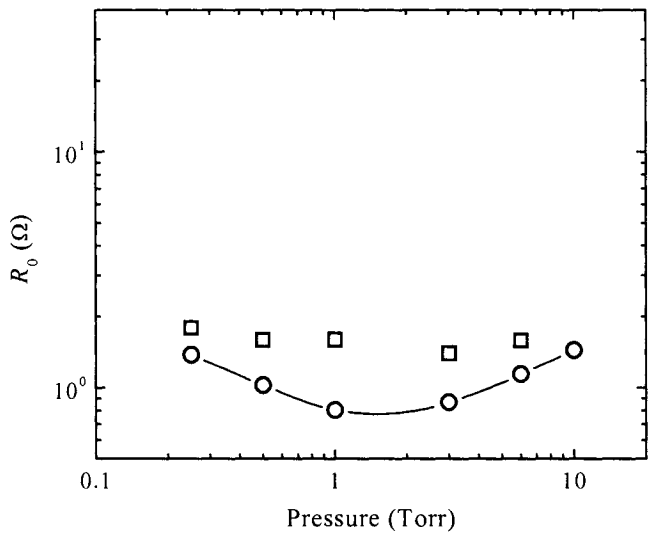

Figure c.27. Experimental and calculated plasma resistance as a function of pressure for an argon plasma on discharge tube *"C"* (power: 625 W).

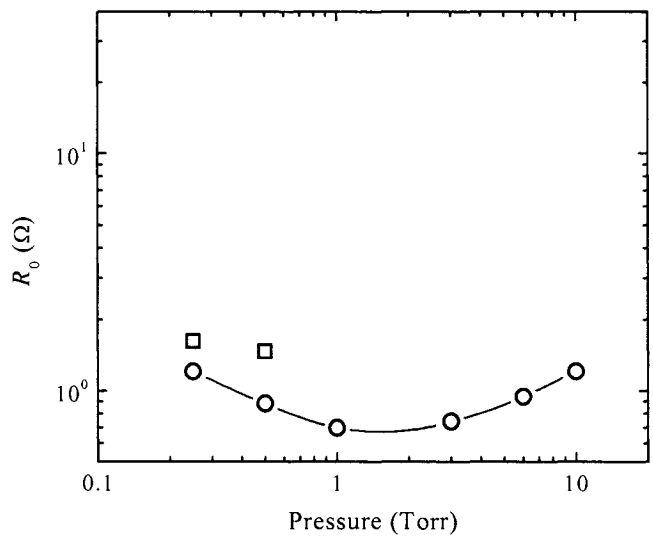

Figure c.28. Experimental and calculated plasma resistance as a function of pressure for an argon plasma on discharge tube *"C"* (power: 720 W).

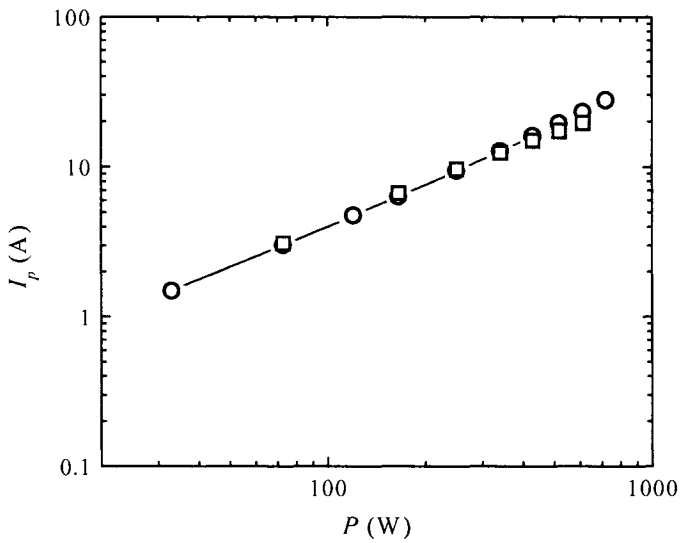

Figure c.29. Experimental and calculated plasma current versus power for a 6 Torr argon discharge. The red squares represent the experimental points; the blue circles with a solid line correspond to model the predicted values

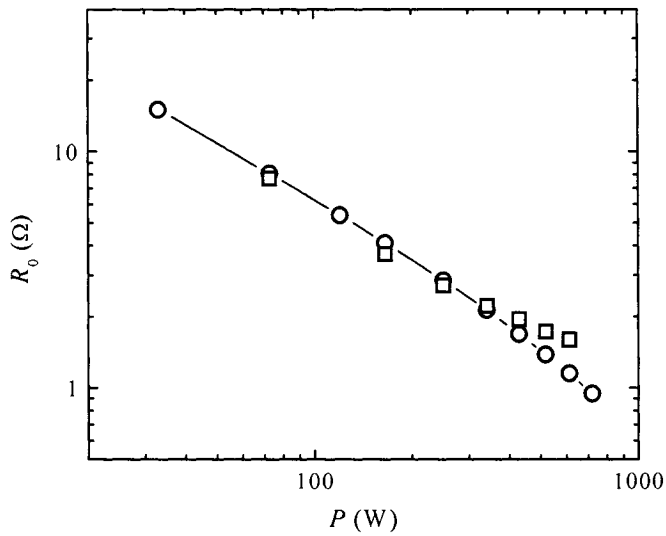

Figure c.30. Experimental and calculated plasma resistance versus power for a 6 Torr argon discharge. The red squares represent the experimental points; the blue circles with a solid line correspond to model the predicted values.